Design, Modelling, Fabrication, and Testing of a Hall Effect Based Pressure Sensor

THESIS

Submitted in the partial fulfilment of the requirements for the degree of

DOCTOR OF PHILOSOPHY

by

Sankalp Paliwal
2018PHXF0434P

Under the supervision of

Dr. Sujan Yenuganti

BIRLA INSTITUTE OF TECHNOLOGY & SCIENCE

PILANI – 333031 (RAJASTHAN) INDIA

2023

BIRLA INSTITUTE OF TECHNOLOGY & SCIENCE

PILANI- 333031 (RAJASTHAN) INDIA

CERTIFICATE

This is to certify that the thesis entitled **"Design, Modelling, Fabrication, and Testing of a Hall Effect Based Pressure Sensor"** submitted by **Sankalp Paliwal,** ID. No**. 2018PHXF0434P** for award of Ph.D. of the Institute embodies original work done by him under my supervision.

Signature in full of the Supervisor ______________________

Name : **Dr. Sujan Yenuganti**

Designation : **Assistant Professor**

Department of Electrical and Electronics Engineering

BITS Pilani, Pilani campus,

Pilani, Rajasthan, 333031, India

Date : _______________

Dedicated

To

My Parents

ACKNOWLEDGEMENT

Completion of my PhD is one of the biggest achievements in my life. I would not have been able to complete my PhD journey without the support of many people in the past 4 years.

I would like to thank my supervisor Dr. Sujan Yenuganti for his expert guidance, support and motivation throughout my PhD journey.

The time spent at BITS-Pilani was very enjoyable and inspiring. I wish to thank all my colleagues for creating a great working environment for in-depth technical discussions and valuable suggestions to cope with all sorts of difficulties. I would also like to thank my DAC members Prof. K. K. Gupta, Professor and Dr. Puneet Mishra, Assistant professor for their valuable suggestions and support all along.

I express my gratitude towards Prof. H D Mathur, Prof. V. K. Chaubey and Prof. Surekha Bhanot for providing me with valuable suggestions throughout my PhD. I am thankful to HoD EEE Department Prof. Navneet Gupta. I am also thankful to the Director of BITS Pilani, Prof. Sudhir Kumar Barai and the Vice-chancellor of BITS Pilani, Prof. V. Ramgopal Rao. I am also thankful to the Dean of Academic Graduate Studies and Research Division (AGSRD) Prof. M. B. Srinivas, Dean of Administration Prof. S. K. Verma, Associate Dean, AGSRD, Prof. Shamik Chakraborty and Registrar, Col. Soumyabrata Chakraborty (Retd) for giving me an opportunity to do the research in the area of my interest.

I am also grateful to my friends and colleagues Mr. Anukaran Khanna, Mr. Suraj Baloda, Dr. Sambhavi Shukla, Mr. PremSai Regalla, and Dr. Akhilesh Kumar Mishra who kept me inspired and helped in difficult times.

I would also like to thank my parents, Family and friends for their continuous support, motivation and encouragement without which I would not have been able to complete my PhD journey.

I would like to thank Mr. Ashok in the CNC machine lab for helping in the fabrication of the base of my sensor. I would also like to thank Mr. Tulsi Ram, Mr. Mahesh Chandra and Mr. Vijay Pratap Yadav for helping me to carry out my teaching assistantship.

It is a great pleasure for me to acknowledge and express my appreciation throughout my research work to all my well-wishers for their understanding, relentless support and encouragement. Last but not least, I would like to express my sincere gratitude to all those who helped me directly or indirectly at different stages of this work.

I would like to thank all my peers and seniors for their support and inspiration during the gamut of adverse times and to help me to overcome impasses. I would cherish happy moments spent with my friends at BITS Pilani campus for my whole life.

Sankalp Paliwal

ABSTRACT

The dissertation explores the design, modelling, simulation, fabrication, and testing of a Hall effect-based pressure sensor. The first work is on the design, analytical modelling, and simulation of a Hall effect-based pressure sensor to operate in the pressure range of 0-20 bar. The 3D model of the pressure sensor is designed using stainless steel and simulated in the COMSOL Multiphysics FEM tool. Complete analytical modelling is also carried out on the proposed design and compared with the numerical simulation results obtained from COMSOL software. The simulated pressure sensor design is custom fabricated with stainless steel as the base material and silicone rubber as the diaphragm material. Another design of the pressure sensor with a design variation is also fabricated. Both the designs of the pressure sensors have been tested in the pressure range of 0-1 bar for 25 cycles of ascending and descending pressure. The performance characteristics like non-linearity, hysteresis, repeatability, resolution, and sensitivity of both fabricated sensor designs are obtained and compared. The differential design has better linearity, repeatability, and hysteresis as compared to the other design. In the case of differential design regulated power supply is not required whereas, in the case of other sensor design, a fixed power supply is required for good repeatability. Moreover, the differential design does not require any temperature compensation against the change in ambient temperature.

The second work of the thesis is to design a wired and wireless transmitter for the fabricated sensor designs. A wired transmitter is designed by converting the sensor output firstly to a range of 1-5 V using a signal conditioning circuit. After the signal conditioning circuit, a V-I converter is used to convert the voltage output to a 4-20 mA current signal which can be transmitted using a wire to any remote indicator without data loss. A wireless transmitter is also designed in which the signal conditioning circuitry is similar to the wired transmitter. The output of the signal conditioning circuitry is given to the NodeMCU with a built-in Wi-Fi module which is used to wirelessly transmit the measured pressure data to the IoT cloud server. The Blynk IoT console is used as the server and the sensor data can be accessed from any PC/laptop with internet connectivity. The percentage nonlinearity and percentage error of the signal conditioning circuitry output and V-I converter output are calculated during the hardware implementation of the transmitters. The transmitted data and the received data are also compared and are found to be in close agreement.

In the third work, a digital output MEMS pressure sensor is designed and simulated in the pressure range of 0-1 bar. The sensor uses the diaphragm deflection and a simple mechanical

structure to convert the applied pressure to a logic digital output. Three different designs of the sensor have been proposed with square and circular diaphragms. The first design uses ten different-sized square diaphragms on the same substrate to get a resolution of 0.1 bar. The second design uses a single square diaphragm instead of ten to get the same resolution. The third design also uses a single circular diaphragm with a central boss structure, which reduces the deflection nonlinearity at low pressures. An analytical analysis is carried out for all the diaphragm deflections, and the results are supported by numerical simulations carried out in the COMSOL Multiphysics tool. The proposed sensor can operate on 5 V which suits well with conventional CMOS logic. The direct digital output from the pressure sensor makes it useful in a wide variety of applications.

Keywords: Pressure sensor, Hall sensor, Differential, Boss structure, MEMS, Digital Output, Transmitters

TABLE OF CONTENTS

CERTIFICATE……………………………………………………………………….i

ACKNOWLEDGEMENT…………………………………………………………..iii

ABSTRACT………………………………………………………………………..v

TABLE OF CONTENTS…………………………………………………………...vii

LIST OF FIGURES…………………………………………………………….....x

LIST OF TABLES………………………………………………………………….xiii

NOTATIONS……………………………………………………………………......xiv

ACRONYMS……………………………………………………………………….xv

Chapter 1…………………………………………………………………………..1

Introduction………………………………………………………………………..1

1.1 General Introduction………………………………………………………….1

1.2 Motivation……………………………………………………………………...5

1.3 Research Objectives…………………………………………………………...6

1.4 Main Contributions……………………………………………………………6

1.5 Organization of The Thesis…………………………………………………8

Chapter 2…………………………………………………………………………….10

Literature Review…………………………………………………………………..10

2.1 Introduction……………………………………………………………..…10

2.1.1 Piezoresistive Pressure Sensors………………………………………10

2.1.2 Capacitive Pressure Sensors…………………………………………….12

2.1.3 Resonant Pressure Sensors……………………………………………13

2.1.4 Optical Pressure Sensors……………………………………………...15

2.1.5 Hall Effect Based Sensors……………………………….……………….17

2.1.6 Transmitters……………..…………………………………………….19

2.1.7 Digital MEMS Pressure Sensors……..…………………………………21

2.2 Research Gaps…………………………………………………………………...21

Chapter 3………………………………………………………………………………23

Design, Modelling and Simulation of a Hall Effect Based Pressure Sensor………………23

3.1 Introduction……………………………………………………………………..23

3.2 Sensor Design and Principle……………………………………………………24

3.3 Analytical Modelling………………………………………………………….....25

3.3.1 Phase 1………………………………………………………………25

3.3.2 Phase 2 ………………………………………………………………30

3.4 Numerical Modelling……………………………………………………………32

3.5 Proposed Sensor Fabrication……………………………………………………...35

3.6 Results and Discussion……………………………………………………………..36

3.7 Conclusion……………………………………………………………………………39

Chapter 4………………………………………………………………………………40

Fabrication and Testing of a Hall Effect Based Pressure Sensor…………………………40

4.1 Introduction……………………………………………………………………..40

4.2 Design I…………………………………………………………………...……..40

4.3 Design II………………………………………………………………...…..…41

4.4 Sensor Fabrication and Integration…………………………………………….43

4.5 Experimentation…………………………………………...…………….45

4.6 Results and Discussion…………………………………………………………..47

4.7 Conclusion……………………………………………………………………….56

Chapter 5………………………………………………………………………………57

Wired and Wireless Hall Effect Based Pressure Transmitters…………………….……..57

5.1 Introduction……………………………………………………………………..57

5.2 Implementation of Wired and Wireless Transmitter…………………………58

5.2.1 Wired Transmitter……………………………………………………….58

5.2.2 Wireless Transmitter…………………………………………………….61

5.3 Experimental Results………………………………………………………63

5.3.1 Design I………………………………………………………………...65

5.3.2 Design II……………………………………………….…………….67

5.4 Conclusion……………………………………………………………………69

Chapter 6…………………………………………………………………………………70

Design and Simulation of Digital Output MEMS Pressure Sensor………………………70

6.1 Introduction…………………………………………………………………..70

6.2 Design and Principle of Operation……………………………………………70

6.3 Analytical Modelling……………………………………………………………75

6.4 Numerical Simulation………………………………………………………..78

6.5 Proposed Fabrication Steps…………………………………………………….80

6.6 Results and Discussion………………………………………………………….80

6.7 Conclusion……………………………………………………………………….83

Chapter 7…………………………………………………………………………………84

Conclusions and Scope for Future Work…………………………………………………84

7.1 Conclusions…………………………………………………………………….84

7.2 Scope for Future Work…………………………………………………………86

References……………………………………………………………………………...87

List of Publications…………………………………………………………………….....98

Brief Biography of the Candidate…………………………………………………….....99

Brief Biography of the Supervisor……………………………………………………...100

List of Figures

Fig. 3.1 Schematic of the pressure sensor structure (a) 3D view (b) side view……………...25

Fig. 3.2 Top view of the sensor diaphragm showing the central boss structure……………..26

Fig. 3.3 Variation in diaphragm central deflection for three different diaphragm thickness (a) 0.1 mm (b) 0.2 mm and (c) 0.3 mm…………………………………………….....29

Fig. 3.4 Diaphragm deflection of the sensor (a) under no pressure load (b) with pressure…….31

Fig. 3.5 Magnetic flux density at a certain distance from the permanent magnet……………..32

Fig. 3.6 Pressure sensor part II built in COMSOL (a) 3D model (b) meshed model…………32

Fig. 3.7 Variation of diaphragm central deflection with three different diaphragm thickness (a) 0.1 mm (b) 0.2 mm and (c) 0.3 mm…………………………………………..….34

Fig. 3.8 (a) The 3D model of a cylindrical permanent magnet (b) Distribution of magnetic flux density around the magnet……………………………………………………..……....35

Fig. 3.9 CAD drawing of the sensor (a) part II (b) part I and III………………………………36

Fig. 3.10 Comparison of analytical and numerical results of diaphragm central deflection with input pressure……………………………………………………………………....37

Fig. 3.11 Comparison of analytical and numerical results of magnetic flux density with input pressure…………………………………………………………………..…..39

Fig. 4.1 Side view of the pressure sensor…………………………………………………….41

Fig. 4.2 (a) Side view of the pressure sensor (b) Diaphragm deflection……………………42

Fig. 4.3 (a) CAD drawing of the SS tube adapter (b) Fabricated SS tube adapter……….......44

Fig. 4.4 Fabricated pressure sensor (design I)…………………………………………..…44

Fig. 4.5 Fabricated pressure sensor (design II)………………………………………………45

Fig. 4.6 Experimental setup for displacement-voltage characteristics of the Hall sensor……46

Fig. 4.7 Displacement-voltage characteristics of Hall sensor……………………………......46

Fig. 4.8 Experimental setup for calibrating the pressure sensor……………..………………47

Fig. 4.9 Input-output characteristics of the pressure sensor (a) design I (b) design II……….48

Fig. 4.10 %Nonlinearity of the pressure sensor (a) design I (b) design II……………………48

Fig. 4.11 Average output voltage of the pressure sensor (a) design I (b) design II……………49

Fig. 4.12 %Hysteresis of the pressure sensor (a) design I (b) design II………………………49

Fig. 4.13 Estimated pressure of the pressure sensor (a) design I (b) design II………………..50

Fig. 4.14 % Error of the pressure sensor (a) design I (b) design II……………………………50

Fig. 4.15 Repeatability of the pressure sensor (a) design I (b) design II………………………51

Fig. 4.16 Resolution of the pressure sensor (a) design I (b) design II…………….……………51

Fig. 4.17 First three vibration mode shapes of the diaphragm (design I)…..……………...…...53

Fig. 4.18 First three vibration mode shapes for design I …………………..…………………...54

Fig. 4.19 First three vibration mode shapes of the diaphragm (design II)……………………....55

Fig. 4.20 First three vibration mode shapes for design II……………………..…………………56

Fig. 5.1 Block diagram of a wired transmitter (design I)………………………………………...59

Fig. 5.2 Wired transmitter circuit implementation for design I ………………...…………..59

Fig. 5.3 Pin-out of AD620 Instrumentation amplifier IC ……….…………………….…….60

Fig. 5.4 Block diagram of a wired transmitter (design II)……………………………………..60

Fig. 5.5 Wired transmitter circuit implementation for design II……………………….…..60

Fig. 5.6 Block diagram of a wireless transmitter for design I…………….……..………..……61

Fig. 5.7 Block diagram of a wireless transmitter for design II……………………….…...62

Fig. 5.8 Wireless transmitter circuit implementation for design I………………….....……....62

Fig. 5.9 Wireless transmitter circuit implementation for design II………………..……….62

Fig. 5.10 Experimental setup of a wired transmitter for design II ………….......................….63

Fig. 5.11 Experimental setup of a wireless transmitter for design II…………………………..64

Fig. 5.12 NodeMCU……………………………………………………………………………..64

Fig. 5.13 Blynk IoT Console……………………………………………………….....65

Fig. 5.14 Signal conditioning circuit output (V_o)……………………………….………..……65

Fig. 5.15 V-I converter output (I)……………………………………………………..………66

Fig. 5.16 % Nonlinearity for V-I converter output…………….……………………….…………66

Fig. 5.17 % Error for V-I converter output…………………………………………..…..……66

Fig. 5.18 Signal conditioning circuit output (V_o)…………..…………………………..….67

Fig. 5.19 V-I converter output (I)…………..……………………………………………..……68

Fig. 5.20 % Nonlinearity for V-I converter output…………..…………….………..……68

Fig. 5.21 % Error for V-I converter output…………..………………….………………68

Fig. 6.1 Initial design of a single diaphragm of the sensor (a) side view (b) top view......…..71

Fig. 6.2 Diaphragm under applied input pressure…………………………………..……71

Fig. 6.3 Top view showing the diaphragm array of the initial sensor design.………….…..72

Fig. 6.4 Design I of the sensor (a) 3D view (b) top view…………………………..…...73

Fig. 6.5 Top view showing the diaphragm with protrusions and contact pads……………....74

Fig. 6.6 Design II of the sensor (a) 3D view (b) top view…………………………….………..74

Fig. 6.7 Top view showing the boss diaphragm with protrusions and contact pads…..…….75

Fig. 6.8 Equivalent circuit of a switch during ON and OFF state………………...……...75

Fig. 6.9 The top view of the square diaphragm…………………………..…..……………77

Fig. 6.10 The top view of the circular boss diaphragm……………………….…..……………77

Fig. 6.11 The meshed model of the sensor in COMSOL (a) design I and (b) design II……...78

Fig. 6.12 The simulation results for (a) initial design (b) design I (c) design II……………..79

Fig. 6.13 Proposed fabrication steps for initial design of the pressure sensor……………….81

Fig. 6.14 Diaphragm deflection for two side lengths (a) 527 μm and (b) 296 μm…………...82

Fig. 6.15 (a) Analytical results of the diaphragm deflection from C1 to C10 (b) Comparison of simulation and analytical results at C10…………………………………………82

Fig. 6.16 Comparison of diaphragm deflection for design II……………………….……..83

List of Tables

Table 2.1 Comparative study of pressure measurement techniques………………………...19

Table 3.1 Optimum dimension of the sensor for maximum central deflection of the diaphragm…………………………….………………………………………..30

Table 3.2 The variation in central deflection and magnetic flux density for 0-20 bar input pressure…………………………………………………………………….38

Table 4.1 Specifications of Hall sensor (SS 495A)…………………………………………46

Table 4.2 Comparison of static characteristics of fabricated sensors..………………………52

Table 4.3 Comparison of proposed sensor designs with other pressure sensors...……..……52

Table 4.4 Vibration mode frequencies for design I …………………………………………53

Table 4.5 Vibration mode frequencies for design II………………………………………....54

Table 5.1 Transmitted data vs Received data………………………………………….…….67

Table 5.2 Transmitted data vs Received data……………………………………...……69

Table 6.1 The logic table for various applied pressures……………………………………..73

Table 6.2 The side lengths and protrusion heights for all the sensor designs……………….78

NOTATIONS

$w(r)$	Deflection of circular diaphragm
ρ	Density of the diaphragm
P	Pressure
D	Flexural rigidity of the diaphragm
a	Radius of the diaphragm
b	Radius of central boss structure
t	Thickness of the circular diaphragm
ν	Poison's ratio
w_c	Diaphragm central deflection
B_i	Magnetic flux density
B_r	Flux density of the permanent magnet
V_h	Hall voltage
$w(x, y)$	Deflection of square/rectangular diaphragm

ACRONYMS

CAD	Computer Aided Design
CNC	Computer Numerical Control
FEM	Finite Element Method
GCP	Ground Contact Pad
IoT	Internet of Things
MATLAB	Matrix Laboratory
MEMS	Micro-electromechanical Systems
NodeMCU	Node Microcontroller Unit
OCP	Output Contact Pad
PDMS	Polydimethylsiloxane
SCP	Supply Contact Pad
SS	Stainless Steel
Wi-Fi	Wireless Fidelity

Chapter 1
Introduction

1.1 General Introduction

Sensing and measuring physical quantities like temperature, pressure, viscosity, level, and flow are very important in the industry. Among these parameters pressure sensing, monitoring and control are very important. Pressure sensors have various applications which are not only limited to process industries but also have applications in the automotive industry, robotics, aerospace industry, and bio-medical industry. Various types of pressure sensors are available in the literature. The most common types of pressure sensors are piezoresistive, piezoelectric, capacitive, resonant, and optical pressure sensors for measuring various ranges of pressure. Pressure sensors can also be designed using Hall effect sensors as secondary sensors that show some advantages compared with the existing pressure sensors available in the market. Very few works are available on Hall effect-based pressure sensors in the literature and this area has not been explored.

Hall effect is the generation of a potential difference called Hall voltage across a conductor which is transverse to an electric current flowing through the conductor and a magnetic field that is perpendicular to the current. The Hall effect was discovered by Edwin Hall in 1879. Hall effect sensors have various applications, and they are mostly used to detect and measure unknown magnetic fields. The key advantage of using Hall sensors is that they are highly robust and maintenance free. This makes use of Hall sensors efficient for applications like position sensors and for optical and electromechanical sensing.

There are various other contemporary applications of Hall effect based sensors for measuring various physical and electrical quantities. A split ring clamp-on sensor can be designed which is used to make temporary test equipment for current measurement [1]. The clamp on sensor can be clamped on any line where current is to be measured. The current flowing in a conductor will create a magnetic field due to which the Hall voltage will be generated and any change in current will change the Hall voltage according to the current value. Another application for Hall sensor is analog multiplication in which the output will be proportional to the Hall sensor voltage and the magnetic field [2]. Wheel rotation sensing which is widely useful for anti-lock braking systems is also done using Hall sensors [3]. During a rotational direction change, the phase difference of the magnetic field changes the polarity. The vertical dual Hall sensor detects this change and delivers a

corresponding signal. The Hall sensors are used as ignition timing devices which include a permanent magnet and semiconductor Hall effect chip which are mounted next to each other. A metal rotor consisting of a metallic window is mounted to a shaft. The shaft is arranged such that during rotation the window comes between the magnet and the Hall chip. A uniform square wave is produced when the window shields and exposes the Hall effect chip to the permanent magnet. The signal is used by the engine computer to control the ignition. Hall effect sensors are also used to design joysticks which are used to control hydraulic valves in industry and thus replace mechanical levers with contact less sensing.
Displacement measurement can also be done with the help of Hall sensors. If an arrangement is made such that the Hall sensor and a magnet attached to the shaft whose displacement is to be measured are kept in line, then as the distance between the shaft and the Hall sensor changes, it results in a change in the Hall voltage produced by the Hall sensor. Thus the unknown displacement of the shaft can be related to the Hall voltage. By using the same technique, we can measure the unknown external force on a specimen. If we assume the unknown force is applied to a spring mass system due to which the distance between the seismic mass and the Hall sensor changes hence, the Hall voltage also changes in correspondence to the force applied. Here the external force is converted to an equivalent displacement by the spring element in the system. The level of liquid in a tank can also be measured using Hall sensors. The level of liquid is measured by measuring the hydrostatic pressure that the liquid applies at the base of the tank using a diaphragm. A suitable mechanism can be developed using a diaphragm and Hall sensors for measuring this pressure and can be calibrated to measure the level in a tank. Similarly, pressure can also be measured by using a diaphragm as the primary sensing element to convert the pressure to displacement. On application of pressure, the diaphragm deflects and causes an out of plane displacement. This displacement can be utilized to produce a Hall voltage from a Hall sensor.

In industry, pressure sensors have to be used in extreme environmental and corrosive conditions. Stainless steel has high corrosive resistance and it is a good packaging material [4]. Stainless steel is a high alloy steel that consists of large amounts of chromium and some nickel and molybdenum. With 11% or greater amount of chromium confers the basic stainless-steel behavior of corrosion resistance. Molybdenum reinforces the effect of chromium and is present between 1% to 3%. The presence of nickel improves the resistance to corrosion in acidic media. In general, stainless steels are classified as ferritic, austenitic, duplex, martensitic, and precipitation-hardening stainless steels. Each has its own

corrosion characteristics. Ferritic stainless steel consist of chromium and sometimes molybdenum. Austenitic stainless steels consist of chromium and nickel to realize their excellent corrosion resistance. In addition, adding 3% molybdenum also improves resistance to chloride pitting and stress corrosion cracking. Duplex stainless steels are chromium-molybdenum alloys of iron with sufficient austenite stabilizers, nickel and nitrogen, to achieve a balance of ferrite plus austenite. Duplex stainless steels find use in more severe conditions of temperature and chloride content, where the usual austenitic grades are susceptible to pitting, crevice corrosion, and stress corrosion cracking. Martensitic and precipitation-hardening stainless steels are chosen primarily for high mechanical and tensile strength.

Diaphragms of many materials can be used for the design of pressure sensors. The most used materials are silicon and stainless steel. Other materials such as PDMS [5] and silicone rubber can also be used as diaphragms in pressure sensor design. Silicone rubber is an elastomer that is made of silicone a polymer made of silicon, carbon, hydrogen, and oxygen. The main advantages of using silicone rubber are its unique properties like non-reactive, stable, and resistant to extreme environments and temperatures. Silicone rubber can be used in the temperature range of -55 to 300^{0}C while maintaining its useful properties. Silicone rubber is highly inert and does not react with most chemicals and it can't participate in biological processes and hence can be used in many medical applications including medical implants. Due to the chemical stability of silicone rubber, it does not affect any substrate it is in contact including skin, water, blood, and other active ingredients which allows its large application in bio-sensors and also in wearable sensors [6]. Silicone rubber elongation at break is 100-1100% which shows it is quite flexible and its young's modulus is between 0.001-0.05 GPa and hence the deflection of the silicone rubber diaphragm is large, and the sensor made by silicone rubber is highly sensitive.

A measurement system consists of sensors that are used for data collection and the second part is data storage and transmission. The most popular form of signal transmission used in modern industrial instrumentation systems is the 4-20 mA DC standard. This is an analog signal standard to represent measurement or control signals. Typically, a 4 mA current represents 0% scale and 20 mA represents 100% scale. In pneumatic systems, a standard signal range of 3-15 psi (pounds per square inch) is used. Typically, a 3 psi pressure value represents 0% of the scale and 15 psi represents 100% of the scale. In the case of wired sensor data transmission, the data can be transmitted using cables like co-axial cables, optical cables, and LAN wires. In the case of wireless transmission, the most

common mode is to use radio waves in which data can be transmitted using amplitude modulation (AM), frequency modulation (FM), or pulse width modulation (PWM). Another technique for wireless data transmission is by using Wi-Fi LAN where data is transmitted using Wi-Fi to a local server and all the users connected to the server can access the data. The internet of things, or IoT, is a system of interrelated computing devices, mechanical and digital machines, objects, animals or people that are provided with unique identifiers and the ability to transfer data over a network without requiring human-to-human or human-to-computer interaction. An IoT ecosystem consists of web-enabled smart devices that use embedded systems, such as processors, sensors, and communication hardware, to collect, send and act on data they acquire from their environment. IoT devices share the sensor data they collect by connecting to an IoT gateway or other edge device where data is either sent to the cloud or analyzed locally. In the case of IoT, the sensor data is transmitted using Wi-Fi protocol to an internet cloud server from which data can be accessed from anywhere in the world by providing proper authentication.

In recent years MEMS pressure sensors have gained a lot of popularity. MEMS pressure sensors have a lot of applications in the process industry, biomedical applications and automotive and aerospace industries. MEMS pressure sensors are cheaper, faster and more reliable than mesoscale pressure sensors. The advantages of MEMS pressure sensors include small size, low power, high precision, and low cost. Most of the pressure sensors use a flexible diaphragm to convert the pressure into deflection and this deflection is transduced to an electrical output by using suitable sensing elements such as piezo resistors, capacitors, and resonators. The sensing elements in piezo resistors can be produced by doping suitable ions on the silicon wafer. These sensors have high sensitivity and show linear characteristics, but the output is dependent on temperature and requires temperature compensation through electronic circuits. Hysteresis, nonlinearity, and non-repeatability have a significant effect on the output in the case of the piezoresistive pressure sensors [7]. To address these limitations, many micromachined pressure sensors using capacitive sensing methods have been proposed. In general, capacitive pressure sensors are more sensitive to pressure and generally have less temperature dependence than piezoresistive ones [8]. The resonant pressure sensors operate by monitoring the resonant frequency shift of a vibrating structure, which is the main element in resonance-based sensors. The vibrating structure is made to vibrate at resonance conditions by suitable excitation and

detection units. The output frequency is commonly read out by electronic circuits (oscillator amplifier and frequency converter) which are integrated into the sensor cell.
Some applications require an easily transmittable digital output and hence digital MEMS pressure sensors are also gaining popularity in the industry. These types of sensors are free from the inherent disadvantages of conventional piezoresistive and capacitive pressure sensors. These types of sensors do not require any type of complex signal conditioning electronics. The direct digital output of the sensors makes them useful for tire pressure monitoring and process control applications. The output of the digital MEMS pressure sensor can be easily stored and analyzed without the requirement of ADC and DAC and hence making the overall system easy to design with low cost. Since the output is directly in digital form, the hysteresis present in the sensor output is less than the conventional sensors.

1.2 Motivation

Pressure sensors employed in applications such as automobiles, aerospace, downhole oil/gas logging equipment, and industrial process control are typically subjected to harsh environments, including high pressures, high temperatures, and corrosive media creating a challenge in the design of pressure sensors. Silicon based sensors with a silicon diaphragm as a wetted part used in corrosive media applications require complex protective packaging which increases the overall sensor cost, size, and limited operating temperature range. Silicone rubber diaphragms are chemically inert and stable in high operating temperatures up to 300^0C and can be used as an alternative option. The stainless steel packaging of the sensor allows the sensor to operate in the corrosive and high temperature range. The research on Hall effect based pressure sensors is relatively new with less literature available and also has a wide scope for improvement. Hall effect based pressure sensors are highly sensitive, linear, and can operate in a high-temperature range of up to 150^0C. The above discussed features of Hall sensor based pressure sensors like high linearity, high sensitivity, good repeatability, and the need for low-cost self-packaged sensors which can be used in a highly corrosive and harsh environment are the motivation factors to do research in the area of Hall sensor-based pressure sensors.
Numerous research efforts are put on even today in developing micro pressure sensors to meet the stringent needs in various fields. The majority of the micro pressure sensors use piezoresistive and capacitive sensing. These sensors have various problems like

temperature dependence, hysteresis, and nonlinearity. For storage and transmission of pressure sensor data, it required a complex and costly signal-processing electronics. The above reasons were the motivation to design a digital MEMS pressure sensor that directly provides the sensor output in digital form which can easily be stored and transmitted. Digital MEMS pressure sensors are easy to design and provide accurate results with fewer variations in the sensor output due to changes in environmental conditions. The output can be directly fed to a processor or controller for further processing without additional electronics like ADC and DAC.

1.3 Research Objectives

- To design a new diaphragm based pressure sensor by utilizing the Hall effect in a suitable arrangement.
- To develop a complete analytical model to come up with initial sensor dimensions before fabrication that is to be validated through FEM simulation.
- To undergo a custom fabrication of the pressure sensor based on the results from the analytical and FEM simulation along with another modified design.
- To calibrate both the fabricated pressure sensor designs and to compare their performance characteristics with other pressure sensors available in the literature.
- To design and implement wired and wireless transmitters for both the fabricated pressure sensor designs.
- To design and simulate a new digital output MEMS pressure sensor with some variations in the design to improve resolution and reduce nonlinearity.

1.4 Main Contributions

The main contributions of this thesis based on objectives are summarised as follows:

1. The design and simulation of a pressure sensor integrated with two identical hall sensors and permanent magnets arranged in a differential configuration for measuring pressure in the range of 0-20 bar was presented. The sensor uses the deflection of a circular diaphragm with a simple rigid mechanical structure to convert the applied pressure to a differential hall voltage output. Complete analytical modelling was carried out by assuming the rigid mechanical structure as a central circular boss structure on the circular diaphragm. Numerical simulations were also carried out in the COMSOL Multiphysics FEM tool to

support the analytical results. Before going for actual fabrication, the optimum sensor dimensions were also fixed from both analytical modelling and numerical simulation analysis. The sensor was planned to be fabricated completely using stainless steel material and hence it can be used in high temperature and corrosive environments. The fabricated sensor can be of low cost, simple in design and the differential arrangement helps to compensate for any ambient temperature variations.

2. The fabrication and testing of a pressure sensor integrated with Hall sensors and permanent magnets arranged in different configurations as two separate designs to measure pressure in the range of 0-1 bar was demonstrated. Two sensor designs were proposed with a single pair of Hall sensors and magnets and a differential configuration with two pairs of Hall sensors and magnets. Two sensor designs were custom fabricated and calibrated using a dead weight tester for 25 cycles of ascending and descending pressure in steps of 0.1 bar in the pressure range of 0-1 bar. Various static characteristics like nonlinearity, hysteresis, repeatability, sensitivity, resolution and error are estimated for both the sensor designs from the experimental results and then comparison has been done. The differential design was found to have better characteristics as compared to the other design. The differential arrangement of the sensor can aid in the compensation of ambient temperature variations and the use of stainless steel as a base material in fabrication enables its use in high-temperature and highly corrosive applications. The proposed sensor is low-cost, simple in design, and found to have high repeatability and good linearity compared to other similar Hall effect-based pressure sensors and also other types of pressure sensors available in the literature.

3. Wired and wireless transmitters were designed and implemented for the fabricated Hall effect based pressure sensors. In the implementation of a wired transmitter, the sensor output was converted to give an output in the range of 1-5V with the zero-gain span adjustment circuit. The output of this circuit was once again converted to an electric current signal with the help of a voltage-to-current converter circuit to give 4-20 mA output which can be easily transmitted to a remote indicator. The V-I converter output current in terms of pressure has been calculated and showed good linearity and accuracy for both pressure sensor

designs. Implementation of a wireless transmitter was also carried out using a NodeMCU with an in-built Wi-Fi module and the Blynk IoT cloud console is used as an IoT cloud server for storing and accessing the sensor data. For the wireless transmitters, the transmitted voltage from NodeMCU and the received voltage shown in the Blynk IoT console was found to be in good agreement.

4. The design and simulation of a MEMS pressure sensor with a digital output for measuring pressure in the range of 0-1 bar was presented in this work. The sensor uses the diaphragm deflection and a simple mechanical structure to convert the applied pressure to a logical digital output. Three different designs of the sensor have been proposed with square and circular diaphragms. The first design uses ten different-sized square diaphragms on the same substrate to get a resolution of 0.1 bar. The second design uses a single square diaphragm instead of ten to get the same resolution. The third design also uses a single circular diaphragm with a central boss structure, which reduces the deflection nonlinearity at low pressures. Analytical analysis was carried out for all the diaphragm deflections, and the results are supported by numerical simulations carried out in the COMSOL Multiphysics tool. The proposed sensor can operate on 5V which suits well with conventional CMOS logic. The direct digital output from the pressure sensor makes it useful in a wide variety of applications.

1.5 Organization of The Thesis

The thesis is organized as follows: Chapter 2 reviews detailed literature pertaining to various types of pressure sensors- piezoresistive, capacitive, resonant, optical, and Hall effect based sensors. It also reviews papers for wired and wireless sensor data transmission and papers related to digital MEMS pressure sensors. Based on the literature, research gaps were identified and included in this chapter. In Chapter 3, the Design and simulation of a Hall effect based pressure sensor is presented. A detailed modelling of the pressure sensor is also provided in this chapter. In Chapter 4, the fabrication and testing of two different effect based pressure sensor designs are demonstrated, and the testing results of both sensors are compared. In Chapter 5, wired and wireless transmitters are designed and implemented for the fabricated pressure sensors. In Chapter 6, the design and simulation of a digital MEMS pressure sensor are presented with three different designs. Detailed

analytical modelling and numerical simulation of all three designs are discussed along with the results. The conclusions are summarised along with suggestions for future research work in Chapter 7.

Chapter 2
Literature Review

2.1 Introduction

Related literature pertaining to the work done in this thesis is presented in this chapter. It is not intended to cover all the reported literature but includes the most important sources which motivated to carry out this research work.

2.1.1 Piezoresistive Pressure Sensors

Piezo resistive pressure sensors are the most popularly used sensors in the industry for pressure measurement. In piezoresistive pressure sensors, the resistance of the piezoresistive material changes when it is deformed on the application of external pressure. The basic principle of the piezoresistive pressure sensor is that when pressure is applied on a piezo resistor its resistivity changes. The piezo resistor can be fabricated by selective ion doping on a silicon diaphragm which will provide a change in resistance on the application of pressure. This change in resistance can be converted to a voltage signal with the help of a Wheatstone bridge circuit. The change in resistance is typically given by the equation below where π_l and π_t are piezoresistive constants and σ_l and σ_t are longitudinal and transverse stress components due to the applied pressure.

$$\frac{\Delta R}{R} = \pi_l \sigma_l - \pi_t \sigma_t \tag{2.1}$$

A piezoresistive pressure sensor in the pressure range of 0-2.5 MPa is demonstrated [9]. The piezoresistor thickness and positions were optimized using numerical simulation. A piezoresistive pressure sensor with a square diaphragm and a rectangular boss-type structure is presented in [10]. The sensor showed a sensitivity of 35mV/V FSO and a Non-linearity of 0.05%. A silicon diaphragm-based piezoresistive pressure sensor is designed by R. Singh *et al.* [11]. In this paper, a square diaphragm made of monocrystalline silicon is used and fabricated by etching the bulk silicon till the required thickness of the diaphragm is achieved. Four piezo resistors are fused on the surface of the diaphragm close to the edges. A novel high sensitivity and a linear piezoresistive pressure sensor for environmental applications in the pressure range of 0-1 MPa is developed [12]. The paper proposed two designs of the sensor, one with a square diaphragm and one with a rectangular diaphragm. The study shows that deflection in the case of the square diaphragm is more, whereas stress on the edges is more in the case of the rectangular diaphragm. A

piezoresistive pressure sensor for low pressure is demonstrated [13]. The sensor is designed and fabricated using a crossbeam membrane and peninsula (CBPM) diaphragm for low-pressure measurement. A piezoresistive pressure sensor with high sensitivity is designed for ultra-low differential pressure measurement [14]. The pressure range is from 0-0.5 kPa and showed a sensitivity of 34.5mV/kPa and Non-linearity of 0.81% FS. The major problem with piezoresistive pressure sensors is the variation of output with temperature change. To overcome this problem, temperature compensation is required to get an accurate reading of pressure. A passive technique for temperature compensation is presented [15]. In this technique, polysilicon resistors with negative temperature coefficients are fabricated along with piezo resistors. The aim is to make the temperature coefficient of sensitivity to be zero and hence there is no variation in the output with variation in temperature. The accuracy of the piezoresistive sensors is improved by signal conditioning with the help of an alternative current loop circuit [16]. A smart piezoresistive pressure sensor is fabricated using a microcontroller [17]. The microcontroller helps in the temperature compensation of the sensor and improves linearity. The microcontroller also helps in sensor data storage and transmission. A flexible piezoresistive pressure sensor array is designed using graphene dioxide foam and silicone elastomer [18]. The sensor array is designed on a flexible PCB and the range of the sensor is 0-30 kPa. A flexible piezoresistive pressure sensor is fabricated using wrinkled PDMS with silver nanowires (AgNWs) [19]. The paper also shows that by modifying the PDMS microstructure sensors with different sensitivity and ranges can be designed. A piezoresistive pressure sensor for the detection of low pressure (less than 100 Pa) is developed using PDMS microstructure with polypyrrole (PPy) and gold electrode [20]. A flexible piezoresistive pressure sensor is designed with high sensitivity [21]. The sensor is made of hybrid porous microstructures, which are fabricated using Epipremnum aureum leaf and sugar as templates. An implantable piezoresistive pressure sensor for biomedical applications is demonstrated [22]. The sensor is energy efficient and is coupled with a wireless link for data transmission. This method is significantly useful in biomedical applications where the patient's physical properties change slowly, such as glucose concentration, intraocular pressure, etc.

2.1.2 Capacitive Pressure Sensors

The capacitive pressure sensor measures pressure by measuring the change in capacitance. A capacitor consists of two parallel conducting plates separated by a small distance and filled with a dielectric medium. The capacitance of the capacitor is directly proportional to the permittivity of the dielectric medium and the cross-section area of the plates. The capacitance is inversely proportional to the distance between the plates of the capacitor. The capacitance of the capacitor can be varied by changing any of the three parameters, i.e, the permittivity of the dielectric medium, the cross-section area of the plates and the distance between plates. The easiest way to change the capacitance is by varying the distance between the plates. The capacitive pressures sensor is also designed on the same principle by making one or both plates as a flexible diaphragm which deforms on the application of the pressure. When the diaphragm deforms the gap between the plates changes and the capacitance changes, which can be measured and calibrated in terms of the applied pressure.

The use of capacitive pressure sensors is very popular and a lot of literature is available on. A low-pressure capacitive pressure sensor in the pressure range of 60 kPa is developed [23]. The sensor consists of a fixed frame and a silicon diaphragm which gets deflected when pressure is applied and thereby changing the capacitance. An analytic analysis of a capacitive MEMS pressure sensor is presented under dynamic load [24]. The analysis is done using the Differential Transformation Method (DTM) and the Runge-Kutta method. The design of a MEMS-based capacitive pressure is developed for use in harsh environments [25]. The sensor has a metal-insulator-metal type design in which the structure is designed using gold and silicon nitrate is used as a dielectric medium and the diaphragm is also made of gold. The sensor simulation is done in COMSOL Multiphysics software and a graph showing variation between input pressure and change in capacitance is presented. The sensor can withstand a pressure of 1500 MPa. A MEMS capacitive pressure sensor is demonstrated with a CMOS read-out circuit [26]. The sensor is formed on a CMOS chip by using a post-CMOS MEMS process. A capacitive pressure sensor is fabricated on stainless steel chip with a pressure range of 0-250 mmHg for bio-medical applications [27]. The sensor is microfabricated through thermal bonding of the chip dies made of medical grade stainless steel to the Au-polyimide diaphragm film. A CNT-based stretchable capacitive pressure sensor is designed in the pressure range of 0-4 kPa for application in soft robotics, E-skin and medical monitoring [28]. The sensor is based on

flexible electrodes with a wrinkled structure and composite dielectric layer. Capacitive pressure sensors for various applications are also available in the literature. A capacitive MEMS pressure sensor array is developed for the measurement of heart rate [29]. The sensor array is mounted on the wrist so that radial arterial blood flow during contraction and expansion of the heart deflects the diaphragm of the sensors. A CMOS-based capacitance-to-voltage converter is also designed, which indicates the change in pressure in terms of voltage. A MEMS-based clamped capacitive pressure sensor is designed for blood pressure measurement [30]. The operating range of the pressure sensor is between 0-0.16 MPa. The dielectric medium used for the design of the sensor is silicon nitrate. A MEMS capacitive pressure is fabricated for tire pressure measurement with high sensitivity [31]. The sensor is designed with a stepped diaphragm made of polysilicon. The stepped design of the diaphragm increases the sensitivity and linearity of the sensor. A capacitive pressure sensor for aircraft engine health monitoring is also developed [32]. The electronic circuit is based on a Clapp-type oscillator that incorporates a 6H-SiC MESFET, a SiCN MEMS capacitive pressure sensor, titanate MIM capacitors, wire wound inductors, and thick film resistors. The sensor acts as a capacitor in the LC tank circuit, thereby linking pressure to the resonant frequency of the oscillator.

2.1.3 Resonant Pressure Sensors

A resonant sensor is a device with an element vibrating at resonance, which changes its resonant frequency as a function of a physical or chemical parameter. The physical effects used by these types of sensors are based on the modification of one of its mechanical properties. The two principal modifications used within the framework of resonant sensors are the variation of the resonance frequency resulting from the mass modification of the system or the stiffness variation of the system. The resonant sensor element can take a number of forms, such as a cantilever, a double-ended tuning fork or a singly clamped beam. A cantilever operating in the dynamic mode, i.e., resonance frequency mode, is essentially a mechanical oscillator. From the simple classical model, the frequency of an oscillating cantilever is $f = \frac{1}{2\pi}\sqrt{\frac{k}{m}}$ where k is the spring constant and m is the effective mass of the cantilever. The major advantage of resonant sensors among the sensors producing frequency output is that the output is dependent on mechanical parameters and electronic effects contribute minimally to the performance of the device. In resonant

pressure sensors, the resonant frequency is varied by changing the stiffness of the system by applying pressure.

Pressure sensors which depend on vibrating structures for sensing, work on the principle of resonance frequency shift with applied pressure, are resonant pressure sensors and are advantageous over other conventional sensing techniques. The key advantage is that the frequency output is essentially in digital form and therefore can be easily integrated with digital electronics and other instrumentation systems. A low cost self-packaged piezoelectric resonant pressure sensor made of stainless steel metal is designed, fabricated and tested [33]. The sensor consists of a sensing diaphragm, inclined trusses, vertical mounts, and a resonating beam. The deflection of the diaphragm is transferred to the resonating beam with the help of specially designed trusses and mounts. A wide-range resonant pressure sensor is demonstrated with high sensitivity [34]. The sensor is based on the veering phenomenon in which multiple modes of vibrations are tracked for an electrothermally heated initially curved micro-beam. The first three modes of vibrations are used in the sensor. A piezoelectric pressure sensor based on a thickness shear mode crystal resonator in the pressure range of 0-45 psi is developed [35]. In this sensor, an AT-cut quartz crystal resonator with a beat frequency method is used for temperature compensation up to 60 ^{0}C. The design and testing of a langasite crystal-based pressure sensor operated in dual mode is presented [36]. The design of the sensor utilizes a doubly rotated cut piezoelectric langasite (LGS) crystal resonator with temperature compensation. The sensor can simultaneously measure pressure and temperature by utilizing the dual mode nature of the doubly cut langasite crystal resonator. A dual-mode thickness quartz pressure sensor is designed for high-pressure applications for use in oil and gas explorations [37]. The pressure sensor uses a doubly rotated Stress-compensated for the B-mode and temperature compensated for the C-mode cut disc resonator sandwiched between two matching end caps. A MEMS-based resonant pressure sensor using a silicon island-compliant mechanism supported frequency tuneable resonating beam-based micro pressure sensor is proposed [38]. The sensor consists of a silicon frame that supports the silicon nitride resonating beam placed diagonally on the island in a square diaphragm made of silicon. A micromachined resonant pressure sensor composed of an SOI wafer as the sensing element with a glass-on-silicon cap for vacuum packaging is demonstrated [39]. In this design of the sensor two resonators are used on the central and side areas of the diaphragm. A micro resonant pressure sensor is designed with three degrees of freedom [40]. The sensor has a silicon diaphragm with silicon islands supporting a three degree of

freedom resonator beam made of silicon nitride. A differential resonant pressure sensor is demonstrated with high accuracy using the linear fitting method [41]. Theoretical methods have been proposed to improve the linearity of the sensor. A pressure sensor with balanced mass dual-ended tuning fork resonators and a twinborn diaphragm is presented [42]. The design reduces thermal stress and out-of-plane displacement of the vibrating beams of the resonator. A resonant pressure sensor is designed with on-chip temperature and strain sensors for error correction [43]. The sensor is designed to reduce temperature and stress-induced errors in the sensor. The sensor has three resonators on the shared diaphragm to independently capture pressure, temperature and stress signals and the errors in the pressure signal can be compensated. A resonant pressure sensor with in- plane mode vibration and piezoresistive detection is demonstrated in [44]. A unique piezoresistive detection method based on small axially deformed beams with a resonant status is proposed, and other adjacent mode outputs are easily shielded. A wireless pressure sensor is designed by integrating a surface acoustic sensor with a bourdon tube [45]. The SAW (surface acoustic wave) sensor is used as a secondary sensor which provides a signal in terms of frequency shift proportional to the pressure applied. A piezoelectric pressure sensor is presented for hypersonic flow measurement [46]. The sensing diaphragm of the sensor is a composite stack of Si, SiO_2 and Aluminium Nitride. A piezoelectric sensor for muscle contraction estimation is developed [47]. The sensor is designed to measure voluntary muscle contraction, which provides motion action information of the body useful for designing a human-robot interaction system. A wireless embedded resonant sensor is designed using the standard low-temperature co-fired ceramics (LTCC) technology [48]. The use of LTCC technology enables the sensor to be used in high-temperature and chemically aggressive environments.

2.1.4 Optical Pressure Sensors

In optical pressure sensors, the pressure is measured as a change in the intensity of light received. The sensor is designed such that when pressure is applied, the sensor blocks the path of light changing the intensity of light received. This change in intensity is calibrated in terms of applied pressure. Some optical pressure sensors also use interferometry to measure changes in paths and phase of light that are caused by the applied pressure and this change in phase is calibrated in terms of applied pressure. Optical pressure

sensors are not sensitive to environmental temperature hence the readings of these types of sensors do not vary with temperature.

Optical pressure sensors are widely used in Research laboratories. A GaAs-based fiber optic pressure sensor is designed to measure hydrostatic pressure up to 100 MPa [49]. The sensing element is composed of a pure GaAs single crystal configured in the form of a micro-prism and is placed at the sensor tip. The sensor also has attached two multimodal optical fibers, one for the input light and the other for the pressure-modulated light signal. An electro-optic type of pressure sensor is designed with bellows as a primary sensor [50]. The sensor uses a Mach-Zender interferometer (MZI) for pressure transmission. In the primary part of the sensor, a magnet is attached to the bellow, and a Hall sensor is fixed directly above the bellow. As pressure is applied, the distance between the magnet and the Hall sensor is reduced and a corresponding voltage signal is generated. This signal is provided to MZI, and the intensity of the light is modulated due to the electro-optic effect. A fiber optical pressure sensor is developed based on tunable liquid crystal (LC) technology [51]. A low-index LC is used as a tuneable birefringent cladding of the fibre. A lossy mode resonance (LMR) based fibre-optic pressure sensor is also demonstrated [52]. The designed sensor works in reflection mode, wherein the sensing signal is measured in terms of retro-reflection spectra. An optical pressure measurement system for intraocular pressure measurement is developed in the pressure range of 0-60 mm of Hg [53]. The system consists of a hermetically sealed, biocompatible, wireless, and powerless interferometric pressure sensor and a portable handheld reader. The interferometric pressure sensor consists of a 200 nm silicon nitride diaphragm, a 10 μm SU-8 spacer, and a 200 μm glass substrate. An optical pressure sensor is designed using dual waveguide Bragg gratings on the diaphragm [54]. The sensor consists of a curved waveguide with two identical waveguide Bragg gratings (WBGs) on the diaphragm. The pitch of the gratings changes when the pressure is applied and hence there is a shift in Bragg wavelength according to the pressure applied.

Apart from piezoresistive, capacitive, piezoelectric and optical pressure sensors, there are some other types of pressure measurement systems available in the literature. An all-elastomer pressure sensor using a printed carbon nanotube is presented [55]. The sensor developed is highly sensitive and is composed of PDMS and carbon nanotube as the sensing element. The carbon nanotube is inkjet printed on polyethene terephthalate (PET) film and then transferred to PDMS. An ANN-based pressure transducer is demonstrated [56]. The primary sensor used is a bellow which converts pressure into displacement. The

displacement is converted to a voltage signal using an inductive pickup. An op-amp-based inductive signal conditioning circuit is designed to produce a voltage proportional to changes in self-inductance. This signal has a considerable non-linearity error which is improved by ANN modelling.

2.1.5 Hall Effect Based Sensors

Hall effect is the generation of a potential difference called Hall voltage across a conductor, which is transverse to an electric current flowing through the conductor and a magnetic field which is perpendicular to the current. The Hall effect was discovered by Edwin Hall in 1879. Hall effect sensors have various applications, and they are mostly used to detect and measure magnetic fields. Hall effect sensors can also be used to design position and displacement sensors. Hall sensors can also be used as secondary sensor for pressure measurement.

Hall sensors have various applications and numerous Hall effect-based sensors are present in the literature. Hall sensors can be used to design magnetic sensors as described in [57]. The sensor is designed using Fe-Pt alloy with various thin film thicknesses and Fe concentrations for magnetic sensitivity applications at low frequencies. A system-on-chip (SoC) Hall sensor is designed to measure current which includes Hall sensor elements, preamplifiers, ADC, DAC and digital calibrator [58]. The SoC integrates a digital correction unit that implements a polynomial computation algorithm to calibrate the current sensor's magnetic core-induced nonlinearities. Hall sensors can be also used for position measurement in motors. A Hall sensor-based position sensor is designed for a permanent magnet synchronous linear motor [59]. The measurement model with the Fourier series is employed to approximate the mapping relationship between magnetic field strength and mover position. A Hall effect-based sensor is designed to measure the displacement of a miniature magnetically levitated rotor [60]. The measurement system consists of six Hall sensors attached to the stator and a ring-shaped permanent magnet mounted on the rotor. The system is designed in such a way that the direction of the magnetic flux into the sensors for each axis are monitored. A Hall sensor-based velocity meter is presented for UAV indoor navigation [61]. The navigation of a UAV requires aiding measurements such as position, velocity and altitude. The sensor is designed to measure the velocity of a quadcopter UAV. A Hall effect-based sensor is designed to measure torque for rotating shafts [62]. In the system, two permanent magnets are attached

to the rotating shaft and the Hall sensor is placed on the stationary unit close to the shaft. The relative movement between the magnets increases or decreases the magnetic field sensed by the Hall sensors that can be calibrated in terms of the torque of the rotating shaft. Hall sensors can also be used as secondary sensors for pressure measurement. Semiconductor Hall sensors are immune to dirt and moisture hence less maintenance is required for these types of sensors. The operating temperature range of these sensors is normally higher than normal piezoresistive sensors. A pressure sensor using bellow as the primary sensor and a Hall sensor as the secondary sensor is presented [63]. A magnet is placed on top of the bellow and a Hall sensor is fixed above the bellow with some gap between the magnet and Hall sensor. When pressure is applied, the distance between the magnet and the Hall sensor changes and the output voltage of the Hall sensor also changes. The Hall voltage output is corresponding to the pressure applied. The transmitter for the sensor is also designed by converting the output into a 4-20 mA signal using a signal conditioning circuit. A non-contact type pressure sensor using Hall sensors and a bourdon tube is developed [64]. In this sensor design, a Hall sensor is attached to the aluminium casing of the bourdon gauge and a permanent magnet is attached to the free end tip of the bourdon tube. When the pressure is applied the free end tip of the bourdon tube moves closer to the Hall sensor attached and hence changing the output of the Hall sensor corresponding to the pressure applied. A signal conditioning circuit for temperature compensation is also designed. A fingertip pressure sensor is designed using a Hall sensor in the pressure of 0-90 kPa is fabricated and tested [65]. The sensor is designed for accurate measurement of pressure for robotic gripping operations. An omnidirectional pressure sensor using a cone-shaped magnetic slider and a Hall sensor is included in the designed. when the pressure is applied to the fingertip, the magnetic slider moves the magnet closer to the Hall sensor which changes the output of the Hall sensor corresponding to the pressure applied. The Hall sensor is embedded in a flexible elastomer which guarantees pressure measurement from all sides of the fingertip. A magnet-based pressure sensor is designed using PDMS and a Planar Hall resistive (PHR) sensor in the pressure range of 0-20 kPa [66]. The micro-structured PDMS of 1 mm thickness is sandwiched between the magnet and the PHR sensor. The pressure is applied on the magnet side of the sensor hence deforming the PDMS and reducing the distance between the magnet and the Hall sensor and changing the Hall sensor output voltage corresponding to the pressure applied. This sensor can be used as a wearable sensor for heart rate measurement. A MEMS Hall effect-based pressure sensor in the pressure range of 0-110 kPa is presented [67]. The sensor

design consists of a membrane, a cavity for pressure measurement, a permanent magnet and ohmic contacts for voltage measurement. When the current flow between two input ports a voltage is generated due to the Hall effect. When pressure is applied the membrane deflects and moves closer to the magnet and thereby producing corresponding hall voltage. A highly sensitive giant magnetoresistance (GMR) sensor-based pressure sensor is fabricated and tested in the pressure range 0-300 Pa [68]. In this design a permanent magnet is attached to a silicone elastomer diaphragm and a GMR sensor is placed on the base of the sensor below the diaphragm. In the case of a GMR sensor when the magnetic field is changed resistance of the GMR sensor changes. The change in resistance can be reflected in terms of a voltage signal with the help of a Wheatstone bridge. When pressure is applied to the diaphragm, the diaphragm deforms and produces a corresponding hall voltage which can be related to the pressure. A comparative study of the pressure sensors discussed in the literature is presented in Table 2.1.

Table 2.1 Comparative study of pressure measurement techniques

Parameters	Piezoresistive	Capacitive	Piezoelectric	Optical	Hall Effect based
External power supply	DC	AC	AC	AC	DC
Cost	low	High	High	High	Low
Fabrication	Complex	Simple	Complex	Complex	Simple
Operating Temperature	Up to 80ºC	Up to 200ºC	Up to 100ºC	Up to 800ºC	Up to 150ºC
Linearity	Linear	Non-linear	Linear	Linear	Linear

2.1.6 Transmitters

Sensor data transmission is an important aspect in all the process industries. The sensor data transmitted can be used to monitor the process variable or for controlling the variables like temperature, pressure, flow, etc. Sensor data transmission becomes more useful in the case of hazardous industries where a human operator is not allowed to go near the sensors. The data transmission used in industry at the current time can be both wired and wireless. In the case of wired sensor data transmission, the data can be transmitted using cables like co-axial cables, optical cables and LAN wires. In the case of wireless transmission, the most common mode is by using radio waves in which data can be

transmitted using amplitude modulation (AM), frequency modulation (FM) or pulse width modulation (PWM). Another technique for wireless data transmission is by using Wi-Fi LAN, where data is transmitted using Wi-Fi to a local server and all the users connected to the server can access the data. The most emerging technology in sensor data transmission is the internet of things (IoT). In the case of IoT, the sensor data is transmitted using Wi-Fi protocol to an internet cloud server from which data can be accessed from anywhere in the world by providing proper authentication.

Various sensor data transmission techniques are available in literature. An electronics level transmitter based on the measurement of hydrostatic pressure is designed and developed [69]. The level sensing is done by measuring the hydrostatic pressure at the base of the container using Hall sensors. A wired transmitter is designed with the help of signal conditioning circuitry that includes instrumentation amplifier, a zero, gain and span circuit and a voltage to current converter circuit. The signal conditioning circuit converts the sensor data in the form of 4-20 mA current signal and then it is transmitted to a remote indicator. A similar electronic level transmitter is also designed using inter digital capacitor [70]. The level is measured using inter digital capacitor as a primary sensing element. The change in capacitance with level is converted to electrical signal with the help of a suitable bridge circuit. The signal from the bridge is passed through a precision rectifier circuit to convert to a DC signal. The DC signal is given to a zero, gain and span circuit to convert the signal in the range of 1-5V. The signal is then given to a voltage to current converter circuit which converts the signal to a 4-20mA current signal which is transmitted to a remote indicator. A wireless sensor network for temperature measurement in hostile environments is demonstrated [71]. A highly reliable network architecture is designed based on a distributed coordinator. In [72] a wireless air flow transmitter is designed using resistive type flex band sensor to sense the airflow. The data is transmitted wirelessly with the help of an Arduino microcontroller and ESP8266 Wi-Fi module. In [73] an air quality monitoring system based on Internet of things (IoT) is presented. The system monitors components of air quality such as temperature, humidity, CO and CO_2. LPWAN Lora was used for data transmission and for cloud services. A wireless sensor network based on IoT for precision agriculture is designed and various parameters helpful for agriculture are monitored using wireless sensor nodes [74].

2.1.7 Digital MEMS Pressure Sensors

MEMS sensors have become popular for use in most of the process industries. Because of their small size, MEMS sensors can be easily placed in inaccessible regions. The sensors provide accurate results, are easy to design and are low-cost due to batch production. There are applications which require an easily transmittable digital output and hence digital MEMS pressure sensors are also gaining popularity in the industry. These types of sensors are free from the inherent disadvantages of conventional piezoresistive and capacitive pressure sensors. These types of sensors do not require any type of complex signal conditioning electronics. The direct digital output of the sensors makes them useful for tire pressure monitoring and process control applications. The output of the digital MEMS pressure sensor can be easily stored and analyzed without the requirement of ADC and DAC and hence making the overall system easy to design and of low cost. Since the output is directly in digital form, there is less hysteresis present in the sensor output.

Many MEMS sensors provide a digital output and various literature is present on them. A MEMS-based gyroscope is designed with a digital readout [75]. The MEMS sensor design is integrated with a highly programmable capacitive interface ASIC for providing a digital output. A MEMS-based first-order sigma-delta analog-to-digital converter for a resistive sensor is presented [76]. The CMOS circuit for the ADC is designed using cadence silterra 0.13 µm standard CMOS process. The designed ADC reduces the quantization error as compared to the conventional ADC. A MEMS accelerometer with digital output is designed with ultra-low power consumption [77]. The device comprises of several acceleration switches (equal to the number of bits of resolution), which are coupled to each other via electrostatic actuators.

Various MEMS-based pressure sensors with digital output are also present in the literature. A CMOS-based MEMS pressure sensor is presented with a compact size and a digital readout [78]. The sensor designed is a capacitive pressure sensor with a square diaphragm. The CMOS circuit for providing a digital output with a 10-bit SAR ADC is designed on the same chip. A digital MEMS pressure sensor using capacitance to time converter is designed [79]. The MEMS transducer has been designed and fabricated using the Metal Mumps process from MEMSCAP. A capacitance-to-digital converter has been designed and fabricated in a low-cost 2P4M 0.35µm CMOS standard process as a digital interface to the MEMS sensor. A MEMS PWM pressure sensor with a cantilever switch and a SOI diaphragm is developed [80]. The proposed system converts the applied pressure into a

PWM signal. The pressure applied on the silicon diaphragm is converted to a PWM signal with the help of a metallic cantilever and metallic contacts attached to the diaphragm which comes in contact with the cantilever when pressure is applied. An implantable piezoresistive pressure sensor with a digital readout circuit was proposed [81] which is insensitive to temperature and uses low power for operation. A novel readout circuit suitable for temperature compensation has been demonstrated using the PWM technique in a piezoresistive pressure sensor by Jun [82]. Various types of digital readout methods were proposed, where the pressure is converted into frequency which can be seen in the literature [83, 84]. These methods, though generate digital output, have their own drawbacks. Hence, the development of a MEMS pressure sensor that has a simple structure and needs no complex signal conditioning and processing electronics for producing digital output should be an ideal alternative to the existing sensors. Such sensors should possess all the advantages of piezoresistive and capacitive sensors but effectively do not suffer from their disadvantages. A micro-electro-mechanical systems (MEMS) pressure sensor based on PWM technique was proposed which converts the applied pressure into an equivalent PWM signal with a simple structure [85]. A new concept of a low-power piezoelectric MEMS-based digital logic process was also proposed and studied [86].

2.2 Research Gaps

- Piezoresistive pressure sensors show linear responses but are sensitive to temperature variation. These sensors are generally not suitable for use in high temperature.
- Capacitive pressure sensors are robust but show a nonlinear response which makes the calibration difficult and have a complex readout circuitry.
- Tracking of resonant frequency in resonant pressure sensors is difficult and has some fabrication constraints.
- The read out equipment for optical pressure sensors are bulky, and generally, these types of pressure sensors are expensive.
- Hence, there is a need for a pressure sensor that shows good linearity, which is of low-cost, easy to design, has simple electronic readout circuitry, and can be operated in high temperatures with good sensitivity and repeatability.

Chapter 3

Design, Modelling and Simulation of a Hall Effect Based Pressure Sensor

3.1 Introduction

Measurement and monitoring of pressure is one of the most critical tasks in all the process industries. Numerous sensors were proposed in the literature to measure various physical parameters including pressure using the Hall effect as primary or secondary sensing element. Some of the most recent sensors using the Hall effect are displacement sensors [87] and magnetic field sensors [88], in which the Hall effect sensor/probe plays a role of a primary sensing element. A few pressure sensors were also available in literature which use Hall sensor/probe as a secondary sensing element to convert the displacement from the primary transducer (a flexible diaphragm) to a corresponding Hall voltage output. A pressure sensor using the bellows element as a primary transducer and a Hall sensor/probe acting as a secondary transducer was demonstrated [63]. The applied input pressure makes the bellows element to displace a permanent magnet due to which there will be a change in the magnetic flux density and hence a Hall voltage will be generated by the Hall probe that can be related to the applied pressure. Instead of a bulky and heavy bellows element, a simple C-shaped Bourdon tube was used as the primary transducer along with a Hall effect sensor/probe for pressure measurement proposed by Sirshendu et al. [64]. A MEMS pressure sensor based on the Hall effect using SOI diaphragm as a primary transducer was designed and tested [67]. It was also proved that the output Hall voltage is linear with the applied input pressure. In another pressure sensor design, the Hall sensor has been replaced by giant magnetoresistance (GMR) sensor [66]. The sensitivity of the GMR sensor is much higher than the Hall sensor but also more expensive than the Hall sensor. Also, to measure pressure in harsh environments, pressure sensors use stainless steel for packaging and completely packaged sensors have been found in the literature.

In this chapter, a pressure sensor comprising a circular diaphragm with a T-shaped structure as a primary transducer and two identical Hall sensors as secondary transducers along with two permanent magnets in a differential arrangement was designed, modelled, and simulated. Combining the Hall effect in a differential arrangement for pressure sensing with a complete self-packaging brings a new technique of sensing pressure which was found to be unique and not available in the literature. Complete analytical modelling of a

circular diaphragm with a T-shaped structure was also presented and the analytical results were compared with the numerical simulation results. Moreover, the differential output voltage from both the hall sensors can be related to the input applied pressure and compensates for any ambient temperature variations.

3.2 Sensor Design and Principle

The pressure sensor design comprises three parts as shown in Fig. 3.1. Part I is a cylindrical stainless steel (SS) tube fitting for applying input pressure and acts as a base structure for the sensor. Part II consists of a circular diaphragm of radius a, thickness t and a T-shaped rigid structure with a cylindrical base of radius b carrying two permanent magnets, fixed on the top surface of the circular diaphragm as shown in Fig. 3.1(b). Part III consists of an inverted L-shaped rigid structure with its inverted base resting on the SS tube fitting of part I. The top side of the SS tube fitting consists of a circular extension to fasten the circular diaphragm of part II and the bottom side is planned to fit a dead weight tester for applying input pressure. Two identical Hall sensors were attached one on the top side of the SS tube fitting and the other on the L-shaped rigid structure such that the two permanent magnets were in close proximity on either side of T-shaped rigid structure (part II) as shown in Fig. 3.1(b). The Hall sensors were exactly in line with the magnets and thus forming two pairs, with each pair consisting of a permanent magnet and a Hall sensor. For both the pairs an equal, fixed gap d is maintained between the Hall sensor and permanent magnet. Part I and part II shown in Fig. 3.1(a) to be integrated together to get a complete sensor.

Under no pressure load conditions, based on the initial arrangement the Hall sensors yield identical Hall voltages based on the magnetic field produced by the permanent magnets with an equal gap d. Since the sensor is a differential one, the difference between Hall voltages will be zero under initial conditions. When an input pressure is applied through the bottom side of the SS tube fitting (part I) to the circular diaphragm in part II, the diaphragm deforms, and this deformation is transmitted as an out-of-plane displacement to the two permanent magnets via the T-shaped rigid structure. This displacement results in an increase in the gap d of one pair and a decrease in the gap d in the other pair thereby producing a corresponding shift in the Hall voltage from the Hall sensors. The difference in the Hall voltages is taken as a measure of applied input pressure P.

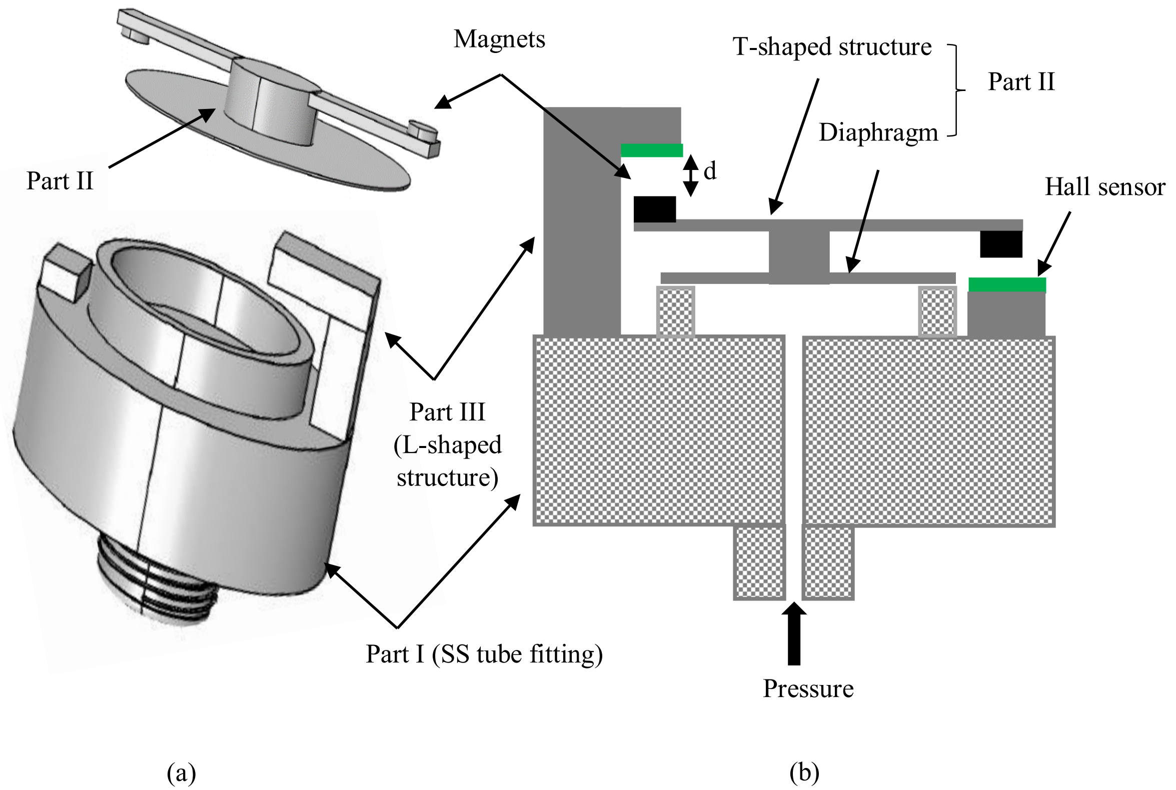

Fig. 3.1 Schematic of the pressure sensor structure (a) 3D view (b) side view

3.3 Analytical Modelling

Theoretical modelling of the sensor was carried out in two phases. In phase 1, the modelling of the part II alone was carried out to estimate the central deflection of the diaphragm and hence the displacement of the two permanent magnets with respect to the applied input pressure. In phase 2, analytical expressions for the Hall voltages developed by the two Hall sensors based on the diaphragm central deflection obtained from phase 1 were modelled.

3.3.1 Phase 1

The analytical model of the pressure sensor part II shown in Fig. 3.1 was developed by assuming the diaphragm as a circular diaphragm with T-shaped structure as circular boss structure. In modelling, the circular diaphragm is assumed as a thin plate with radius a, and the T-shaped rigid structure with cylindrical base representing a central circular boss structure of thickness h_1 and radius b were shown as a shaded region in Fig. 3.2.

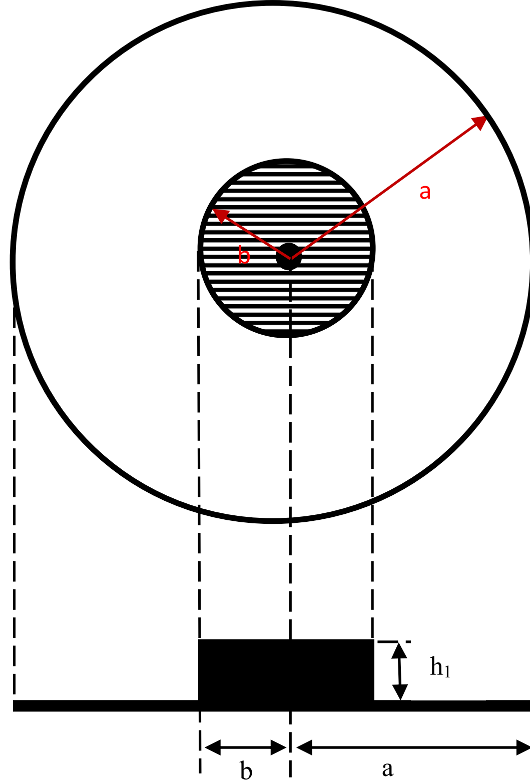

Fig. 3.2 Top view of the sensor diaphragm showing the central boss structure

Further, it is assumed that: (i) when no pressure is applied, the diaphragm remains flat and (ii) The outer circumference edge of the circular diaphragm is firmly clamped in all directions. A load-deflection analysis was carried out for the diaphragm by assuming a deflection function of the diaphragm given in Eq. (3.1) [89].

$$w(r) = A_o + B_o\rho^2 + C_o \log\rho + D_o\rho^2 \log\rho + \frac{Pa^4\rho^4}{64D} \tag{3.1}$$

where D is the flexural rigidity of the diaphragm, r is the radial axis of the diaphragm, P is the uniform applied pressure load on the diaphragm and ρ is the ratio *(r/a)*. The constants A_o, B_o, C_o and D_o can be determined by using the four boundary conditions given in Eq. (3.2).

$$\left.\begin{array}{c} \text{when } \rho = \frac{a}{a} = 1, \text{ at } r = a \\ w(r) = 0\,, \frac{dw}{d\rho} = 0 \\ \text{when } \rho = \frac{b}{a} = \beta\,, \text{ at } r = b \\ \frac{d^2w}{d\rho^2} + \frac{\nu}{\rho}\frac{dw}{d\rho} = 0\,, \frac{d}{d\rho}\left(\frac{d^2w}{dp^2} + \frac{1}{\rho}\frac{dw}{d\rho}\right) = L \end{array}\right\} \tag{3.2}$$

where a is the radius of the diaphragm, b is the radius of the circular boss structure and L is given in Eq. (3.3).

$$L = -P(2\pi b)\frac{a^3}{D} \tag{3.3}$$

By applying all the four boundary conditions specified in Eq. (3.2) to Eq. (3.1), The below four simultaneous equations were obtained given in Eq. (3.4).

$$\begin{gathered} A_o + B_o + \frac{Pa^4}{64D} = 0 \\ 2B_o + C_o + D_o + \frac{Pa^4}{16D} = 0 \\ 2B_o(\nu + 1) + \frac{C_0}{\beta^2}(\nu - 1) + D_0[2\log\beta(\nu + 1) + 3 + \nu] + \frac{Pa^4}{16D}\beta^2(3 + \nu) = 0 \\ \frac{4D_o}{\beta} + \frac{Pa^4\beta}{2D} = L \end{gathered} \tag{3.4}$$

where v is the poison's ratio of the diaphragm material. By solving all the four simultaneous equations specified in Eq. (3.4), the constants A_o, B_o, C_o and D_o thus obtained were given in Eq. (3.5).

$$\begin{gathered} D_o = -\frac{Pa^4}{8D} + L\beta \\ C_o = -\frac{Pa^4}{16D} * \frac{\beta^2}{\alpha + \beta^2}[4\beta^2\log\beta + \alpha\beta^2 + 1] - \frac{L\beta^3}{\alpha + \beta^2}[M] \\ B_o = \frac{Pa^4}{32D} * \frac{1}{\alpha + \beta^2}[4\beta^2(\log\beta + 1) + \alpha(\beta^4 + 2\beta^2 - 1)] + \frac{L\beta^3}{\alpha + \beta^2}[M] \\ A_o = -\frac{Pa^4}{64D} * \frac{1}{\alpha + \beta^2}[8\beta^2(\log\beta + 1) + \alpha(2\beta^4 + 4\beta^2 - 1) + \beta^2] - \frac{L\beta^3}{\alpha + \beta^2}[M] \\ M = [2\log\beta(\nu + 1) + 4 + 2\nu] \end{gathered} \tag{3.5}$$

where α is another constant given by $(1-v)/(1 + v)$. By replacing $\beta = b/a$, all the four constants A_o, B_o, C_o and D_o specified in Eq. (3.5) can be further simplified in terms of diaphragm parameters a, b, P and D. The resulting constants were then finally substituted in Eq. (3.1) to obtain the load-deflection function of the circular diaphragm with circular central boss as given in Eq. (3.6). Since the entire boss structure is rigid, the central deflection w_C of the circular bossed diaphragm will be equal to the deflection at the edge ($r = b$) of the circular boss structure given in Eq. (3.7).

$$w(r) = A_o + B_0 \frac{r^2}{a^2} + C_o \log\frac{r}{a} + D_0 \frac{r^2}{a^2} \log\frac{r}{a} + \frac{Pr^4}{64D} \tag{3.6}$$

$$w_c = w(r = b) = A_0 + B_o \frac{b^2}{a^2} + C_0 \log\frac{b}{a} + D_0 \frac{b^2}{a^2} \log\frac{b}{a} + \frac{Pb^4}{64D} \tag{3.7}$$

The central deflection w_c obtained will depend on the parameters *a, b, P* and *D*. The flexural rigidity *D* is in turn dependent on young's modulus *E* and thickness *t* of the diaphragm. From the analytical expression in Eq. (3.7), the radius *a*, thickness *t* of the diaphragm and radius *b* of the circular boss structure is optimized to ensure maximum central deflection for an applied pressure in the range of 0–20 bar using MATLAB as a mathematical tool. The results in Fig. 3.3 shows the variation in diaphragm central deflection w_c with the radius of the diaphragm for three different diaphragm thickness (0.1 mm, 0.2 mm and 0.3 mm) and three different radii of the central boss (2 mm, 3 mm and 4 mm) at an applied maximum pressure of 20 bar. It can be seen from the results tabulated in Table 3.1, the diaphragm radius of 15 mm, thickness of 0.1 mm and central boss radius of 4 mm, the diaphragm central deflection was found to be maximum. For further analysis, the variation in w_c was also obtained by applying pressure in steps of 1 bar for the entire pressure range of 0-20 bar.

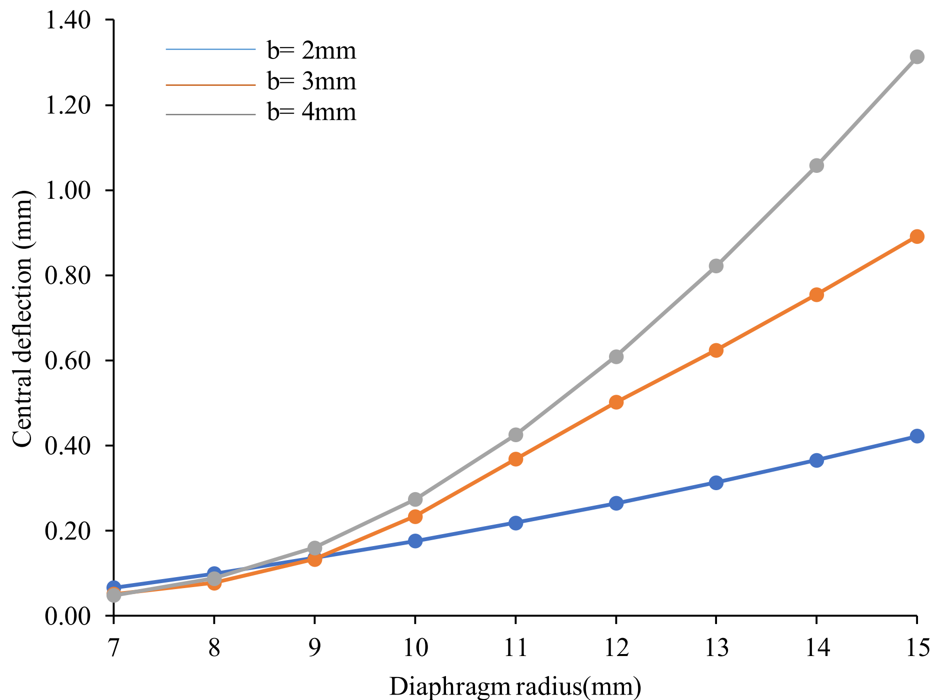

(a)

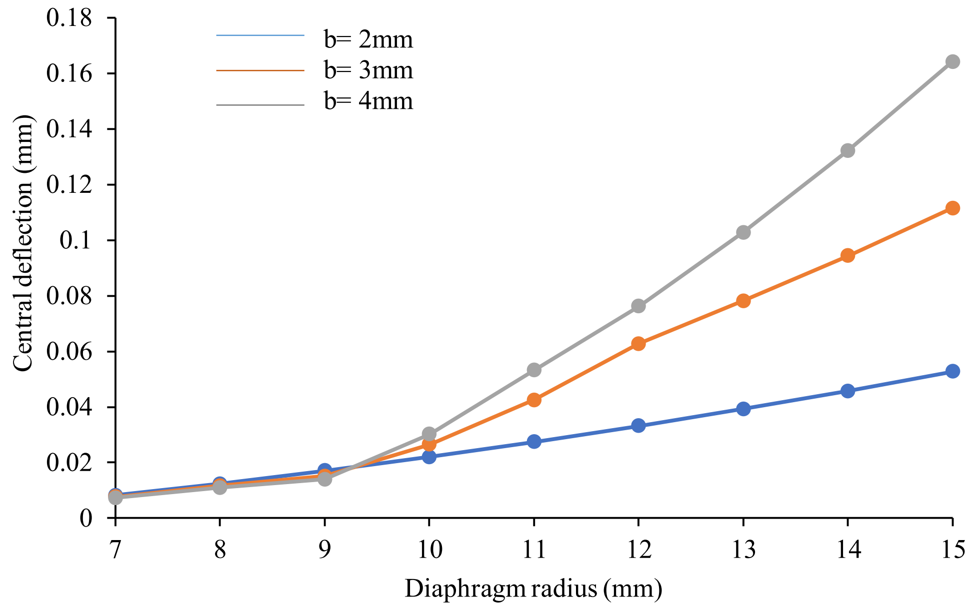

(b)

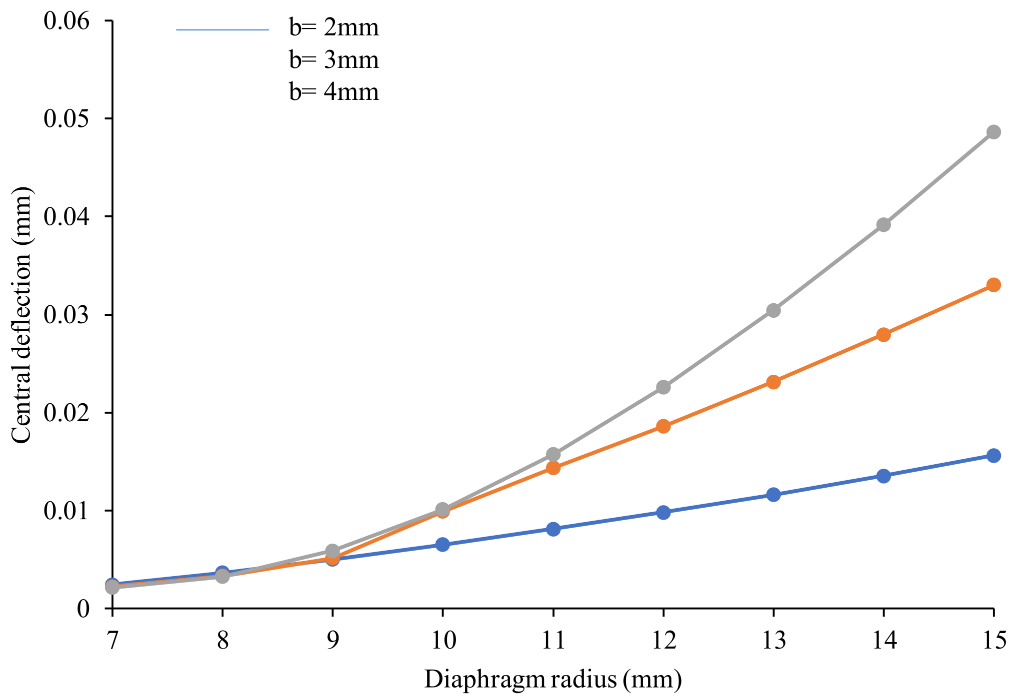

(c)

Fig. 3.3 Variation in diaphragm central deflection for three different diaphragm thickness (a) 0.1 mm (b) 0.2 mm and (c) 0.3 mm

Table 3.1 Optimum dimension of the sensor for maximum central deflection of the diaphragm

	Diaphragm thickness, t (0.1mm)			Diaphragm thickness, t (0.2 mm)			Diaphragm thickness, t (0.3 mm)		
	Boss radius, b (mm)			Boss radius, b (mm)			Boss radius, b (mm)		
Diaphragm radius, a (mm)	2	3	4	2	3	4	2	3	4
7	0.0661	0.0512	0.0479	0.008262	0.007645	0.007241	0.002448	0.002265	0.002145
8	0.0992	0.0773	0.0880	0.012396	0.011664	0.010995	0.003673	0.003345	0.003258
9	0.1361	0.1329	0.1599	0.017009	0.015107	0.013985	0.00504	0.005143	0.005922
10	0.1761	0.2341	0.2736	0.0220	0.0265	0.0302	0.0065	0.0099	0.0101
11	0.2191	0.3679	0.4252	0.0274	0.0425	0.0531	0.0081	0.0144	0.0157
12	0.2649	0.5020	0.6095	0.0331	0.0628	0.0762	0.0098	0.0186	0.0226
13	0.3138	0.6247	0.8217	0.0392	0.0781	0.1027	0.0116	0.0231	0.0304
14	0.3661	0.7548	1.0575	0.0458	0.0943	0.1322	0.0136	0.0280	0.0392
15	0.4222	0.8917	1.3135	0.0528	0.1115	0.1642	0.0156	0.0330	0.0486

3.3.2 Phase 2

Under no pressure load conditions, the (part II) diaphragm central deflection w_c is zero and hence the two permanent magnets are at equidistance d from the Hall sensors as shown in Fig. 3.4(a). By considering the permanent magnet as a cylindrical structure shown in Fig. 3.5, the magnetic flux density B_i due to the permanent magnet experienced by both the Hall sensors kept at a distance d is given by Eq. (3.8) [90]. The corresponding Hall voltages V_{h1} and V_{h2} thus developed were given in Eq. (3.9).

$$B_i = B_r\left(\frac{L+d}{\sqrt{R^2+(L+d)^2}} - \frac{d}{\sqrt{R^2+d^2}}\right) \tag{3.8}$$

$$V_{h1} = V_{h2} = K_h\frac{B_i I}{t_h} \tag{3.9}$$

where L is the length of the permanent magnet, R is the radius of the permanent magnet and B_r is the flux density of the permanent magnet, K_h is the Hall coefficient, I is the input current to the Hall sensor and t_h is the thickness of the Hall sensor. By assuming the two

permanent magnets and two Hall sensors are identical in all other parameters except magnetic flux density, the difference in the Hall voltage V_h will be zero under no pressure load conditions.

With the applied input pressure, the diaphragm deflects by a distance x as shown in Fig. 3.4(b). Now the magnetic flux density of the permanent magnet experienced by both the Hall sensors will be different and given by Eq. (3.10) and Eq. (3.11) as B_1 and B_2. The corresponding difference in Hall voltage V_h is given in Eq. (3.12).

$$B_1 = \frac{B_r}{2}\left(\frac{L+d-x}{\sqrt{R^2+(L+d-x)^2}} - \frac{d-x}{\sqrt{R^2+(d-x)^2}}\right) \tag{3.10}$$

$$B_2 = \frac{B_r}{2}\left(\frac{L+d+x}{\sqrt{R^2+(L+d+x)^2}} - \frac{d+x}{\sqrt{R^2+(d+x)^2}}\right) \tag{3.11}$$

$$V_h = \overline{V_{h1}} - \overline{V_{h2}} = k_h \frac{(B_1 - B_2)I}{t_h} \tag{3.12}$$

The resultant central deflection w_c of the diaphragm obtained from the analytical modelling in phase 1 was assumed to be distance x in this phase as shown in Fig. 3.4(b) to estimate the magnetic flux densities B_1 and B_2. The separation distance or gap d is fixed at 3 mm, length L is 3 mm, radius R is 2.5 mm and B_r is 1.43 T were used in the theoretical calculations of B_1 and B_2 respectively.

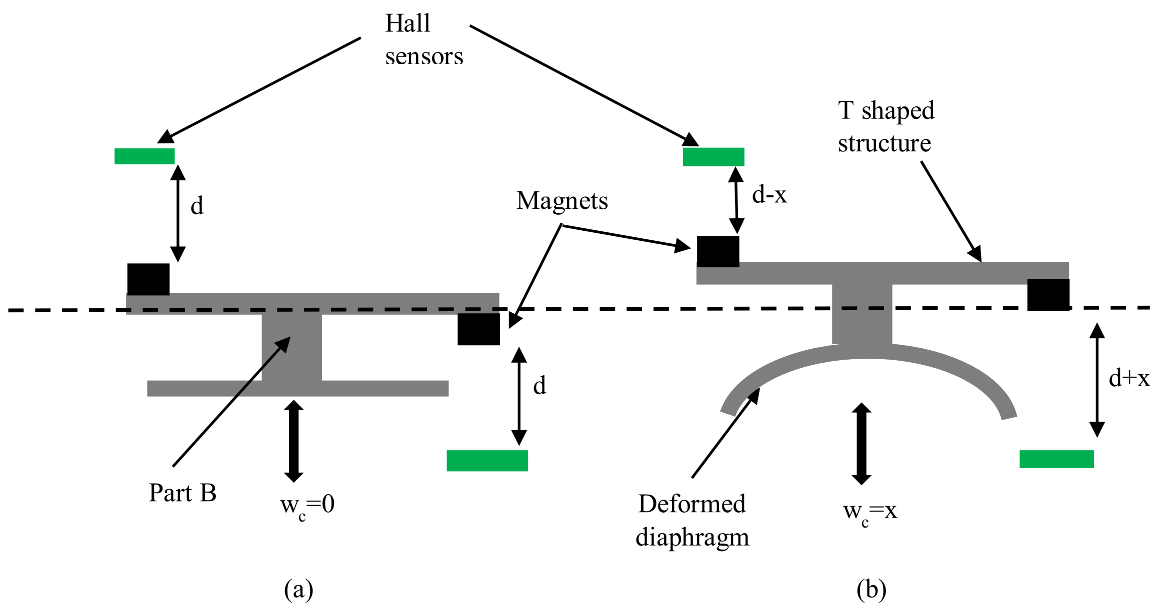

Fig. 3.4 Diaphragm deflection of the sensor (a) under no pressure load (b) with pressure

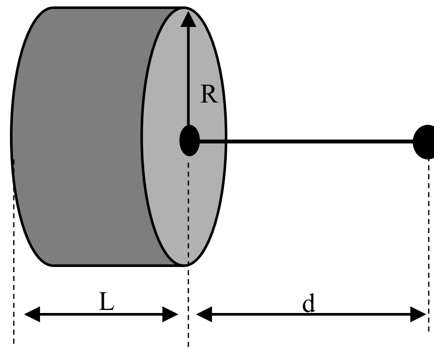

Fig. 3.5 Magnetic flux density at a certain distance from the permanent magnet

3.4 Numerical Modelling

The part II alone of the sensor design shown in Fig. 3.1 was modelled and simulated in the COMSOL Multiphysics FEM tool using the structural mechanics module to evaluate its performance in the operating pressure range of 0-20 bar. The initial dimensions of the sensor diaphragm were taken from the analytical model results and a 3D model of the sensor (part II) was built in the software with stainless steel material as shown in Fig. 3.6(a). The software uses the "Mesh" function to define the amount and size of the domain and boundary elements. During the simulation, a general tetrahedron parabolic meshing is applied to the 3D model to get a meshed model shown in Fig. 3.6(b) and the mesh size was optimized to get consistent results.

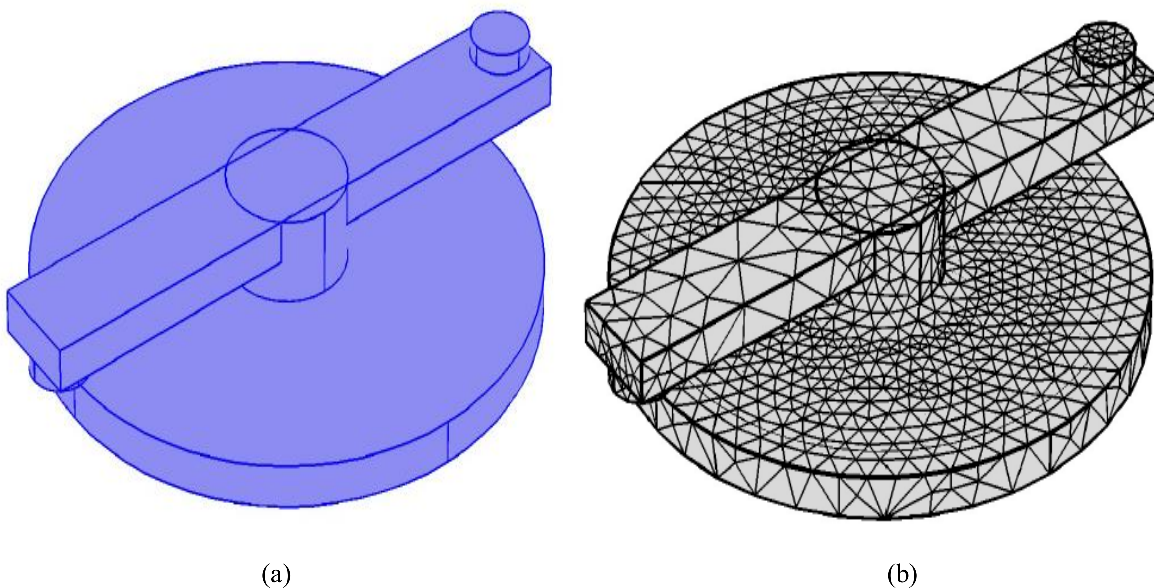

(a) (b)

Fig. 3.6 Pressure sensor part II built in COMSOL (a) 3D model (b) meshed model

As the working principle of the sensor depends on the deflection generated in the circular diaphragm, static structural analysis was carried out to obtain the maximum displacement for an applied pressure in the range of 0-20 bar. The simulation studies were also performed by varying the radius and thickness of the diaphragm and the radius of the central boss structure for maximum central deflection at the maximum pressure of 20 bar to verify the optimum dimensions obtained from analytical results. The results in Fig. 3.7 shows the central deflection of the diaphragm with a diaphragm radius of 15 mm, a circular boss radius of 4 mm for three different diaphragm thickness (0.1 mm, 0.2 mm and 0.3 mm). These results were found to be close agreement with the analytical modelling results obtained in Section 3.3.

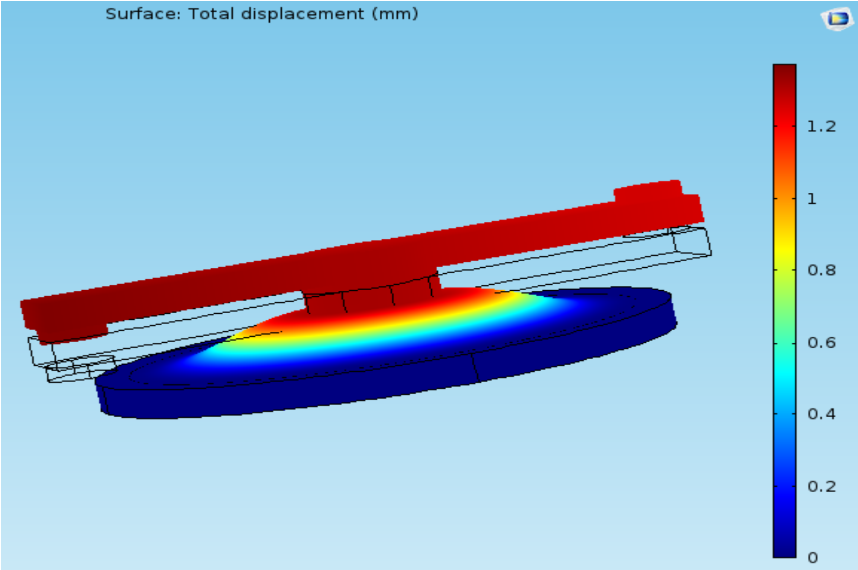

(a)

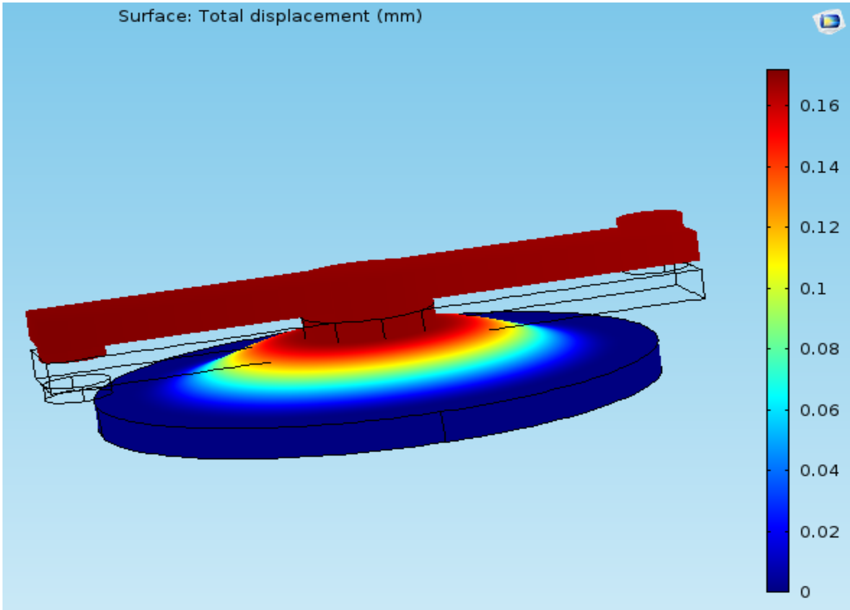

(b)

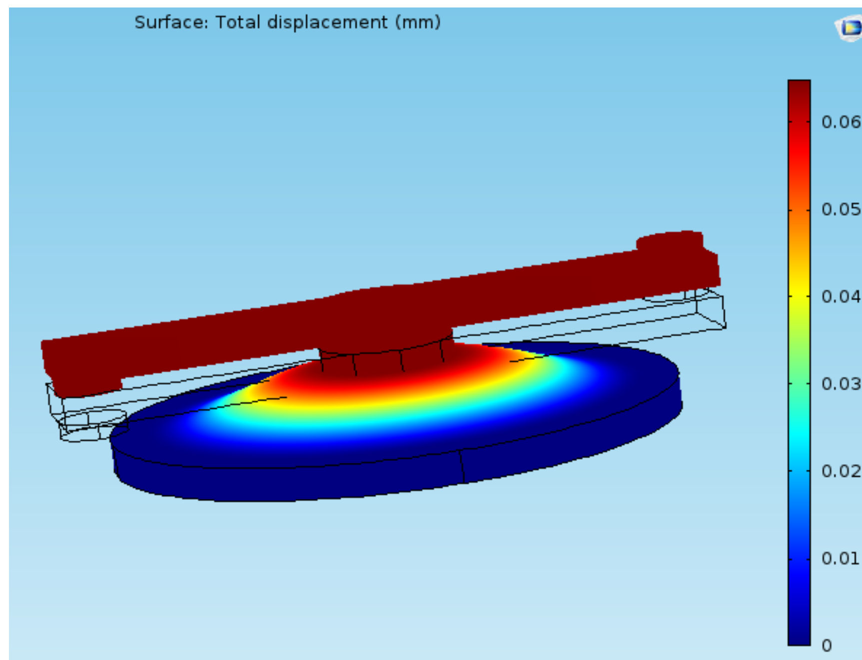

(c)

Fig. 3.7 Variation of diaphragm central deflection with three different diaphragm thickness (a) 0.1 mm (b) 0.2 mm and (c) 0.3 mm

A permanent cylindrical-shaped magnet was also modelled in the COMSOL tool whose dimensions and properties were taken from the data obtained in Section 3.3 as shown in Fig. 3.8(a) to show the variation in the magnetic flux density (B_1 or B_2) with the displacement of the magnet. The magnetic fields study is selected under the AC-DC module to study the distribution of magnetic flux density of the cylindrical magnet and its variation is shown in Fig. 3.8(b) after proper meshing. The resultant central deflection of the diaphragm for an applied pressure of 0-20 bar from the COMSOL simulations of the sensor part II is given as input displacement (positive, z-direction) to the permanent magnet. The corresponding magnetic flux density values at a distance of 3 mm from the top surface of the magnet along the z-direction were tabulated. Since the separation distance decreases with the displacement of the magnet, the corresponding magnetic flux density (B_1) experienced by the Hall sensor placed above the magnet will increase. On the other hand, if the input displacement is in negative z-direction, the separation distance increases with the displacement of the magnet, hence the magnetic flux density (B_2) experienced by the Hall sensor placed below the magnet will decrease.

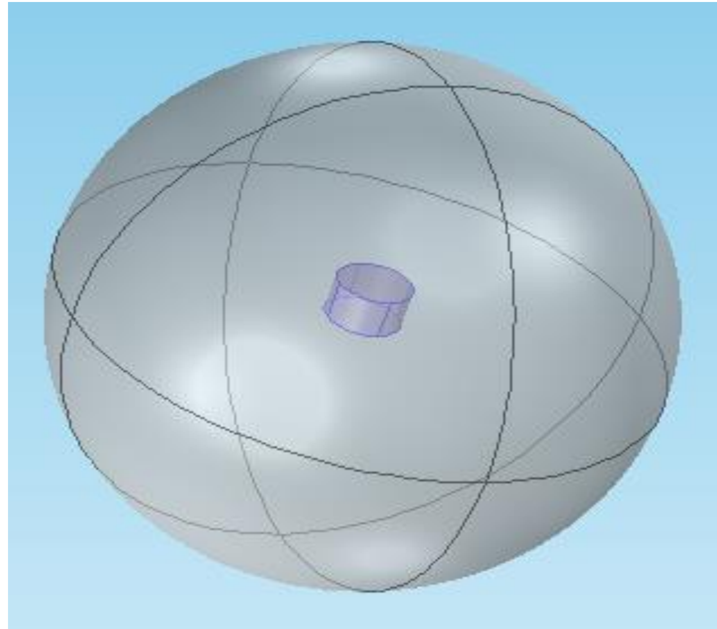

(a)

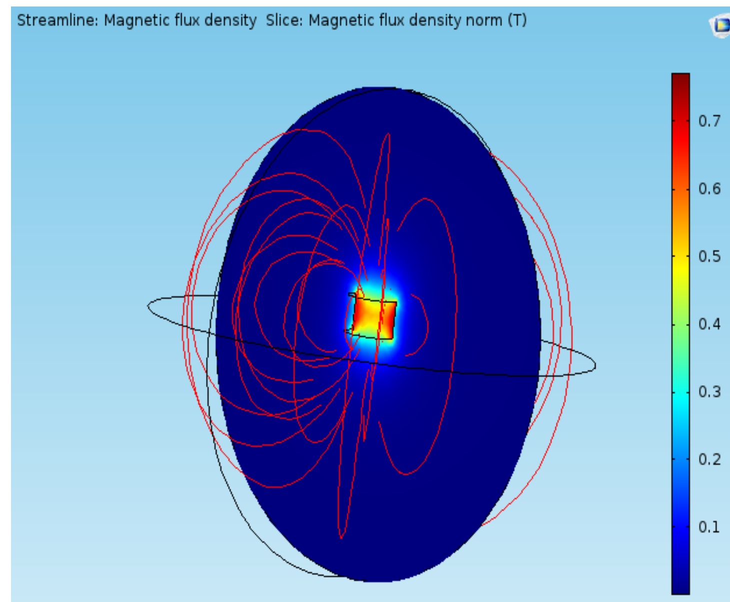

(b)

Fig. 3.8 (a) The 3D model of a cylindrical permanent magnet (b) Distribution of magnetic flux density around the magnet

3.5 Proposed Sensor Fabrication

Part II in the pressure sensor design is to be fabricated from cylindrical stainless steel (SS) disc of diameter 31 mm and 20 mm thick. The dimensions of the circular diaphragm and the boss structure were decided to be 15 mm, 0.1 mm and 4 mm based on the analytical modelling results and as well as from the numerical simulation results. A circular diaphragm can be realized by grooving 19.9 mm from the bottom side of SS disc (part II) using electrical discharge sparking process. The T-shaped rigid structure can be

realized in part II by using turning and wire cut EDM process as shown in Fig. 3.9(a). The pressure inlet tube or SS tube fitting (part I) and also the inverted L-shaped rigid structure (part III) to hold the Hall sensor as a single entity was also planned to be fabricated from another SS cylindrical disc of diameter 55 mm and 50 mm thick having M14 X 1.5 connector on one side and a small extension to fix the diaphragm (part II) on the other side through conventional machining process as shown in Fig. 3.9(b). The complete sensor to be integrated together by laser welding the SS tube fitting along with inverted L-shaped rigid structure (part I and part III) to the diaphragm (part II). Two iron boron neodymium permanent magnets and two Hall sensors are to be permanently attached by an epoxy adhesive and aligned exactly with each other separated by a gap of *d* as per the design of the sensor described in Section 3.2.

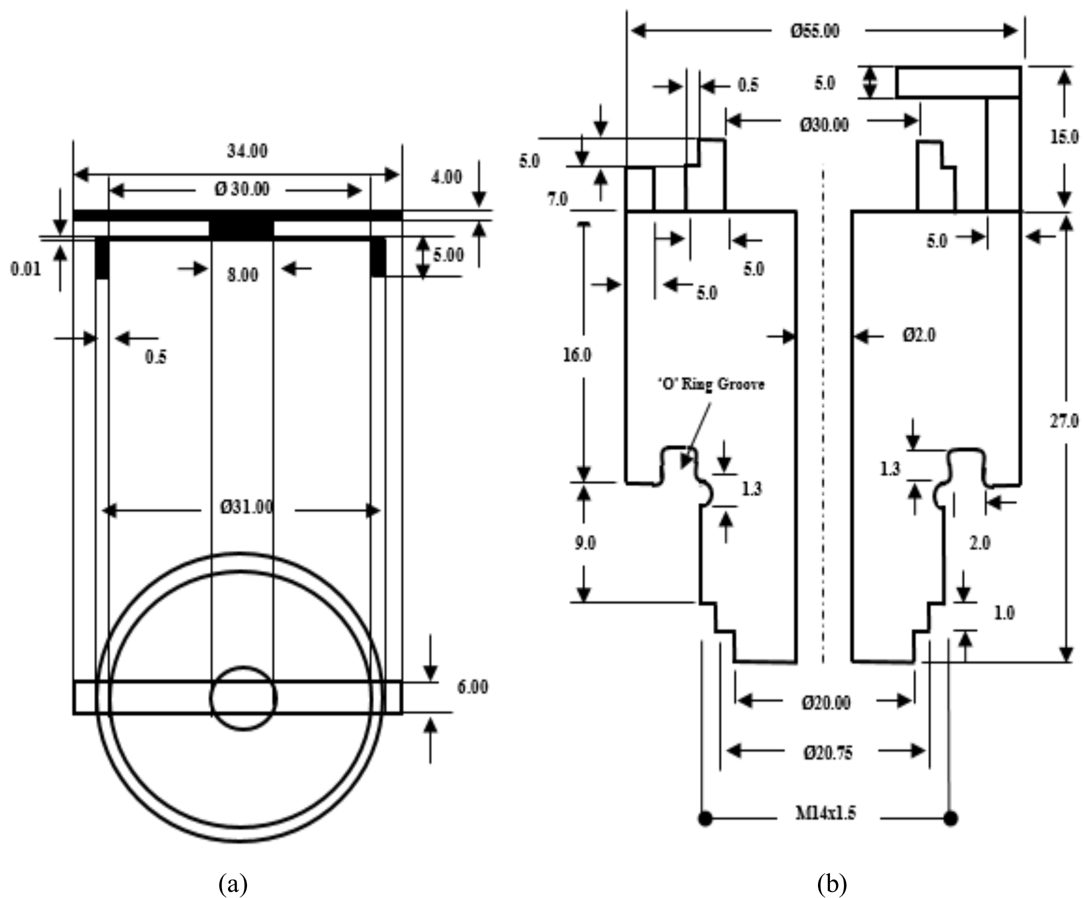

(a) (b)

Fig. 3.9 CAD drawing of the sensor (a) part II (b) part I and III

3.6 Results and Discussion

The diaphragm central deflection of the proposed sensor in the pressure range of 0-20 bar is estimated from Eq. (3.7) derived in Section 3.3 using MATLAB as a mathematical tool. A rigorous analysis was also performed analytically by varying the radius and

thickness of the diaphragm and also the radius of the circular boss structure at maximum input pressure to obtain the optimum dimensions for maximum central deflection. Both the analytical and numerical analysis resulted in the same optimum dimensions of the diaphragm and the rigid circular central boss structure. The diaphragm central deflection from analytical analysis and COMSOL simulation have been compared by varying input pressure in the range of 0-20 bar in steps of 1 bar as shown in Fig. 3.10. From the graph it is clear that the diaphragm central deflection increases linearly with the input pressure from the analytical modelling and numerical simulation. The central boss structure is generally used in the design to reduce the non-linearity in pressure deflection is characteristics of diaphragm based pressure sensors [77].

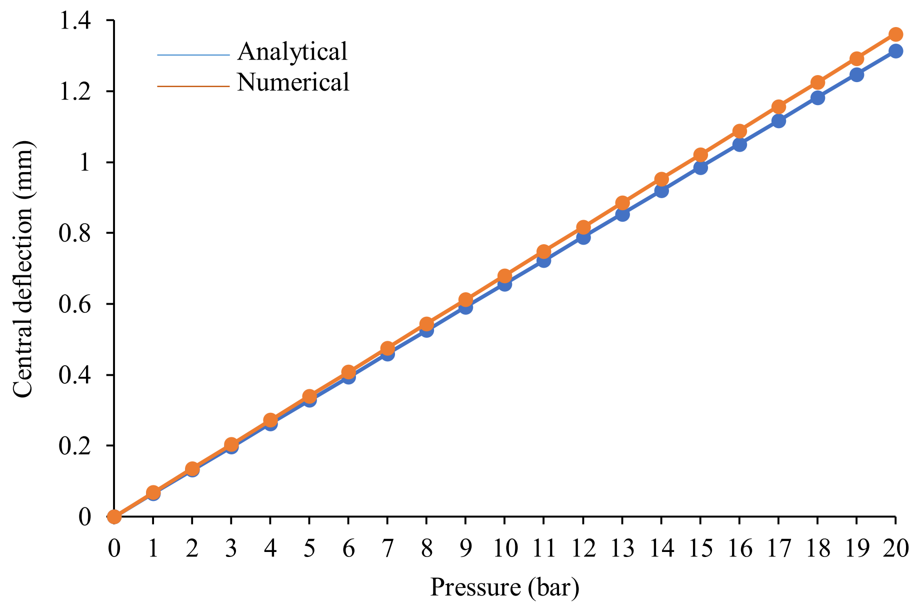

Fig. 3.10 Comparison of analytical and numerical results of diaphragm central deflection with input pressure

The variation in magnetic flux density (B_1) experienced by one of the Hall sensor with diaphragm central deflection of the proposed sensor for an input pressure range of 0-20 bar were estimated using Eq. (3.10) given in Section 3.3 using MATLAB as a mathematical tool. Similarly, the variation in magnetic flux density (B_1) with the diaphragm displacement was also obtained from COMSOL simulation carried out in Section 3.4 for the same input pressure range. The results in Fig. 3.11 show that the magnetic flux density (B_1) increases with input pressure for one pair, whose separation gap d decreases with diaphragm deflection. The analytical values so obtained are well supported by the numerical values.

A similar data can be obtained for the other sensing pair whose separation gap d increases with diaphragm deflection, where the magnetic flux density (B_2) decreases with input pressure. A suitable Hall sensor can be procured and included in the sensor design to match the obtained magnetic flux variations, in order to obtain a measurable Hall voltage.

Table 3.2 The variation in central deflection and magnetic flux density for 0-20 bar input pressure.

	Central deflection (mm)		Magnetic flux density (T)	
Pressure (bar)	Analytical	Numerical	Analytical	Numerical
0	0	0	0.1107	0.1115
1	0.0657	0.068	0.1147	0.1157
2	0.1313	0.1361	0.1188	0.1198
3	0.197	0.2041	0.1231	0.1248
4	0.2627	0.2722	0.1275	0.1295
5	0.3284	0.3402	0.1322	0.1335
6	0.394	0.4083	0.137	0.1385
7	0.4597	0.4763	0.1421	0.1431
8	0.5254	0.5444	0.1474	0.1484
9	0.5911	0.6125	0.1529	0.1538
10	0.6567	0.6805	0.1587	0.1599
11	0.7224	0.7486	0.1646	0.1673
12	0.7881	0.8164	0.1709	0.1735
13	0.8537	0.8847	0.1774	0.1794
14	0.9194	0.9527	0.1842	0.1868
15	0.9851	1.0208	0.1912	0.194
16	1.0508	1.0888	0.1986	0.1997
17	1.1164	1.1569	0.2062	0.21
18	1.1821	1.225	0.2141	0.2182
19	1.2478	1.293	0.2224	0.2281
20	1.3135	1.3611	0.231	0.237

Table 3.2 shows the variation in central deflection of the diaphragm and the magnetic flux density experienced by one of the Hall sensor with diaphragm central deflection of the proposed sensor for an input pressure range of 0-20 bar from both analytical and numerical

simulation results. The close match between the analytical and numerical results show that the analytical modelling attempted in this work on the circular diaphragm with central circular boss structure is validated through COMSOL simulation.

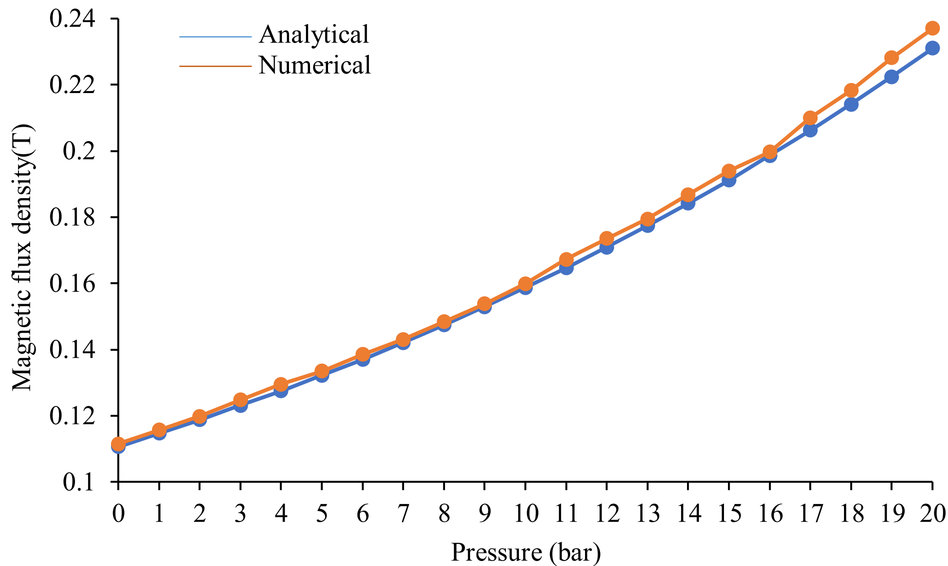

Fig. 3.11 Comparison of analytical and numerical results of magnetic flux density with input pressure

3.7 Conclusion

A pressure sensor utilizing the Hall sensor as a secondary sensor was designed and simulated to measure pressure in the range of 0-20 bar. A differential arrangement was proposed in the sensor design and a complete analytical model was also presented which is new to its kind and has not been attempted till now for any type of pressure sensor. Rigorous analytical studies were also carried out to optimize the dimensions of the sensor to obtain maximum central diaphragm deflection. An analytical expression was also derived to obtain the variation in the magnetic flux density on the Hall sensor for an applied pressure in the range of 0-20 bar. The analytical results were well supported by numerical simulation results in the same pressure range obtained from the COMSOL FEM simulation tool. Both the analytical modelling and the numerical simulation results were found to be in good agreement and resulted in the same optimum dimensions of the sensor. The sensor fabrication was also proposed with a detailed CAD drawing along with the dimensions using different grades of stainless steel materials. Moreover, the output from the proposed sensor is directly in the form of measurable differential Hall voltage that can be easily tracked by simple electronic circuitry and calibrated in terms of applied input pressure.

Chapter 4
Fabrication and Testing of a Hall Effect Based Pressure Sensor

4.1 Introduction

In recent years, a major focus has been vested towards the development of highly linear, sensitive pressure sensors for automotive, military, sports, robotic and biomedical applications. With the rapid evolution in the pressure sensing domain, a wide range of sensors have been developed to sense and monitor pressure. Among all, pressure sensing in conjunction with Hall effect is the least explored and very few works are reported. Hall effect is the production of a voltage difference across an electric conductor in the presence of an applied magnetic field perpendicular to the electric current. Hall sensors have been utilized in the development of various sensors to measure different physical quantities including pressure measurment. This chapter explores the fabrication and testing of Hall effect based pressure sensors with Hall sensors as a secondary sensing element or transducer.

In this chapter, two designs of Hall effect based pressure sensors are fabricated and tested. In design I, a differential setup with two pairs of Hall sensors and magnets are incorporated, and a single pair of Hall sensor and magnet is incorporated in design II. The differential arrangement is found to be a new and simple design as very few pressure sensors based on the Hall effect are available in the literature. Various static characteristics like non-linearity, hysteresis, and sensitivity are estimated and compared for both sensor designs.

4.2 Design I

The design I of the proposed pressure sensor is a differential arrangement as shown in Fig. 4.1 that is described in Chapter 3. A cylindrical round stainless steel (SS) tube adapter constitutes part A of the sensor. Part B consists of a circular diaphragm of radius a, thickness t and a T-shaped structure to carry two permanent magnets. Two identical Hall sensors are attached one on the top base of the SS tube adapter and the other one at the free edge of the inverted L-shaped structure. The permanent magnets are attached to the T-shaped structure such that they are in close proximity with the Hall sensors and are exactly in line with each other forming two pairs. Both the Hall sensor and magnet pairs are separated by a distance d as shown in Fig. 4.1. Part A and part B are to be integrated with each other to get the complete sensor.

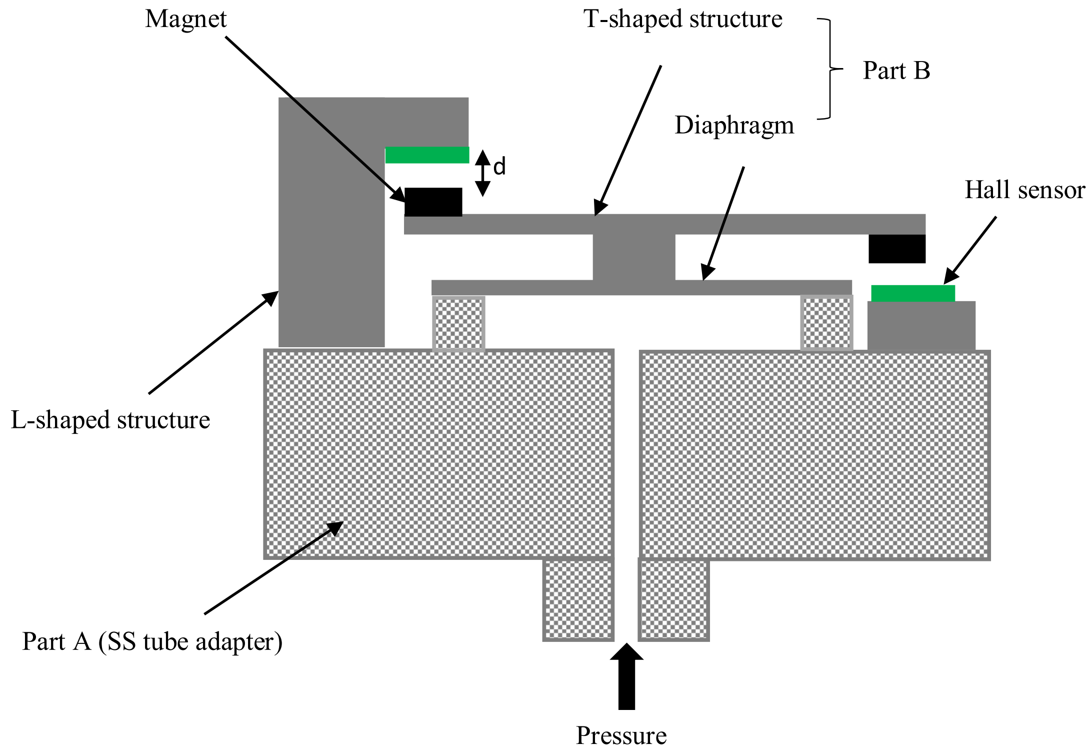

Fig. 4.1 Side view of the pressure sensor

Under no load condition, i.e., when no pressure is applied to the sensor, the diaphragm central deflection is zero as shown in Fig. 3.4(a). The magnetic field experienced by the Hall sensors due to the permanent magnets at the distance d will be the same and hence, both the Hall sensors will provide the same output voltage. Since the sensor design is a differential arrangement and if we select two identical Hall sensors, then the difference output from both the Hall sensor voltages will be zero under no load conditions. When a pressure P is applied, the diaphragm deforms by a distance x from its centre and the separation distance changes to $d+x$ and $d-x$ from the initial gap d as shown in Fig. 3.4(b). This results in a decrease and increase of output voltages from the Hall sensors respectively. The difference in the Hall output voltages is taken as a measure of the applied input pressure P.

4.3 Design II

The design II of the proposed pressure sensor is shown in the Fig. 4.2. Part A is a cylindrical round stainless steel (SS) tube adapter and has a rigid inverted L-shaped structure to hold a Hall sensor. Part B consists of a circular diaphragm of radius a, thickness t and a small protrusion as a single entity as shown in Fig. 4.2(a). A Hall sensor is attached

at the free edge of the inverted L-shaped structure. A permanent magnet is attached on the small protrusion such that it is in close proximity with the Hall sensor and are exactly in line with each other forming a pair. The Hall sensor and magnet pair are separated by a distance *d* as shown in Fig. 4.2. Part A and part B are to be integrated with each other to get the complete sensor

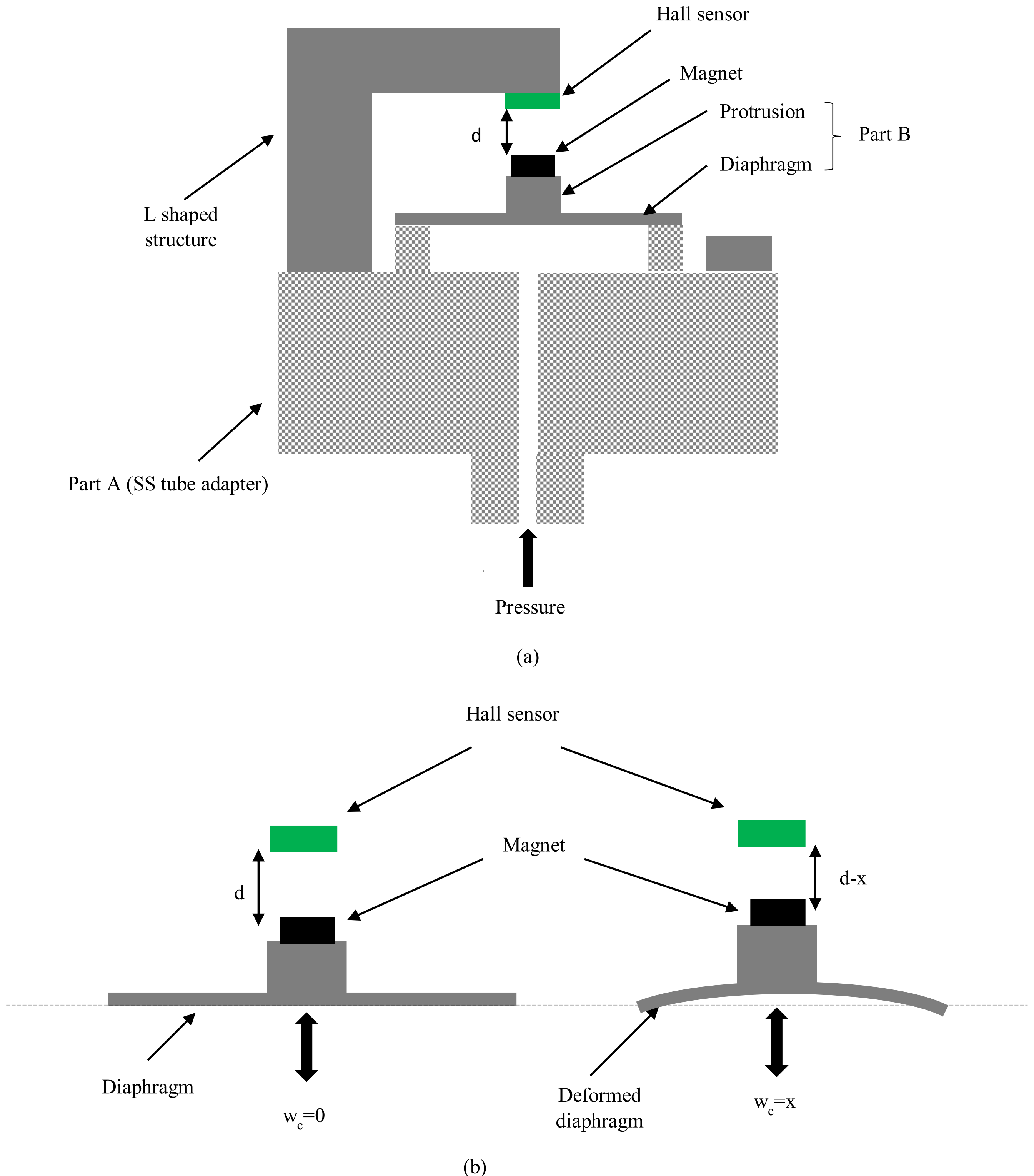

Fig. 4.2 (a) Side view of the pressure sensor (b) Diaphragm deflection

Under no load condition i.e., when no pressure is applied, the separation gap *d* is adjusted such that there is an output offset voltage from the Hall sensor. When an input pressure *P* is applied, the diaphragm deforms by a distance *x* and due to this deformation, the gap *d* decreases between the magnet and the Hall sensor as shown in Fig. 4.2(b). The decrease in the gap *d* will increase the magnetic flux experienced by the Hall sensor and thereby its output voltage increases from the offset value. The output Hall voltage from the Hall sensor is taken as a measure of the applied input pressure *P*.

4.4 Sensor Fabrication and Integration

In both the proposed sensor designs, the SS tube adapter (part A) is fabricated from a cylindrical solid stainless steel (SS 304) rod having diameter 40 mm and length 60 mm. The top side of the cylindrical rod is extended to fix the diaphragm and the other side a 3/8 BSP thread is made which functions as a pressure port. The detailed CAD drawing of the sensor's part A is shown in Fig. 4.3(a). The inner diameter of the diaphragm base is kept at 20 mm and the outer diameter is at 30 mm. The fabrication was carried out using CNC machining processes and the fabricated part A is shown in Fig. 4.3(b). The inverted L-shaped structures are fabricated separately and attached to the SS tube adapter for both the designs. A Hall sensor is to be attached at the free edge of the inverted L-shaped structure with an adhesive. The circular diaphragms which constitutes the part B of both the sensors are made of silicon elastomer rubber material with two different thicknesses 2 mm and 5 mm brought from Ami polymers Pvt Ltd, Dadra and Nagar Haveli.

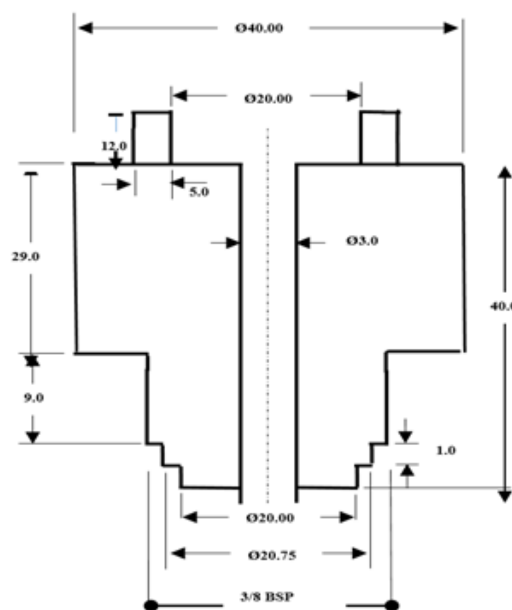

(a)

(b)

Fig. 4.3 (a) CAD drawing of the SS tube adapter (b) Fabricated SS tube adapter

In design I, a rectangular acrylic sheet of length 40 mm and width 10 mm is fastened on the top of the protrusion to get the T-shaped structure. The T-shaped structure is also bonded to the diaphragm with an adhesive to develop part B. On the two free edges of the T-shaped structure, two iron boron neodymium cylindrical magnets are attached, one on the top face and the other on the bottom face with an adhesive. Two Hall sensors are also attached as per the design I described in the Section 4.2. Finally, the part B is integrated with an epoxy adhesive (Gorilla super glue gel) to SS tube adapter (part A) to get the complete sensor as shown in Fig. 4.4.

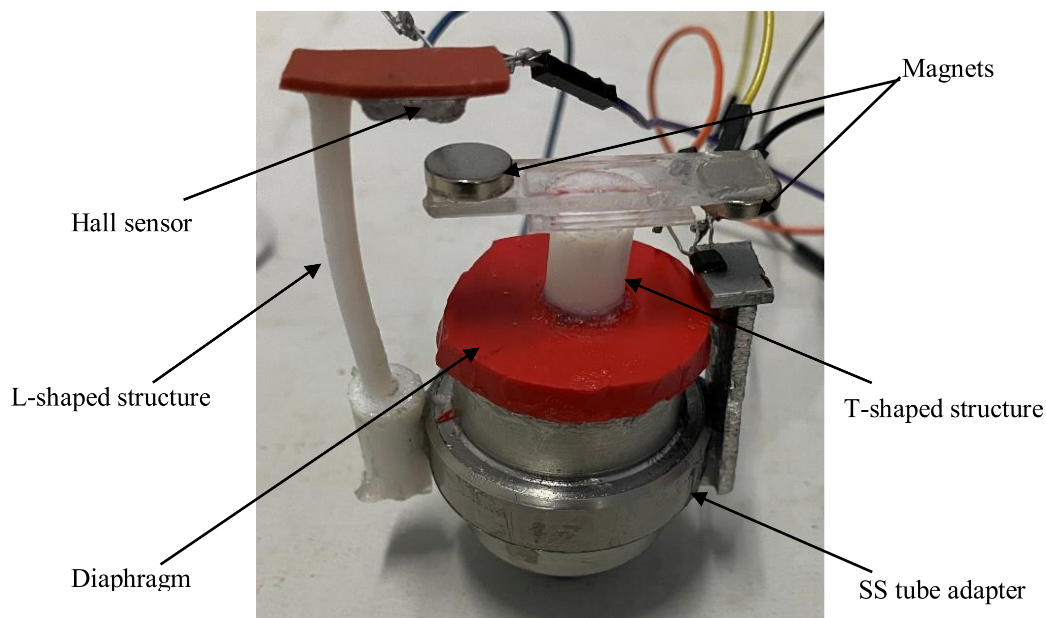

Fig. 4.4 Fabricated pressure sensor (design I)

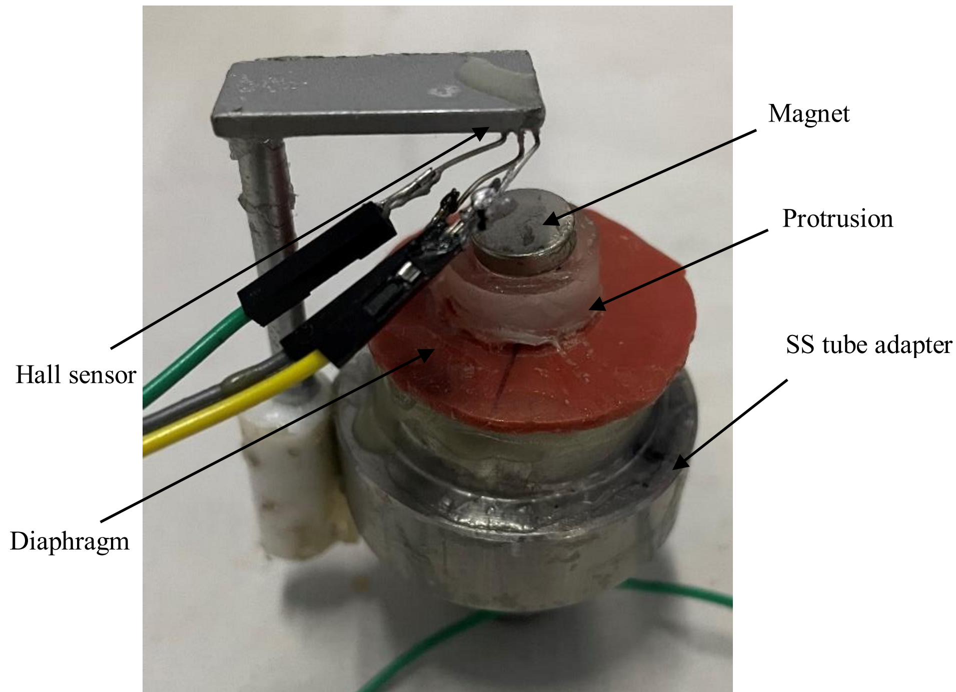

Fig. 4.5 Fabricated pressure sensor (design II)

The protrusion specified in design II is a cylindrical acrylic rod of 15 mm diameter and 5 mm height which is bonded to the diaphragm at its centre with an adhesive to develop part B as a single entity. An iron boron neodymium cylindrical magnet and a Hall sensor are attached with an adhesive as per the design II described in the Section 4.3. Finally, part A and part B are integrated to get the complete sensor as shown in Fig. 4.5.

4.5 Experimentation

To fix the value of *d* i.e., the separation gap between the magnets and Hall sensors under no load conditions, an experimental set up is made to obtain the displacement-voltage characteristics for the Hall sensor (Honeywell SS495A) as shown in Fig. 4.6. The specifications of the procured Hall sensor are given in Table 4.1. The Hall sensor is held firmly on to a fixed rod and a magnet of diameter 10 mm and length 5mm which is attached to the tip of a screw gauge to provide a known displacement. The Hall sensor and the magnet are properly clamped so that they are in close proximity with each other. The Hall voltage is obtained by varying the distance between them as shown in Fig. 4.7. The graph shows a linear range when the distance between Hall sensor and magnet is in between 5 mm to 11 mm. Hence in order to utilize the linear range of the Hall sensor the initial separation gap *d* under no pressure load is kept at 3 mm for the design I and 8 mm for design II.

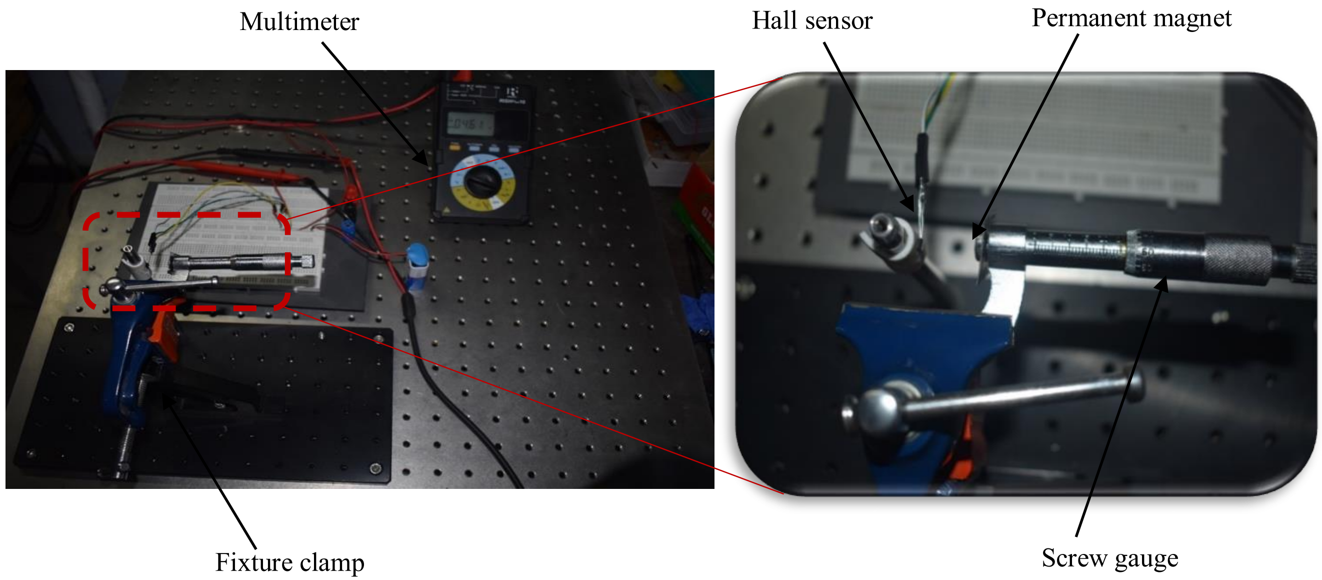

Fig. 4.6 Experimental setup for displacement-voltage characteristics of the Hall sensor

Table 4.1 Specifications of Hall Sensor (SS 495A)

Characteristic	Range
Supply voltage	4.5 to 10.5V
Output voltage	$V_{cc}/2$ - V_{cc}
Supply current	8.7 mA
Operating temperature	-40 °C - 150 °C
B Limits of operation	-600 to +600 Gauss
Sensitivity at 25°C	3 to 3.25 mV/Gauss

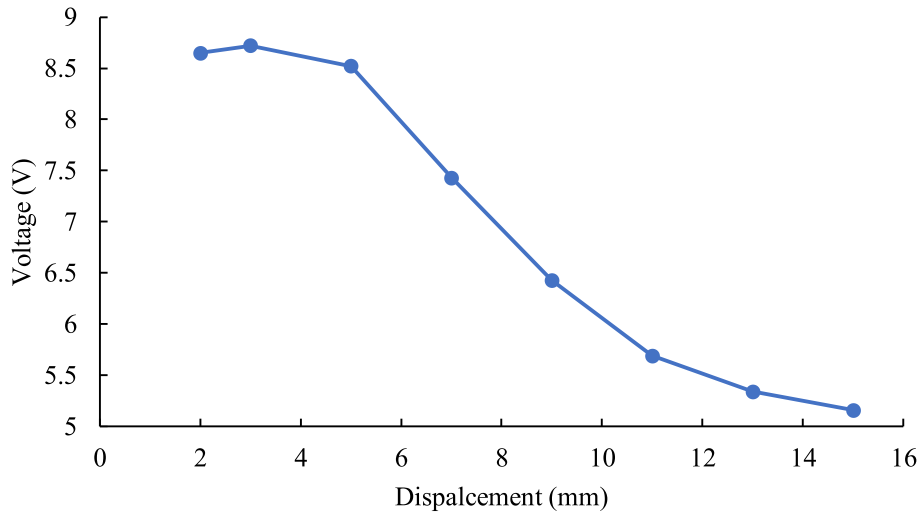

Fig. 4.7 Displacement-voltage characteristics of Hall sensor

After fixing the separation gap *d*, the testing of the fabricated sensors is done using a dead weight tester (M/S Yantrika instruments with a range of 0-100 bar). The experimental setup for testing the pressure sensor design I is shown in Fig. 4.8. Before the start of the calibration

process, priming operation of the dead weight tester was carried out at the zero-gauge pressure and the initial output voltage of Hall sensor at zero-gauge pressure was adjusted to zero. The sensor is mounted and fitted on the pressure port of the dead weight tester using the 3/8 BSP adapter. The pressure is applied to the sensor in steps of 0.1 bar by placing appropriate weights at the low pressure side of the dead weight tester and the differential voltage from the two Hall sensors is measured using a digital multimeter (Fluke 179). The output voltage of the sensor is also measured for descending pressure in steps of 0.1 bar. The calibration readings of the pressure sensor are taken for 25 cycles of ascending and descending pressure in the range of 0-1 bar to check its repeatability and hysteresis. A similar experimental set up was made for the pressure sensor design II and also tested for 25 cycles of ascending and descending pressure.

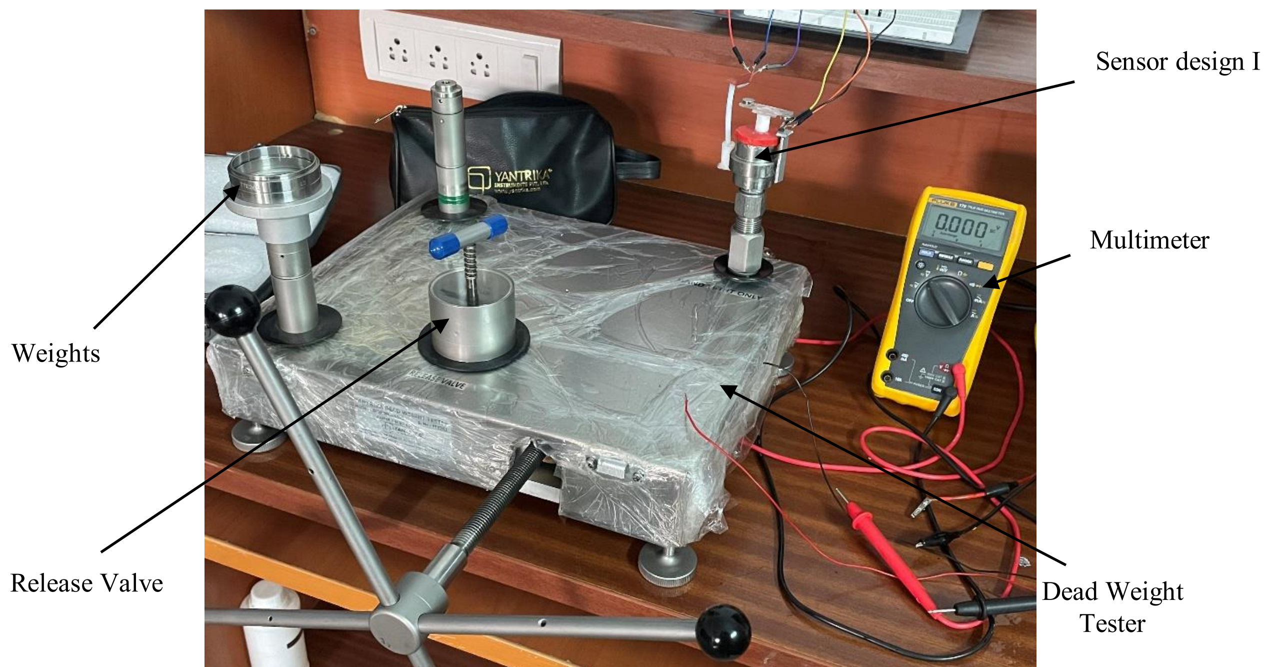

Fig. 4.8 Experimental setup for calibrating the pressure sensor

4.6 Results and Discussions

The calibration data for both design I and design II are obtained after repeating the experimental procedure for 25 cycles of ascending and descending pressure. The input-output characteristics for both the sensors by varying the input pressure from 0 -1 bar in steps of 0.1 bar for five sets of ascending and descending pressure is shown in Fig. 4.9. From the graph, the design I shows a high repeatability when compared to design II. The best fit lines from complete set of data for both sensor designs are plotted and the respective best fit line equations are given in Eq. (4.1)

$$V = 0.03P + 0.007 \text{ (design I)}$$
$$V = 0.2435P + 5.0249 \text{ (design II)} \quad (4.1)$$

where V is the output voltage and P is the input pressure. The % nonlinearity in both the designs are calculated from the best fit line values in Eq. (4.1) and substituting in Eq. (4.2). The corresponding nonlinearity curves are plotted for both the designs as shown in Fig. 4.10. The maximum % non-linearity for design I is found to be 0.2 % and for design II is found to be 3.75 %.

$$\% \text{ Nonlinearity} = \frac{Best\ fit\ value - Measured\ average\ value}{(Best\ fit\ value)max - (Best\ fit\ value)min} X100 \quad (4.2)$$

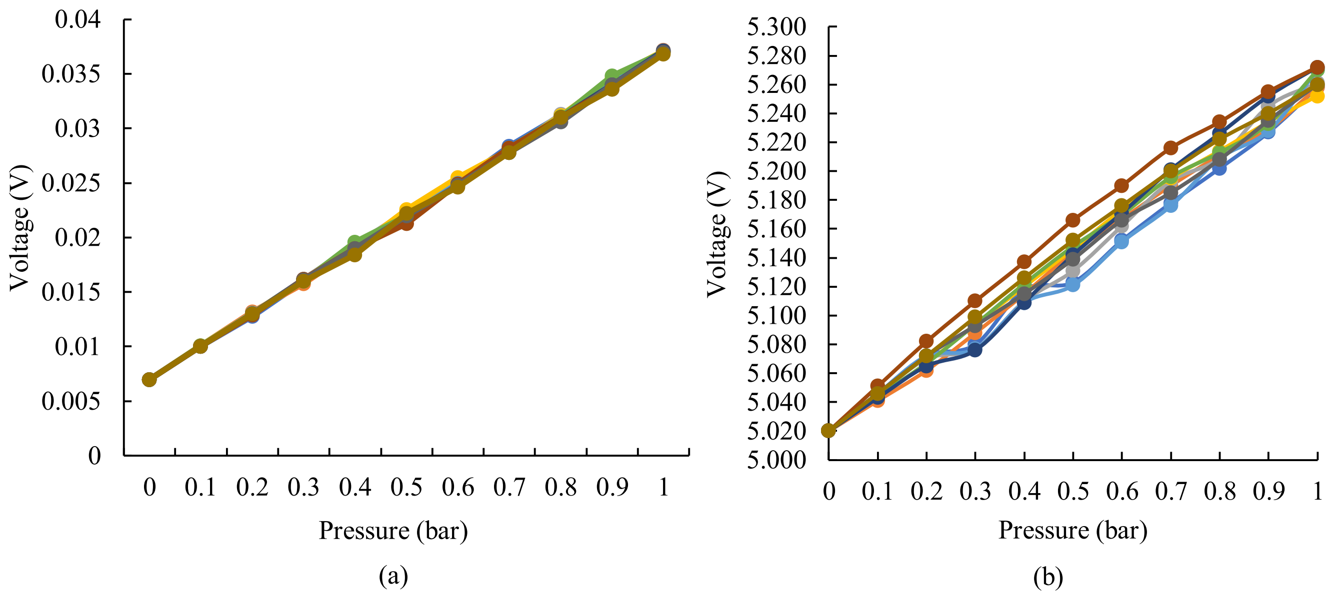

Fig. 4.9 Input-output characteristics of the pressure sensor (a) design I (b) design II

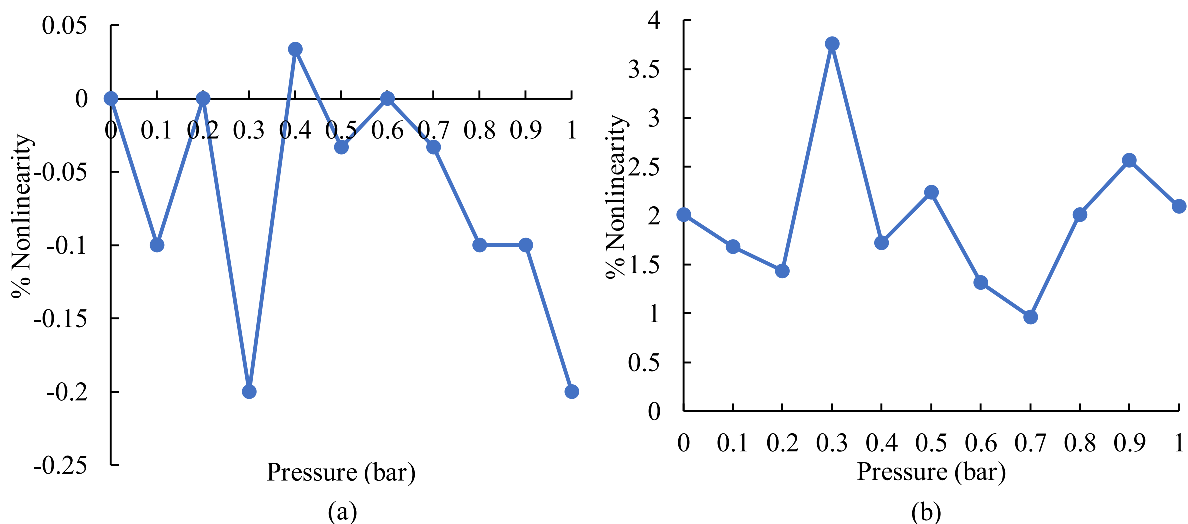

Fig. 4.10 % Nonlinearity of the pressure sensor (a) design I (b) design II

To estimate the hysteresis in both the pressure sensor designs, the average output voltage for complete set of ascending and descending pressure are estimated and plotted in

Fig. 4.11. The hysteresis is calculated by taking the deviation between average output voltage at ascending and descending pressure in terms of full scale deflection output voltage and plotted as shown in Fig. 4.12. From the graph, the maximum hysteresis for design I is found to be 0.21% and for design II is 0.37%.

$$\%\ \text{hysteresis} = \frac{avg.loading\ output\ value - avg.unloading\ output\ value}{avg.loading\ output\ value} * 100 \tag{4.3}$$

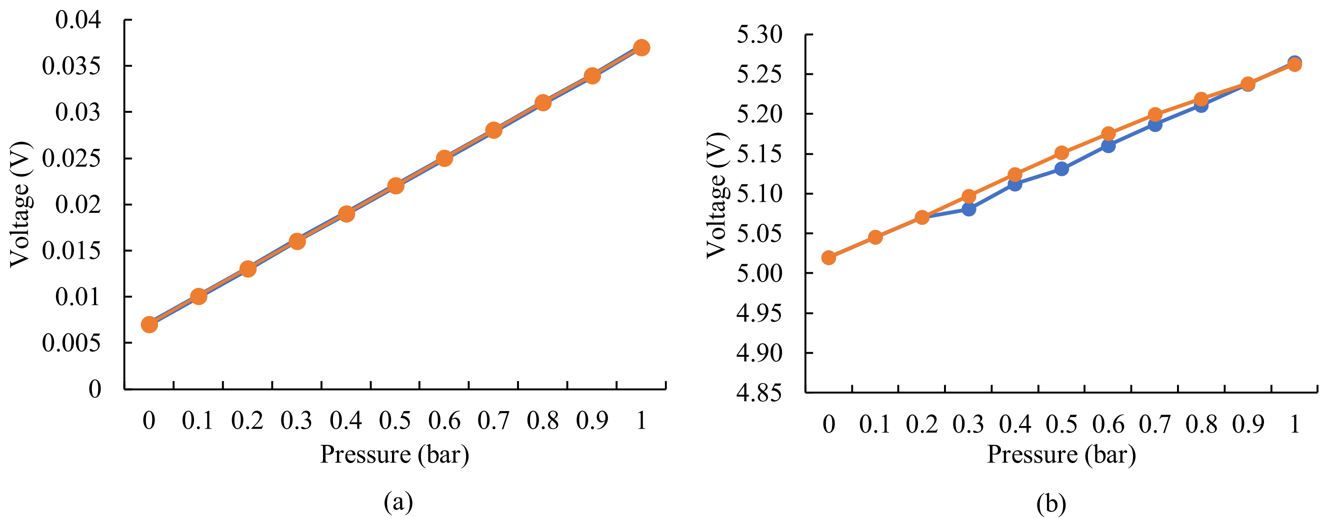

Fig. 4.11 Average output voltage of the pressure sensor (a) design I (b) design II

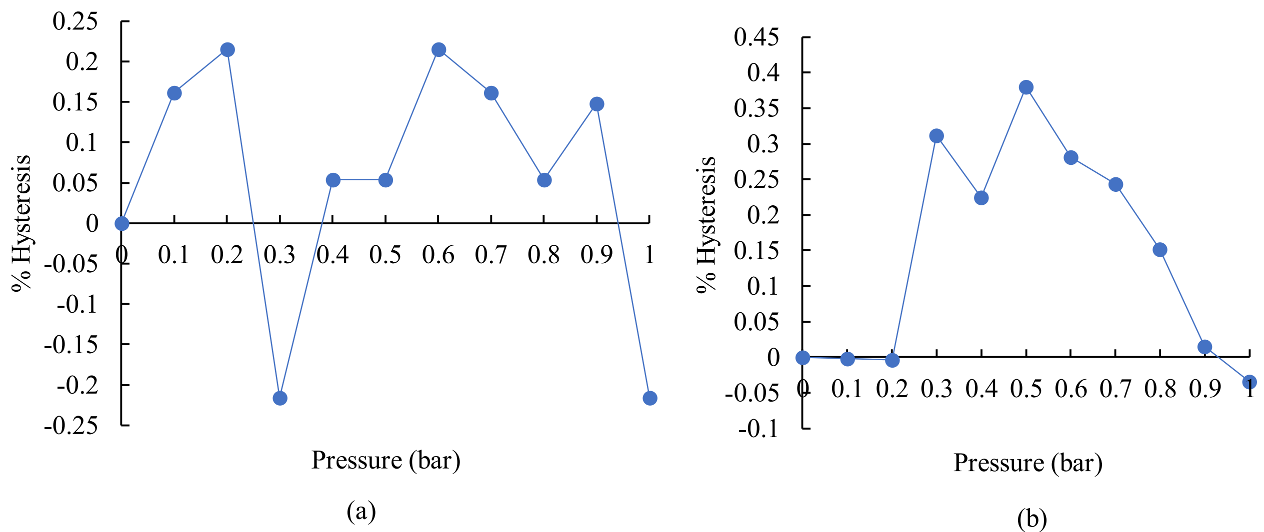

Fig. 4.12 % Hysteresis of the pressure sensor (a) design I (b) design II

By taking the best fit values once again for both the designs from Eq. (4.1), the pressure is calculated back from the average output voltage from the data and the estimated pressure is plotted against input pressure as shown in Fig. 4.13. From the estimated pressure, the percentage error is also calculated in terms of full scale deflection and plotted as shown in Fig. 4.14. The maximum % error for design I is found to be +1.21% and for design II is

-4.08 %. The repeatability for both sensor designs is calculated by the equation $2\sqrt{2}S$ where S is the standard deviation. The maximum repeatability for design I is 0.0008 and for design II is 0.51 as shown in Fig. 4.15. According to industry standards, repeatability should be less than 5 [63]. Hence both the designs show good repeatability. The resolution of both sensor designs is found to be 0.02 bar as shown in Fig. 4.16.

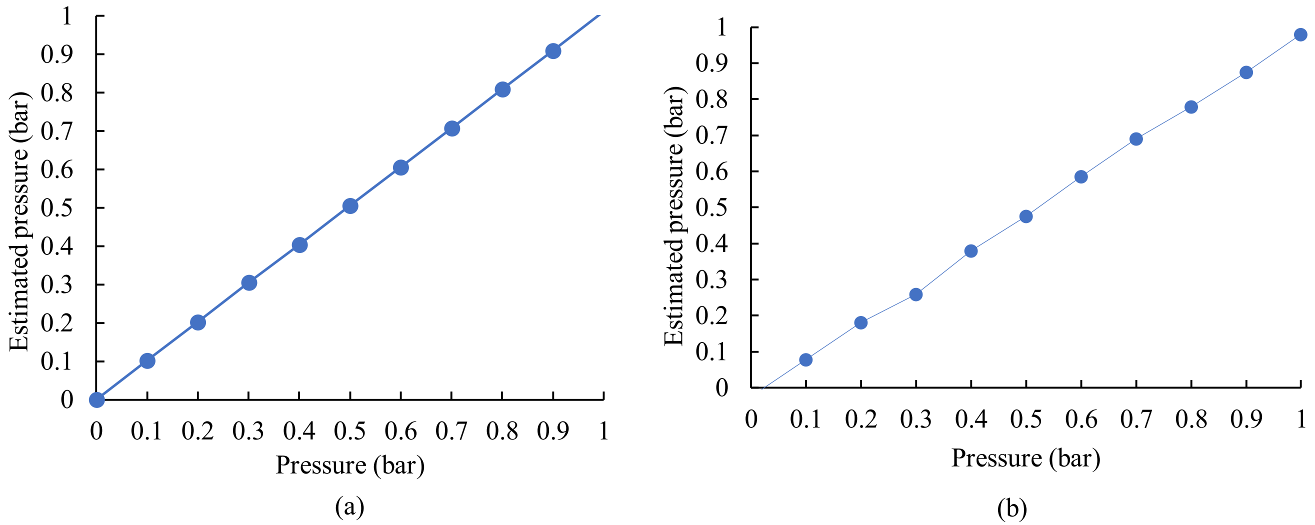

Fig. 4.13 Estimated pressure of the pressure sensor (a) design I (b) design II

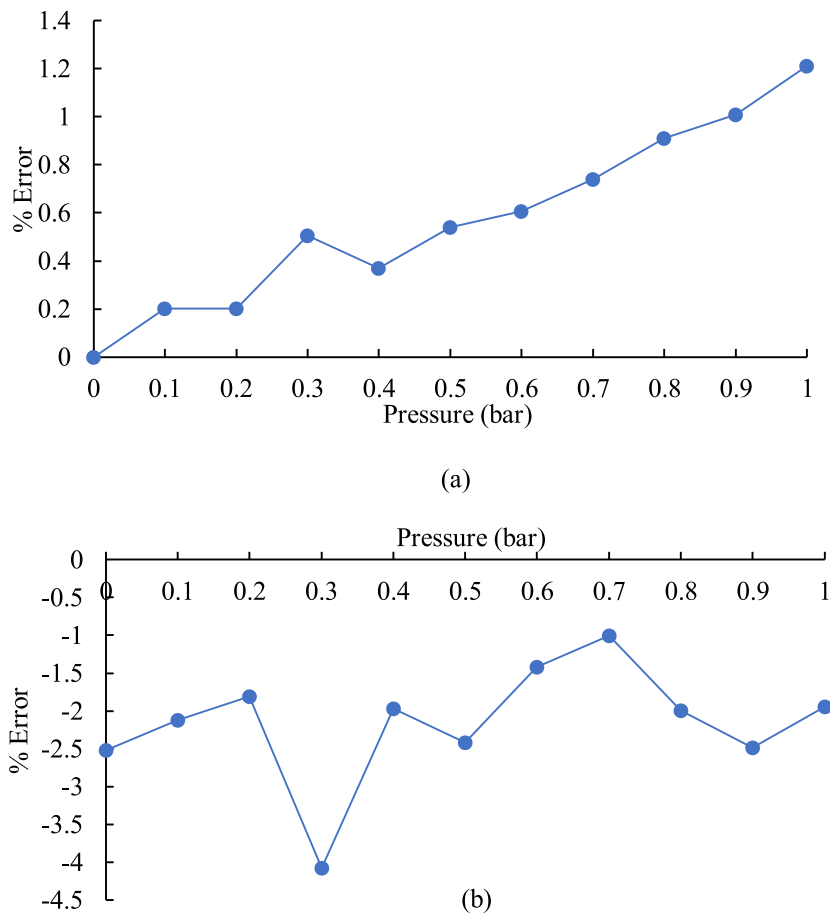

Fig. 4.14 % Error of the pressure sensor (a) design I (b) design II

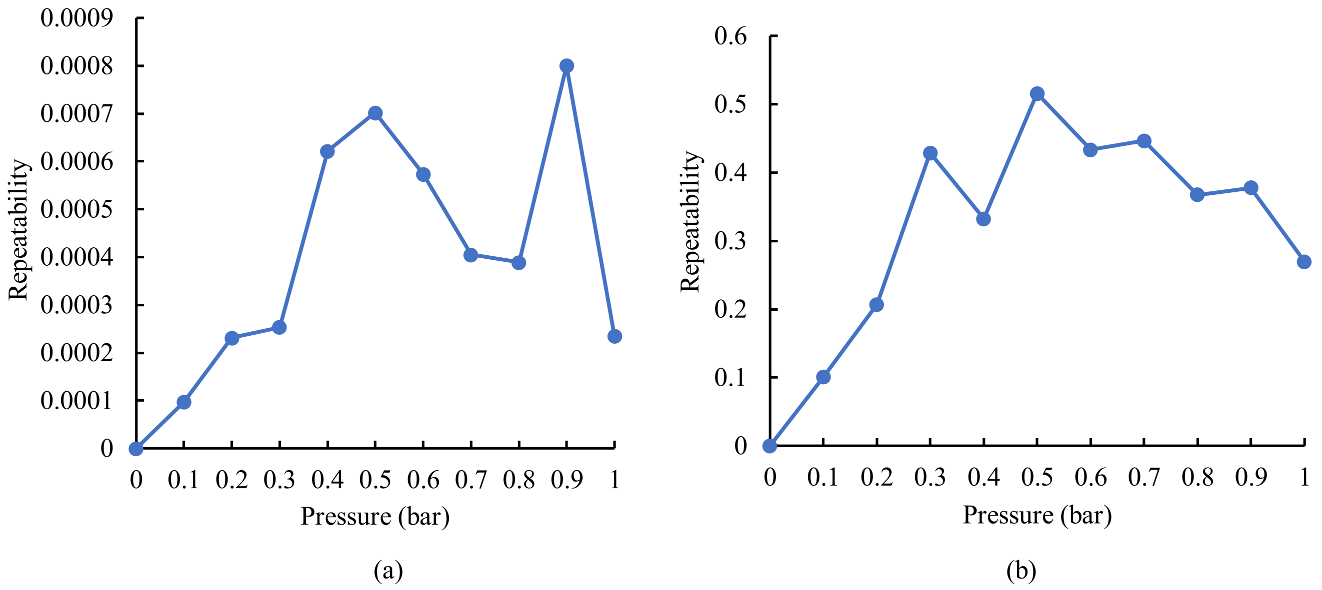

Fig. 4.15 Repeatability of the pressure sensor (a) design I (b) design II

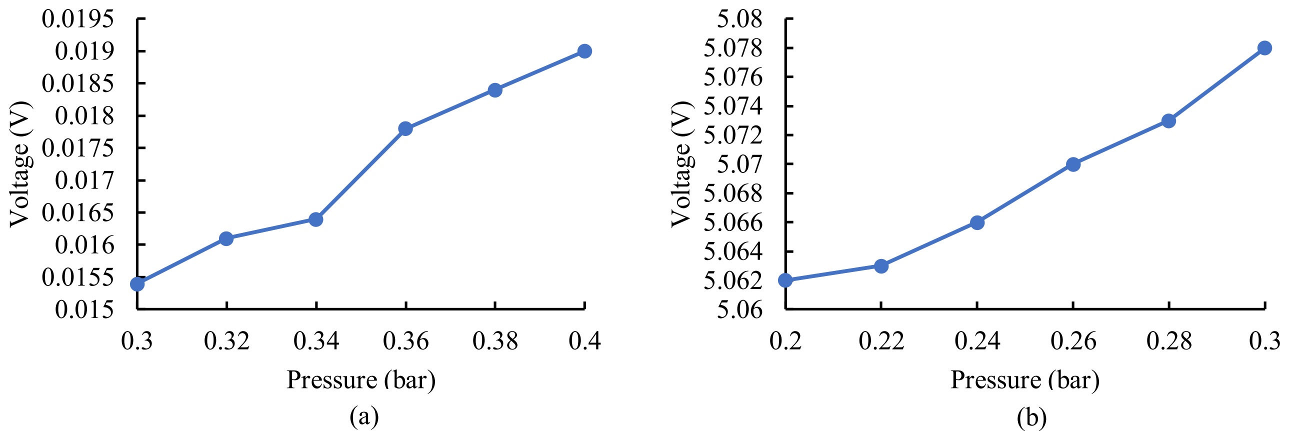

Fig. 4.16 Resolution of the pressure sensor (a) design I (b) design II

The sensitivity for both the pressure sensor designs are also calculated by using the Eq. (4.3).

$$S = \frac{Vo(Pm) - Vo(Po)}{Pm - Po} \tag{4.4}$$

Where Pm is the maximum pressure or full scale pressure and Po is the minimum input pressure and $Vo(Pm)$ is the average output voltage for full scale reading and $Vo(Po)$ is the average output voltage for minimum input pressure. The sensitivity for the design I is found to be 0.03 mV/mbar and for design II is 0.243 mV/mbar.

A comparison of static characteristics of design I and design II is given in Table 4.2. From the comparison, it can be seen that design I shows better characteristics than design II. A

comparison of the proposed pressure sensor with similar pressure sensors available in the literature is also specified in Table 4.3.

Table 4.2 Comparison of static characteristics of fabricated sensors

Characteristic	Design I	Design II
Non-linearity (%)	0.2	3.75
Hysteresis (%)	0.21	0.37
% Error	+1.21	-4.08
Sensitivity (mV/mbar)	0.03	0.243
Resolution	0.02 bar	0.02 bar
Repeatability	0.0008	0.51

Table 4.3 Comparison of proposed sensor designs with other pressure sensors

Characteristic	Design I	Design II	Ref. [63]	Ref. [64]	Ref. [68]
Non-linearity (%)	0.2	3.75	1.6	1	1.5
Hysteresis (%)	0.21	0.37	----	----	----
% Error	+1.21	-4.08	----	1	----
Sensitivity	0.03 mV/mbar	0.243 mV/mbar	0.36 mv/mbar	----	0.167 mV/mbar
Range	0-1 bar	0-1 bar`	0-40 psi (0-2.75 bar)	0-12 bar	0-300 Pa (0-0.003 bar)

The calibration of the fabricated sensors is performed only for static pressures and is not tested for dynamic pressures. The fabricated sensors can also be used to measure dynamic pressure in the pressure range of 0-1 bar by analyzing the mode frequencies of the diaphragms and their complete structures. An Eigen frequency analysis is carried out in the COMSOL tool to find out the mode frequencies of the proposed pressure sensor designs. The three vibrations modes and the five vibration mode frequencies (Eigen frequencies) of the diaphragm alone and the T-shaped structure with diaphragm are shown in Fig. 4.17, Fig. 4.18 and in Table 4.4 respectively.

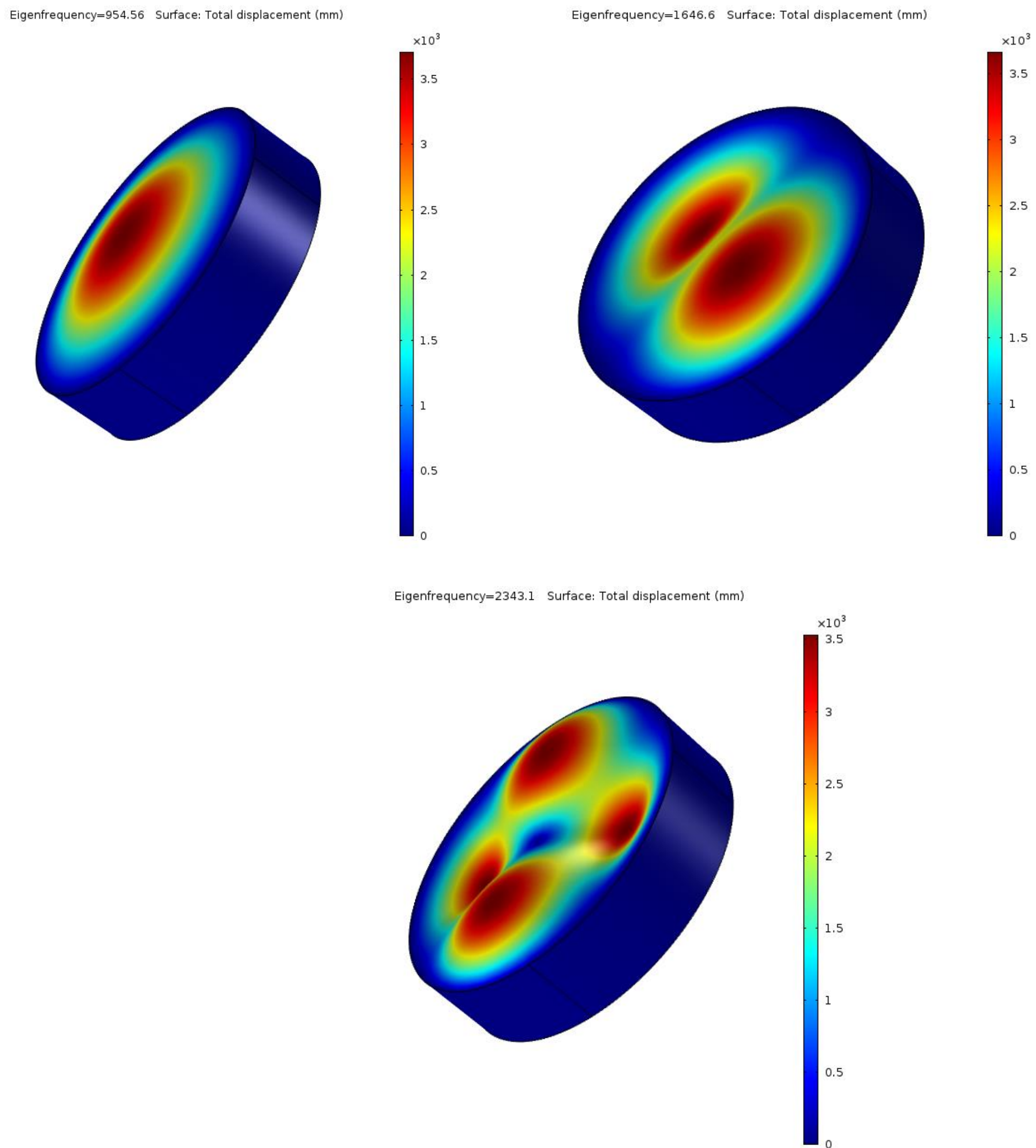

Fig. 4.17 First three vibration mode shapes of the diaphragm (design I)

Table 4.4 Vibration mode frequencies for design I

Mode Shapes	Frequency of diaphragm (Hz)	Frequency of complete structure (Hz)
First mode	954.56	910.08
Second Mode	1646.6	1283
Third Mode	2343.1	1832.9
Fourth Mode	2577.5	2210.6
Fifth Mode	2963	2797.8

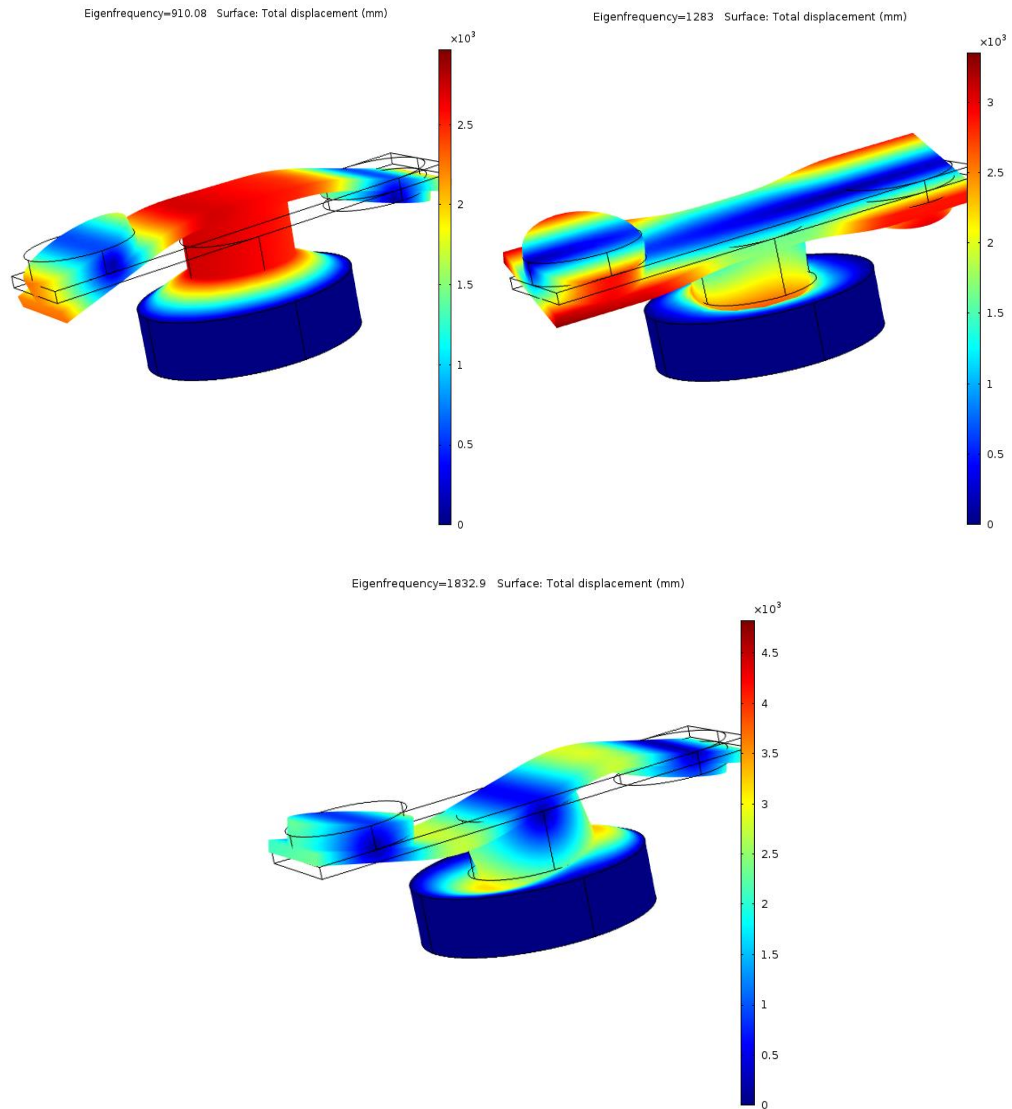

Fig. 4.18 First three vibration mode shapes for design I

The above analysis is also repeated for design II. The three vibrations modes and the five vibration mode frequencies (Eigen frequencies) of the diaphragm alone and complete structure with the diaphragm and the protrusion are shown in Fig. 4.19, Fig. 4.20 and in Table 4.5.

Table 4.5 Vibration mode frequencies for design II

Mode Shapes	Frequency of diaphragm (Hz)	Frequency of complete structure (Hz)
First mode	497.46	375.29
Second Mode	974.12	1278.8
Third Mode	1504.5	3334.6
Fourth Mode	1690.4	3422.2
Fifth Mode	2076.7	3512.9

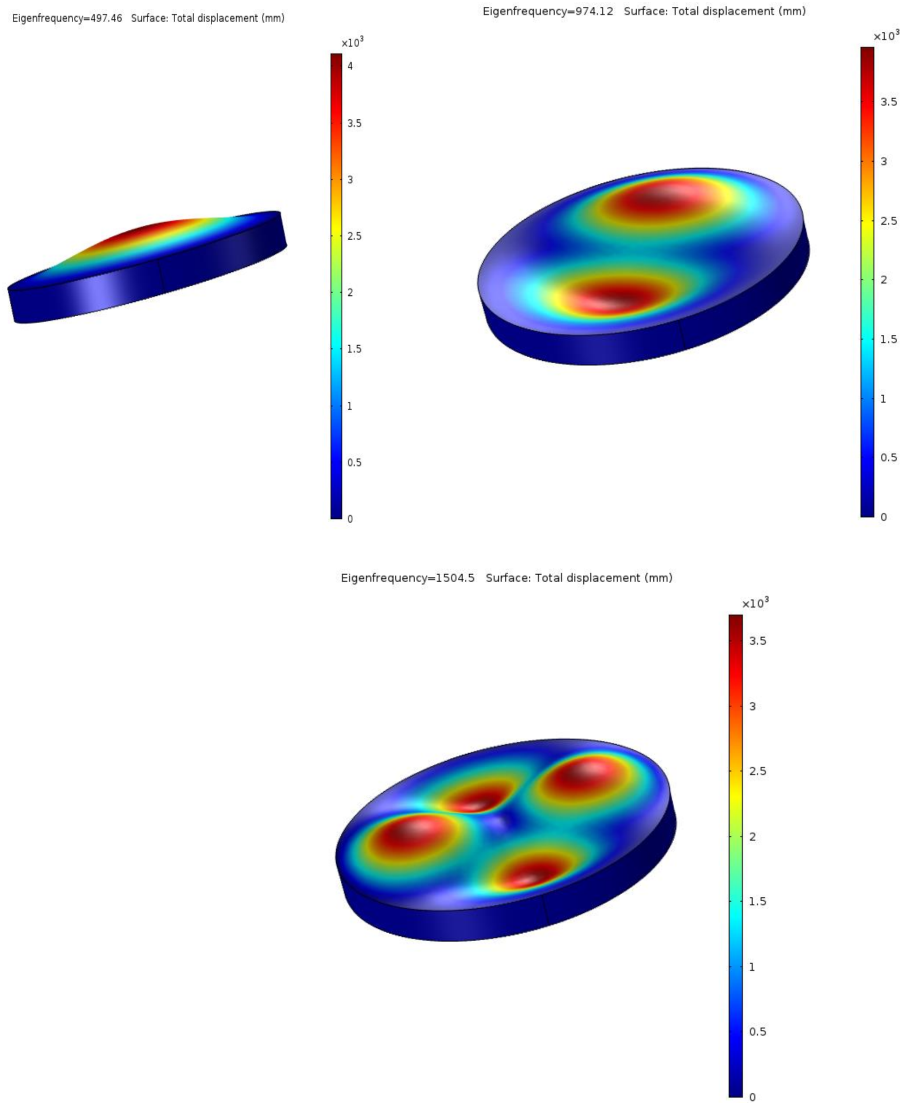

Fig. 4.19 First three vibration mode shapes of the diaphragm (design II)

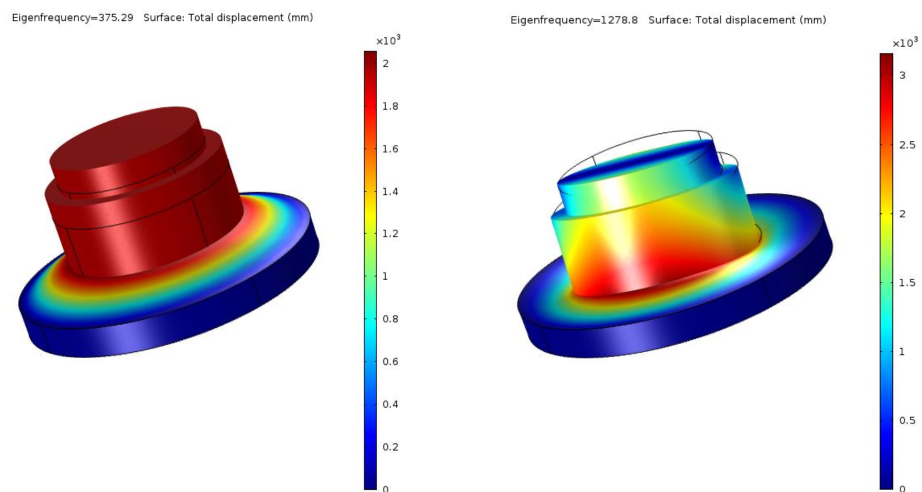

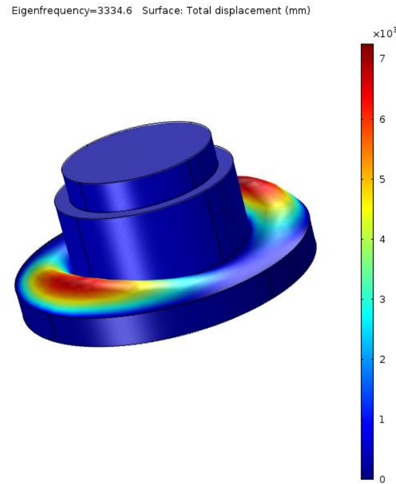

Fig. 4.20 First three vibration mode shapes for design II

From the above analysis, it can be concluded that while applying dynamic pressure to the sensor the frequency of the applied dynamic pressure should be kept far away from the mode frequencies specified in Table 4.1 and Table 4.2 for both designs to avoid their influence on the measured dynamic pressure.

4.7 Conclusion

A simple, cost-effective Hall effect based pressure sensor fabrication that was designed and simulated in Chapter 3 was attempted. A modified sensor design II along with the differential sensor design I were custom fabricated providing effective pressure measurement in the range of 0-1 bar. The calibration of the two pressure sensor designs is carried out in the same pressure range using a dead weight tester for 25 cycles of ascending and descending pressure and various static characteristics are obtained. The designed sensors show high repeatability with a resolution of 0.02 bar. The maximum nonlinearity for design I is 0.2% and 3.75% for design II. The maximum hysteresis for design I is 0.21% and 0.37% for design II and both the sensors were found to be accurate with a maximum +1.21 % error in design I and -4.08 % error in design II. Moreover, the design I has shown better performance as compared to design II from the analysis of experimental data. Both the fabricated sensors showed better characteristics as compared to other pressure sensors available in the literature. The output from both the sensors is in the form of measurable Hall voltage from the Hall sensors, suitable wired and wireless transmitters can be employed to transmit the pressure sensor data to a remote location.

Chapter 5

Wired and Wireless Hall Effect Based Pressure Transmitters

5.1 Introduction

Sensor data transmission is an important aspect in process industries. The transmitted sensor data can be used to monitor the process variable or for controlling other variables like temperature, pressure, flow, etc. The sensor data transmission becomes more useful in case of hazardous industries where a human operator is not allowed to access the sensor location. Both wired and wireless sensor data transmission is currently in use in all industrial applications. Various sensor data transmission techniques are available in the literature. An electronics level transmitter based on the measurement of hydrostatic pressure is designed and developed [69]. The level sensing is done by measuring the hydrostatic pressure at the base of the container using Hall sensors. A wired transmitter is designed with the help of signal conditioning circuitry that includes instrumentation amplifier, a zero, gain and span circuit and a voltage to current converter circuit. The signal conditioning circuit converts the sensor data in the form of 4-20 mA current signal and then it is transmitted to a remote indicator. A similar electronic level transmitter is also designed using interdigital capacitor [70]. The level is measured using inter digital capacitor as a primary sensing element. The change in capacitance with level is converted to electrical signal with the help of a suitable bridge circuit. The signal from the bridge is passed through a precision rectifier circuit to convert to a DC signal. The DC signal is given to a zero, gain and span circuit to convert the signal in the range of 1-5V. The signal is then given to a voltage to current converter circuit which converts the signal to a 4-20mA current signal which is transmitted to a remote indicator. A wireless sensor network for temperature measurement in hostile environments is demonstrated [71]. A highly reliable network architecture is designed based on a distributed coordinator. In [72] a wireless air flow transmitter is designed using resistive type flex band sensor to sense the airflow. The data is transmitted wirelessly with the help of an Arduino microcontroller and ESP8266 Wi-Fi module. In [73] an air quality monitoring system based on Internet of things (IoT) is presented. The system monitors components of air quality such as temperature, humidity, CO and CO_2. LPWAN Lora was used for data transmission and for cloud services. A wireless sensor network based on IoT for precision agriculture is designed and various parameters helpful for agriculture are monitored using wireless sensor nodes [74].

In this chapter, both wired and wireless transmitter were hardware implemneted on the fabricated sensor designs (I and II). A wired transmitter is deigned to give a current ouput that can be transmitted and observed on a remote indicator and a wireless transmitter is designed uisng a Wi-Fi module to transmit the data and a cloud server to access and retrive the transmitted data.

5.2 Implementation of Wired and Wireless Transmitter

Two methods of data transmission for both pressure sensor designs (I and II) fabricated and tested in Chapter 4 have been presented in this work. One is a wired transmitter and the other is IoT-based wireless transmitter.

5.2.1 Wired Transmitter

The 4-20 mA current loop has been the standard signal for transmission and electronic control in all process industries. In this current loop, the signal is drawn from a DC source which flows through the transmitter and then back to the power source in a series circuit. The major advantage of using a current signal is that the current value does not degrade over long distances whereas in the case of a voltage signal a voltage drop is developed according to Ohm's law which is proportional to the length of the cable. In the design of the wired transmitter, suitable circuitry is used to convert the actual output data from the sensor to a 4-20 mA current signal before transmission. Wired transmitters are designed for both the fabricated sensor designs and the block diagrams for design I is shown in Fig. 5.1.

In sensor design I, the measured Hall voltage output from the sensor is in the range of 7-33 mV. Since the output voltage from sensor design I is a differential voltage with low amplitude, an Instrumentation amplifier AD620 is used to amplify the differential output. The output of the instrumentation amplifier is in the range of 0.7-3.346 V. In the first stage, a signal conditioning circuit is used to convert the instrumentation amplifier output to a voltage range of 1-5 V. The corresponding 1-5 V voltage output from the first stage is converted to a 4-20 mA current signal by a V-I converter circuit in the second stage. The output V_0 of the signal conditioning circuit and the output V_{01} of the V-I converter circuit is given in Eq. (5.1) and Eq. (5.2). The current across the output load R_{f1} is given by Eq. (5.3). The instrumentation amplifier, op-amp based signal conditioning circuit along with the V-I converter circuit are shown in Fig. 5.2. The instrumentation amplifier gain can be

controlled by choosing a suitable external resistance R_G. The pin configuration of AD620 is shown in Fig. 5.3. The relationship between gain and R_G is given in Eq. (5.4).

$$V_o = \frac{R_f}{R_i} V_{in} + \frac{R_f}{R_{os}} V_{ref} \tag{5.1}$$

$$V_{o1} = \left(1 + \frac{R_{f1}}{R}\right) V_o \tag{5.2}$$

$$I = \frac{V_o}{R} \tag{5.3}$$

$$G = 1 + \frac{49.4\ k\Omega}{R_G} \tag{5.4}$$

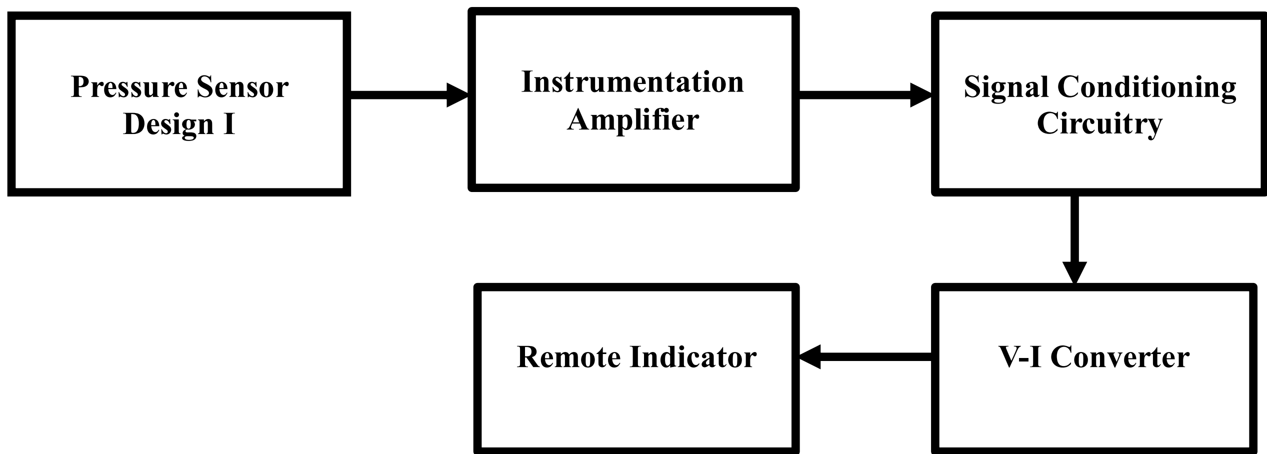

Fig. 5.1 Block diagram of a wired transmitter (design I)

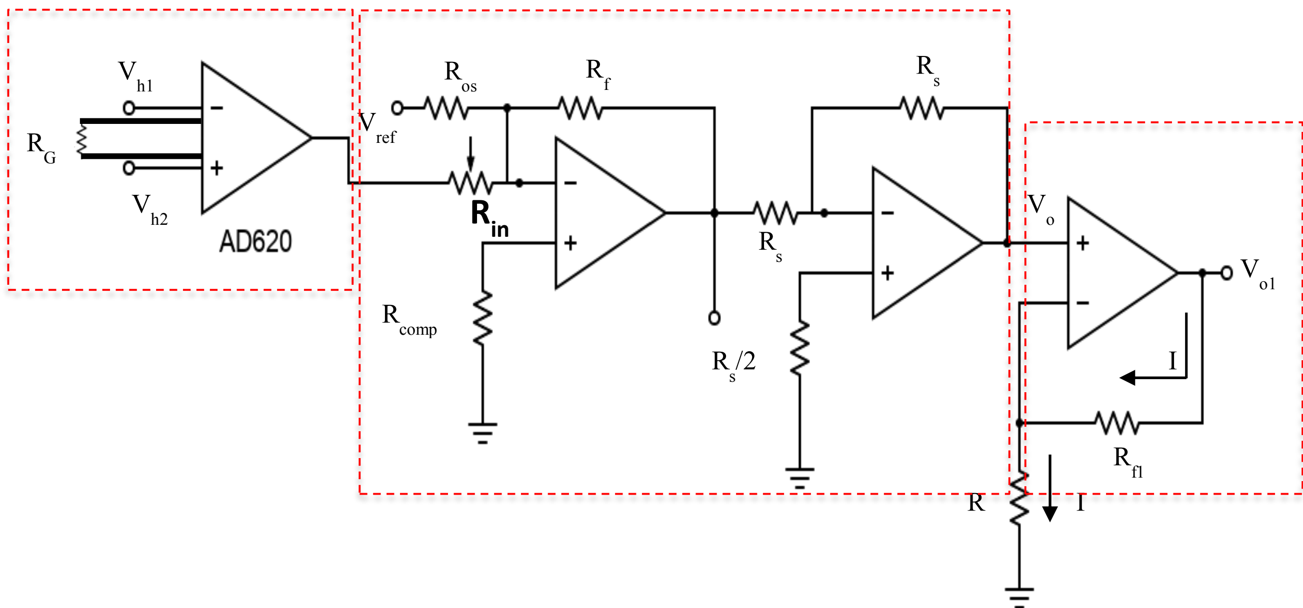

Fig. 5.2 Wired transmitter circuit implementation for design I

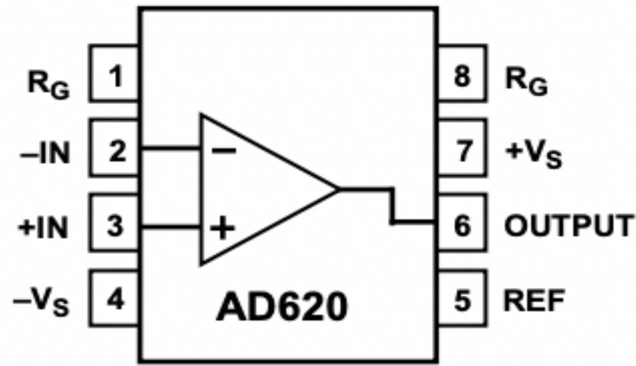

Fig. 5.3 Pin-out of AD620 Instrumentation amplifier IC

In sensor design II, the measured Hall voltage output from the sensor is in the range of 5.02 – 5.27 V. In the first stage, a signal conditioning circuit is used to convert the actual output to a voltage range of 1-5 V and this voltage is converted to a 4-20 mA current signal by using a V-I converter circuit in the second stage similar to design I transmitter. The block diagram of wired transmitter and circuit implementation for design II is shown in Fig. 5.4 and Fig. 5.5.

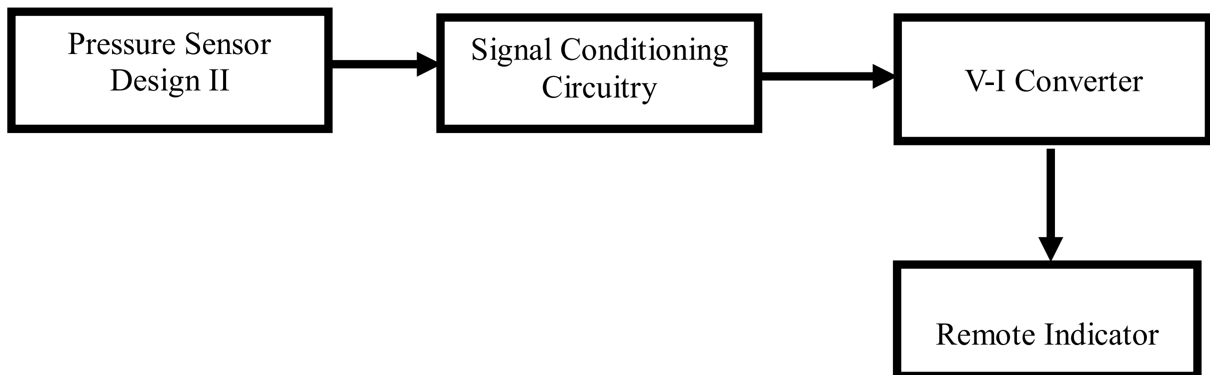

Fig. 5.4 Block diagram of a wired transmitter (design II)

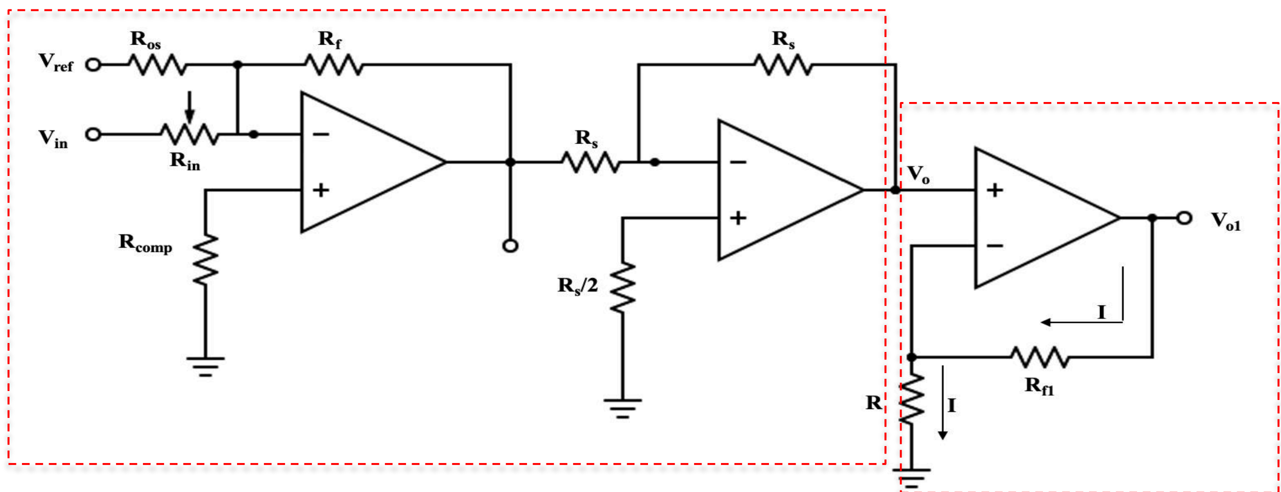

Fig. 5.5 Wired transmitter circuit implementation for design II

5.2.2 Wireless Transmitter

Wireless data transmission and IoT have gained a lot of popularity in recent years. Data from IoT can be accessed anywhere via the internet and hence IoT makes the work environment safe in hazardous locations. IoT has also gained popularity in process industries where it is used to transmit sensor data measuring various physical quantities wirelessly so that the data can be accessed from anywhere in the plant and also outside the plant after providing proper authentication. In the design of a wireless transmitter, a NodeMCU ESP module is used as hardware and the Blynk IoT cloud console is used as an IoT cloud server for storing and accessing the pressure sensor data. NodeMCU is enabled with the ESP8266 Wi-Fi chip and has one analog I/O and 8 digital I/O pins and supports serial communication. The block diagram of the wireless transmitter for sensor design I and design II is shown in Fig. 5.6 and Fig. 5.7.

For transmitting the sensor data wirelessly in sensor design I, the same instrumentation amplifier and signal conditioning circuit (first stage) implemented for wired transmitters is used to convert the actual sensor data to a range of 1-5 V. Since, the operating voltage of NodeMCU is 3.3 V, we use a potential divider to step down the voltage to a range of 0-3.3 V. The output of the potential divider is connected to the analog I/O pin of the NodeMCU to transmit the data to the IoT cloud server. The complete op-amp based circuit implementation is shown in Fig. 5.8. Similar circuitry was implemented for sensor design II as shown in Fig. 5.9 without an instrumentation amplifier.

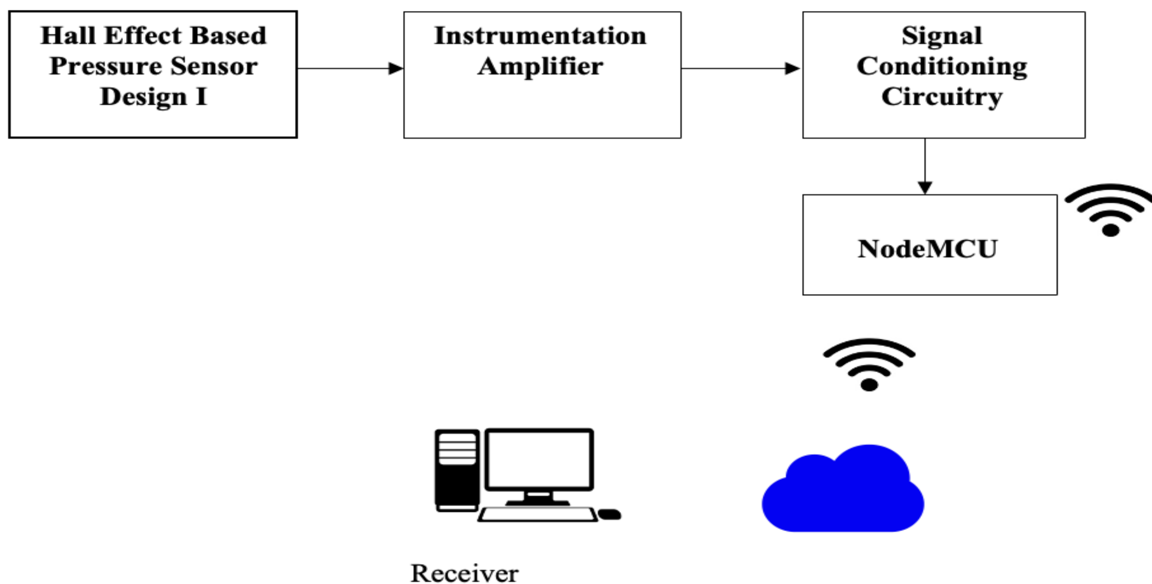

Fig. 5.6 Block diagram of a wireless transmitter for design I

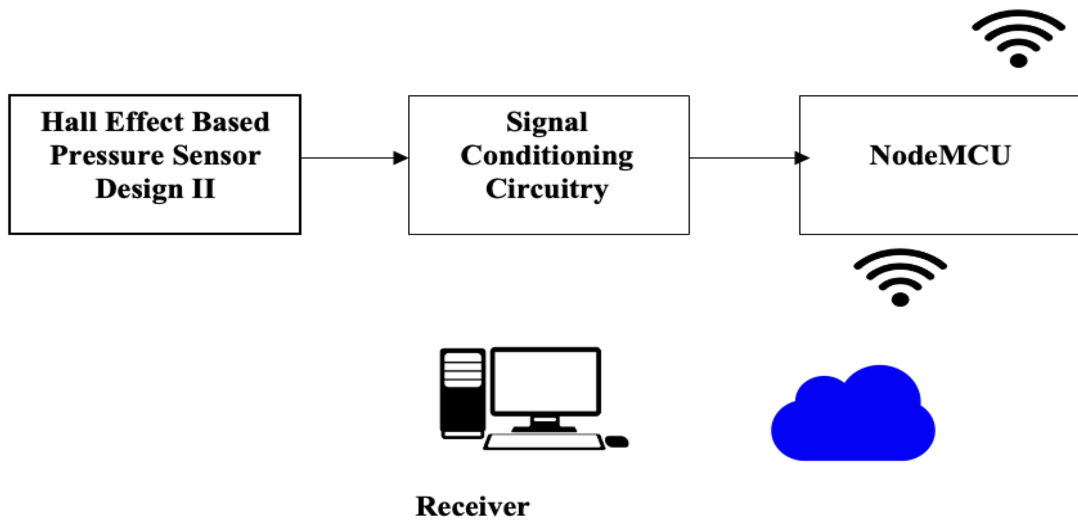

Fig. 5.7 Block diagram of a wireless transmitter for design II

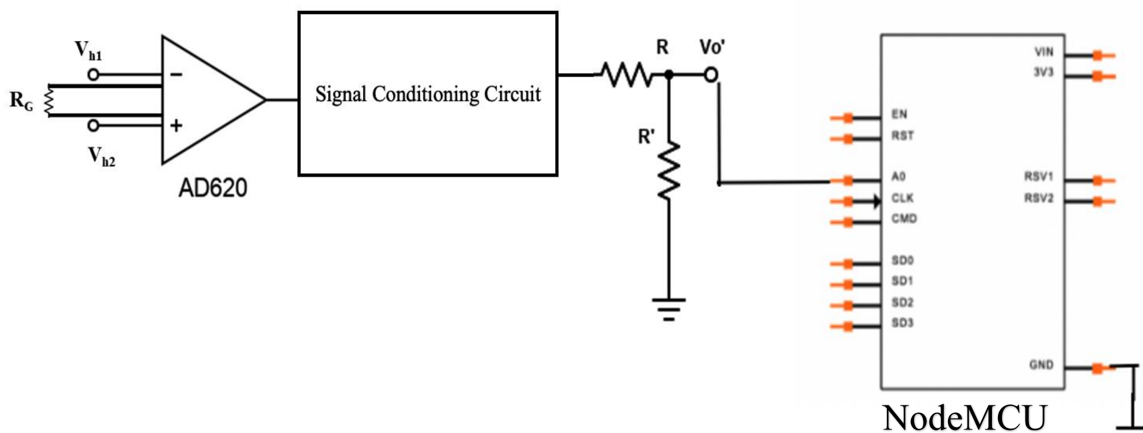

Fig. 5.8 Wireless transmitter circuit implementation for design I

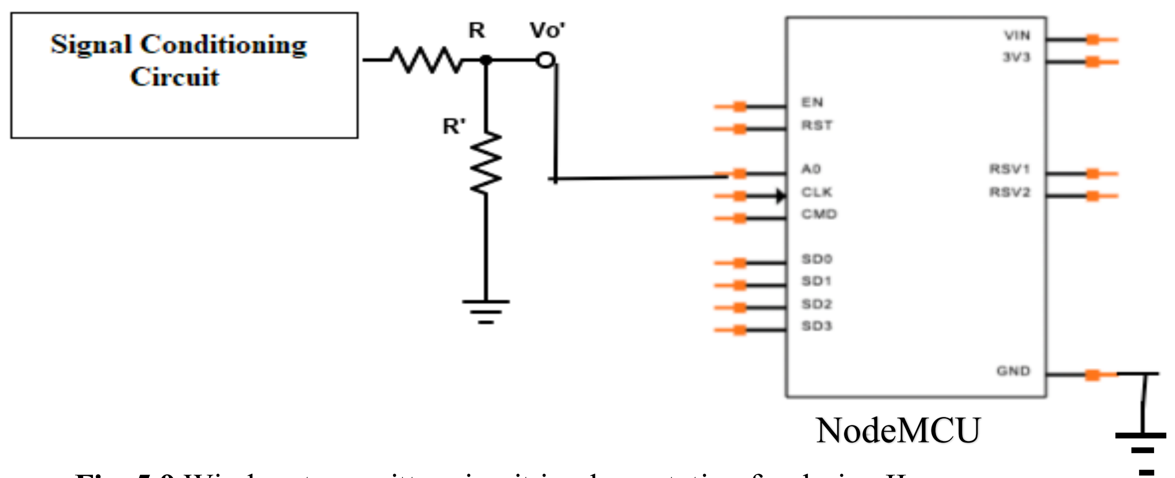

Fig. 5.9 Wireless transmitter circuit implementation for design II

5.3 Experimental Results

A dead weight tester (Yantrika Instruments) is utilized to apply a standard pressure input in the range of 0-1 bar to test the output of wired and wireless transmitters. In the case of a wired transmitter, the span voltage is measured with the help of a DSO (Tektronix) and the equivalent current signal is measured using a digital multimeter (Fluke 179). The complete experimental setup for sensor design II is shown in Figure 5.10. A similar experimental setup is also implemented for sensor design I.

Fig. 5.10 Experimental setup of a wired transmitter for design II

In the case of a wireless transmitter, the voltage output of the signal conditioning circuit is connected to NodeMCU as shown in Fig. 5.8 and Fig. 5.9 for both sensor designs (I and II). The experimental setup of wireless transmitter for design II is shown in Fig. 5.11. A similar experimental setup is also implemented for sensor design I. NodeMCU shown in Fig. 5.12 has one analog I/O and 8 digital I/O pins to support serial communication. The operating Voltage of NodeMCU IS 3.3 Vand it has a built in Wi-Fi module and a 32-bit microcontroller.

With the help of NodeMCU, the sensor data is transmitted to the blynk IoT cloud server where the data can be accessed after providing proper authentication. The Blynk console displays analog voltage value corresponding to the transmitted voltage which is in terms of applied pressure. In the console we can see the latest pressure value which updates every three seconds according to the pressure applied. It also stores all values for last hour, 6

hours day etc. In the blynk login we can add more than one device and the data can be monitored simultaneously. The info of the device being used can also be accessed under device info. A typical link to access data on blynk IoT is https://blynk.cloud/dashboard/93802/global/filter/511831/organization/93802/devices/339378/dashboard. (Includes user id and device id.). The screenshot of the Blynk IoT console is shown in Fig. 5.13 which shows the corresponding received voltage of 2.69 V for 0.7 bar input pressure for design II.

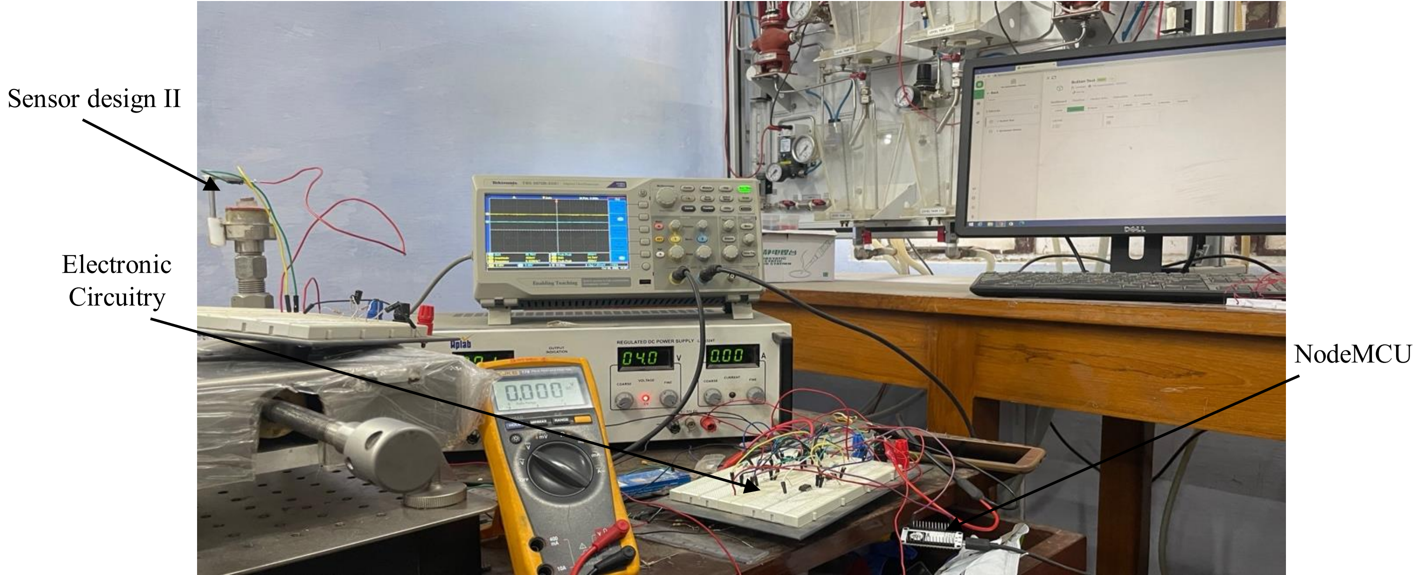

Fig. 5.11 Experimental setup of a wireless transmitter for design II

Fig. 5.12 NodeMCU

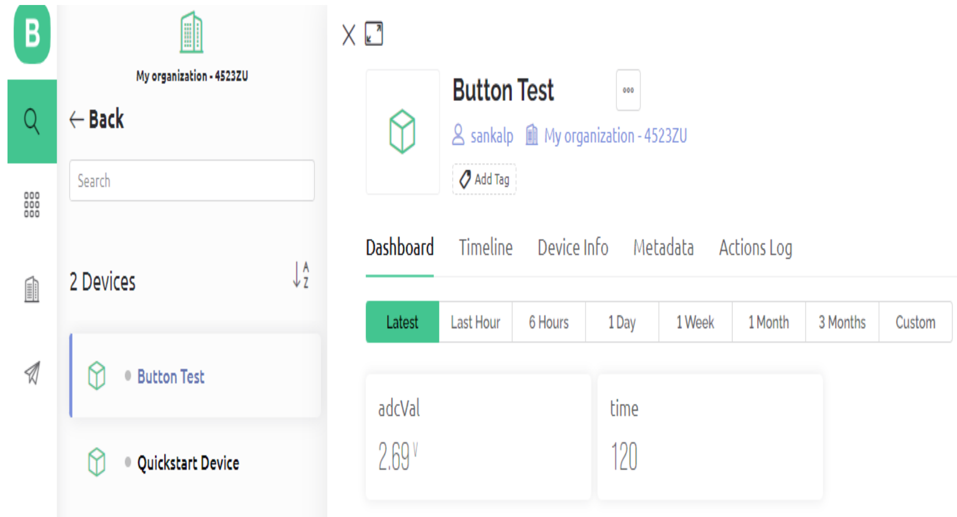

Fig. 5.13 Blynk IoT console

5.3.1 Design I

The straight-line fit equation obtained from the instrumentation amplifier output V_{ins}, signal conditioning circuit output V_o and V-I converter circuit output I are given in Eq. 5.5- Eq. 5.7. The signal conditioning circuit output and V-I converter output in the pressure range of 0-1 bar is shown in Fig. 5.14 and Fig. 5.15.

$$V_{ins} = 3.071P + 0.708 \quad (5.5)$$

$$V_o = 4.0447P + 1.0027 \quad (5.6)$$

$$I = 16.357P + 4.0593 \quad (5.7)$$

Where P is the input pressure (bar). The % nonlinearity and % error for the current output I is shown in Fig. 5.16 and Fig. 5.17. For the wireless transmitter, the transmitted data by the NodeMCU and received data by the blynk IoT console is shown in Table 5.1.

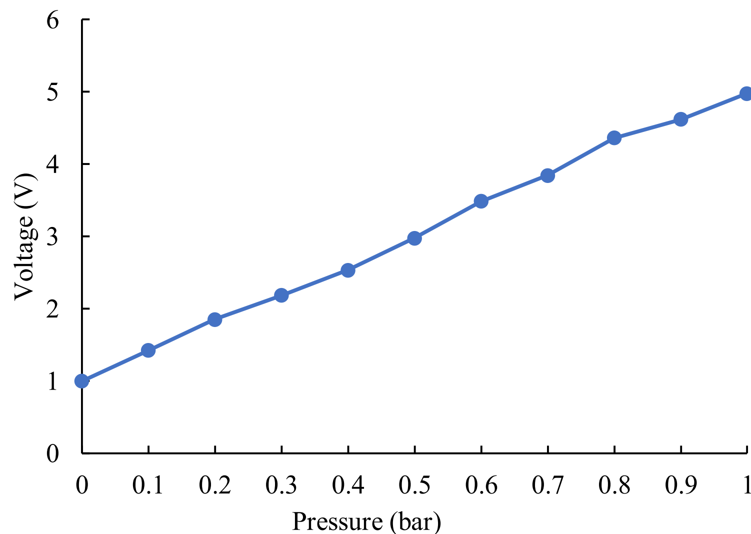

Fig. 5.14 Signal conditioning circuit output (V_o)

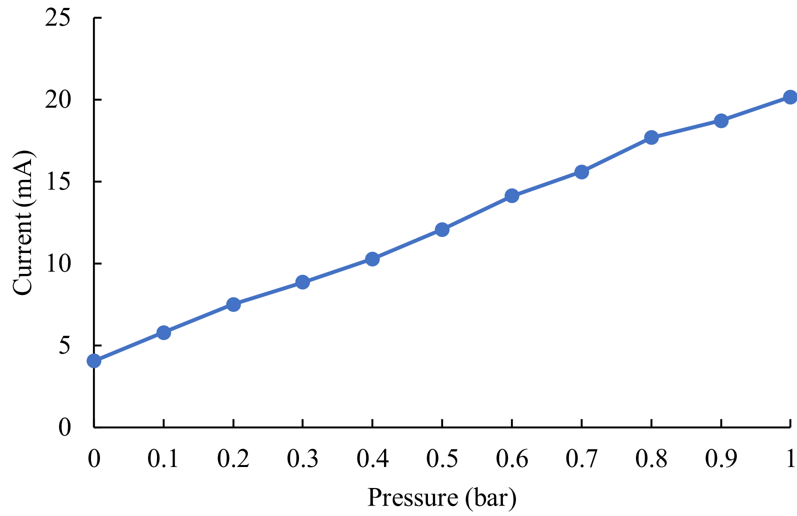

Fig. 5.15 V-I converter output (I)

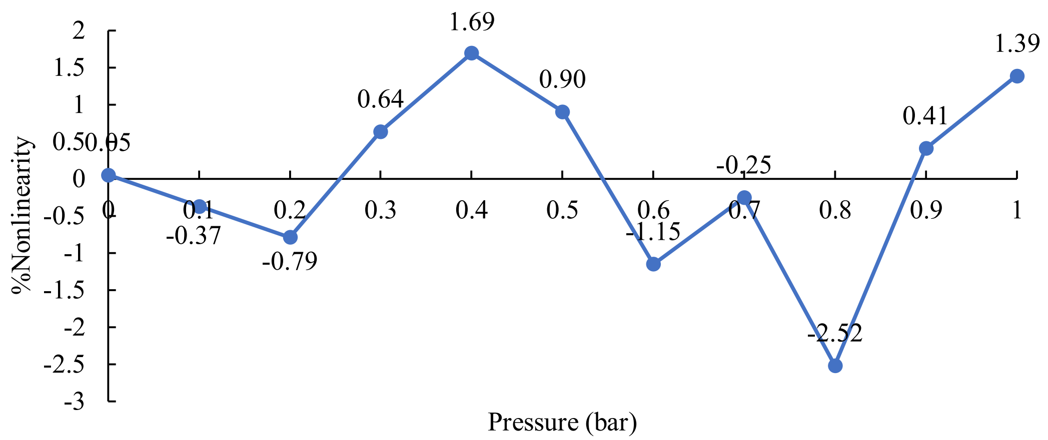

Fig. 5.16 % Nonlinearity for V-I converter output

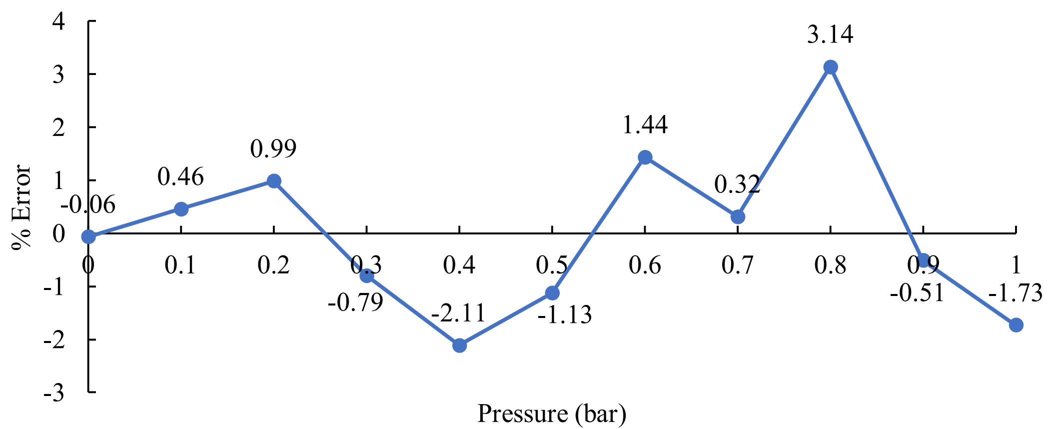

Fig. 5.17 % Error for V-I converter output

Table 5.1 Transmitted data vs Received Data

Input Pressure (bar)	Transmitted voltage (V)	Received voltage (V)
0	0.69	0.64
0.1	0.97	0.93
0.2	1.25	1.20
0.3	1.52	1.48
0.4	1.80	1.75
0.5	2.08	2.01
0.6	2.36	2.31
0.7	2.64	2.59
0.8	2.91	2.85
0.9	3.19	3.14
1	3.47	3.42

5.3.2 Design II

The straight-line fit equation obtained from the signal conditioning circuit output V_o and V-I converter circuit output I are given by Eq. 5.8 and Eq. 5.9 and are shown in Fig. 5.18 and Fig. 5.19.

$$V_0 = 3.9285P + 1.0775 \tag{5.8}$$

$$I = 15.903P + 4.3597 \tag{5.9}$$

Where P is the input pressure (bar). The % nonlinearity and the % error for the current output I is shown in Fig. 5.20 and Fig. 5.21. The transmitted data by the NodeMCU and received data by the blynk IoT console is shown in Table 5.2.

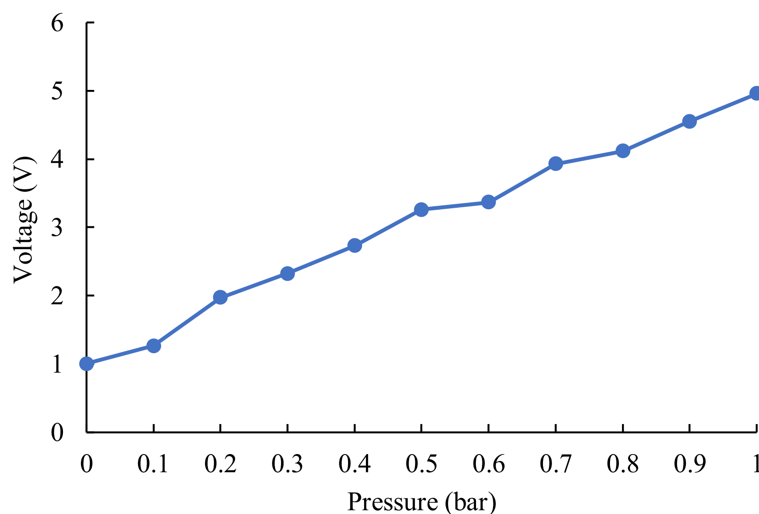

Fig. 5.18 Signal conditioning circuit output (V_o)

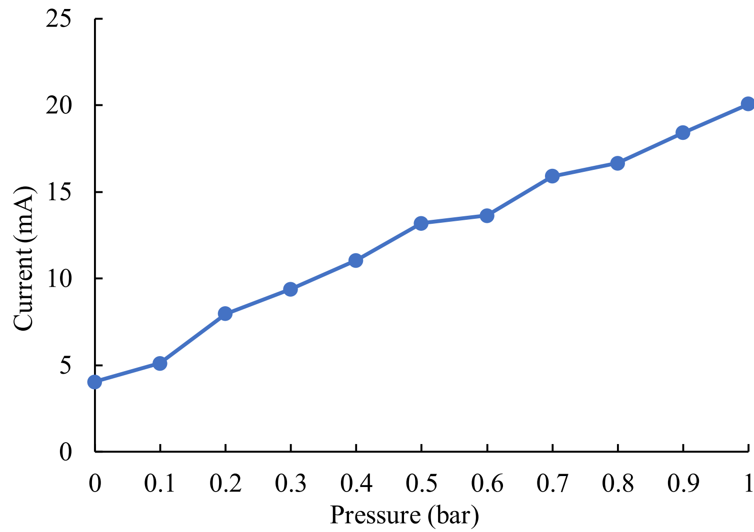

Fig. 5.19 V-I converter output (I)

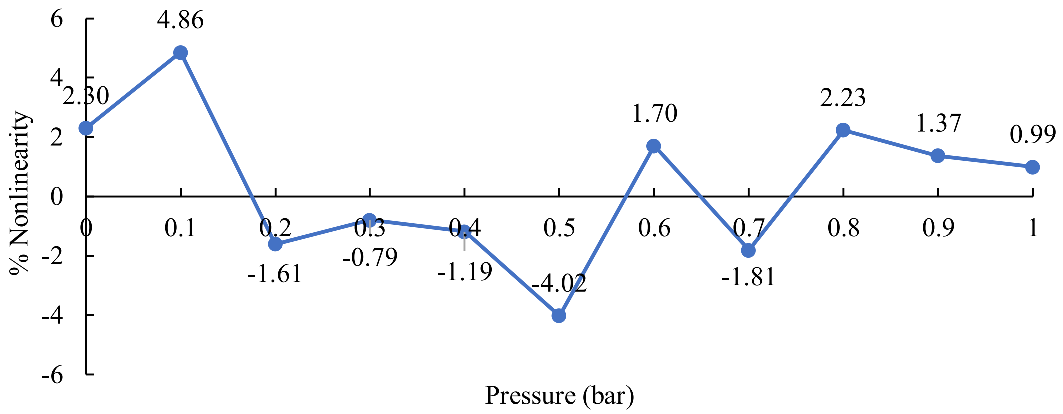

Fig. 5.20 % Nonlinearity for V-I converter output

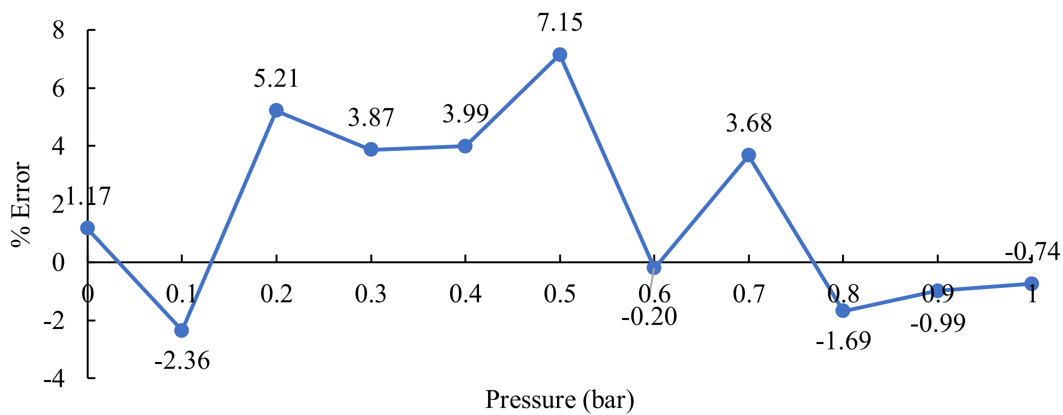

Fig. 5.21 % Error for V-I converter output

Table 5.2 Transmitted data vs Received data

Input pressure (bar)	Transmitted voltage (V)	Received voltage (V)
0	0.77	0.72
0.1	1.03	0.98
0.2	1.30	1.25
0.3	1.57	1.52
0.4	1.84	1.79
0.5	2.10	2.03
0.6	2.37	2.32
0.7	2.72	2.69
0.8	2.91	2.86
0.9	3.17	3.12
1	3.44	3.4

5.4 Conclusion

A wired and wireless transmitter has been implemented experimentally on fabricated pressure sensors demonstrated in chapter 4. Two designs of the pressure sensor are used in the implementation of the wired and wireless transmitters. The wired transmitter has a signal conditioning circuit followed by a voltage-to-current converter circuit to give a 4-20 mA current signal for lossless data transmission over long distances. The current output of the wired transmitter showed good linearity and accuracy for both sensor designs. A wireless transmitter is also implemented which employs a NodeMCU with a built in Wi-Fi module for data transmission and a Blynk IoT console cloud server for data storage and data retrieval. The output from the signal conditioning circuit is followed by NodeMCU for wireless data transmission instead of a voltage-to-current converter circuit in both sensor designs. The received sensor data observed in the Blynk IoT console is in good agreement with the transmitted sensor data by the wireless module. The advantage of the wireless transmission with IoT integration will allow the pressure sensor data to be accessed remotely through the internet. The proposed transmitters can be directly implemented in all process industries for wireless monitoring and control applications.

Chapter 6
Design and Simulation of Digital Output MEMS Pressure Sensor

6.1 Introduction

The most important variable in most process industries is the pressure which must be carefully measured and monitored. MEMS pressure sensors are commercially available for the past two decades. There are applications that require an easily transmittable digital output and hence digital MEMS pressure sensors are also gaining popularity in the industry. These types of sensors are free from the inherent disadvantages of conventional piezoresistive and capacitive pressure sensors. In this chapter, three different sensor designs based on the above literature by combining pressure sensor with a mechanism for digital readout were proposed. The initial design has ten different square diaphragms on a substrate the of same thickness with different side lengths. The second design uses only one square diaphragm instead of ten diaphragms for the same pressure range and resolution. The third design uses a single circular diaphragm with a boss structure [92] to get a digital logic output for the specified pressure range and resolution.

6.2 Design and Principle of Operation

The pressure sensor was realized on a silicon substrate which consists of an array of thin square diaphragms for applying input pressure. The thickness of each diaphragm is fixed, and the lateral dimensions of the diaphragms are varied according to the input pressure range. Two cantilever shaped metallic beams are arranged on either side of a single diaphragm facing each other as shown in Fig. 6.1(a). The square diaphragm has a small metallic protrusion at its centre, and a predefined gap d exists between the metallic protrusion on the diaphragm and free ends of the two cantilever beams. The top view of a single diaphragm in Fig. 6.1(b) shows the metallic protrusion at the centre of the diaphragm, a supply contact pad (SCP), output contact pad (OCP) and a ground contact pad (GCP). A polysilicon piezoresistor is electrically connected between output contact pad (OCP) and ground contact pad (GCP) through metallic strip interconnects. These diaphragms are arranged in multiple arrays on a common substrate to measure the input pressure with a specific resolution.

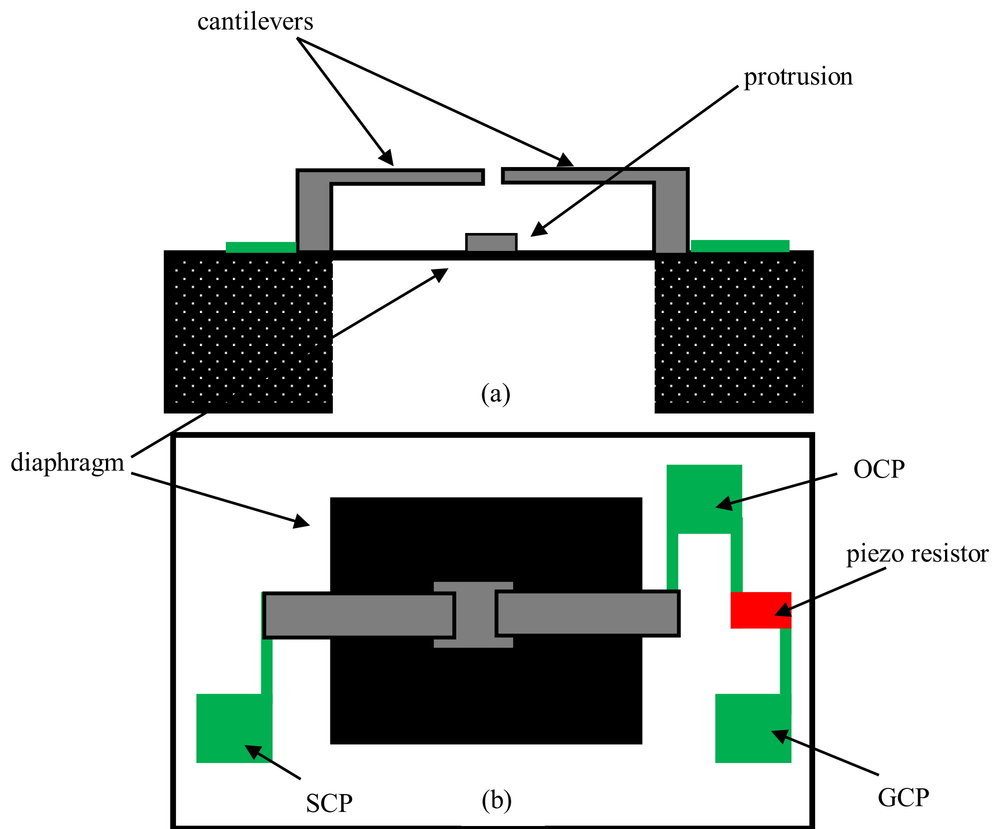

Fig. 6.1 Initial design of a single diaphragm of the sensor (a) side view (b) top view

The silicon diaphragm with a central metallic protrusion and two cantilevers together acts as a mechanical switch in the sensor design. A DC power supply is provided to SCP, and the output is taken across the piezoresistor, i.e., from OCP and GCP. In the absence of pressure, the diaphragm will not deflect and the switch is open and the output will be considered as logic '0' or no connection (NC). With the application of pressure, the diaphragm deflects causing the metallic protrusion to establish a contact at the free end tip of the two cantilevers thereby closing the switch as shown in Fig. 6.2. When the switch is closed, the output will be considered as logic '1' and the central deflection of the diaphragm will be equal to the predefined gap d.

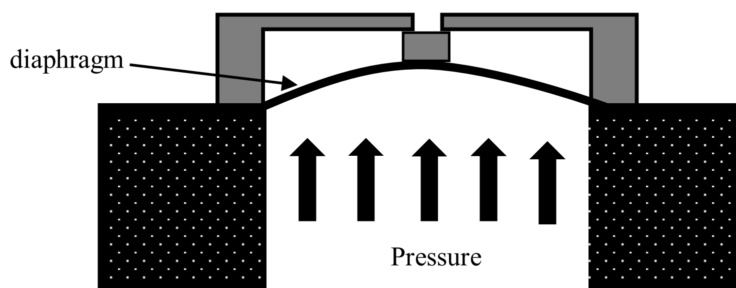

Fig. 6.2 Diaphragm under applied input pressure

For a pressure range of 0-1 bar and with a resolution of 0.1 bar, the sensor requires ten diaphragms D1 to D10 of a similar arrangement shown in Fig. 6.1(a) on a single base substrate with same thickness and different lateral dimensions (side lengths) as shown in Fig. 6.3. When a pressure of 0.1 bar is applied to the entire diaphragm array, the diaphragm D1 is designed to have a deflection equal to the predefined gap *d*. The switch will be closed giving an output of logic '1.' If the pressure is increased to 0.2 bar, then the diaphragm D2 is designed to have a deflection equal to *d* and thereby gives an output logic '1.' The digital outputs from all the diaphragms for pressure in the range of 0-1 bar are specified in Table 6.1.

In order to reduce the number of diaphragms and to increase the resolution of the sensor, a modified design (design I) which uses a single diaphragm was proposed to achieve the same digital output. The 3D view and top view of a single square diaphragm with contact pads are shown in Fig. 6.4. This design is similar to the previous design but has an array of metallic protrusions of different heights positioned along the central axis of the diaphragm with a fixed predefined gap d_1 (gap between the cantilever free ends and the diaphragm) as shown in Fig. 6.4(a). Each metallic protrusion along with the pair of cantilevers forms a switch with multiple output contact pads, common supply and ground contact pad as shown in Fig. 6.4(b). For the same pressure range of 0–1 bar with a resolution of 0.1 bar, the design I requires only one diaphragm on a single substrate with ten protrusions (P1–P10), single SCP, single GCP and ten output contact pads (OCP1 to OCP10) as shown in Fig. 6.5.

When a pressure of 0.1 bar is applied, the protrusion P1 height is designed such that the diaphragm deflection will make that particular switch to close giving an output from OCP1 as logic '1.' If the pressure is increased to 0.2 bar, the protrusion P2 height is designed to give an output logic '1' taken from OCP2.

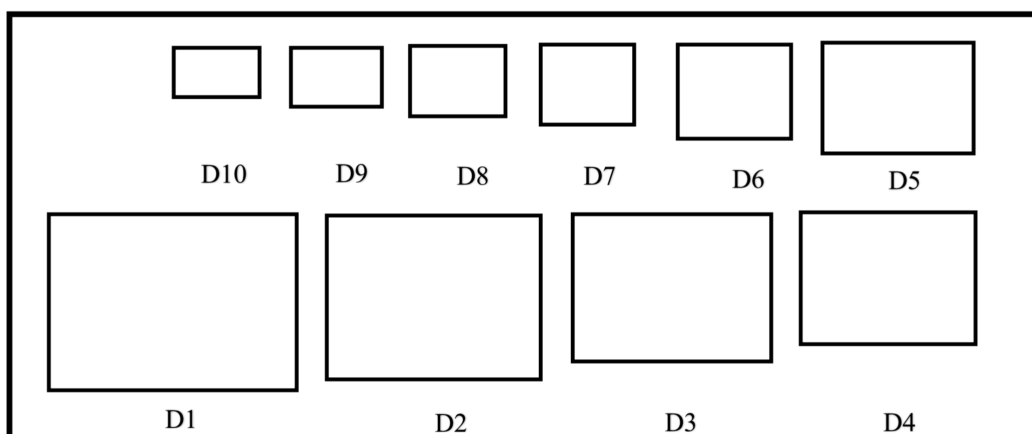

Fig. 6.3 Top view showing the diaphragm array of the initial sensor design

Table 6.1 The logic table for various applied pressures

Pressure (bar)	D1	D2	D3	D4	D5	D6	D7	D8	D9	D10
0.1	1	0	0	0	0	0	0	0	0	0
0.2	1	1	0	0	0	0	0	0	0	0
0.3	1	1	1	0	0	0	0	0	0	0
0.4	1	1	1	1	0	0	0	0	0	0
0.5	1	1	1	1	1	0	0	0	0	0
0.6	1	1	1	1	1	1	0	0	0	0
0.7	1	1	1	1	1	1	1	0	0	0
0.8	1	1	1	1	1	1	1	1	0	0
0.9	1	1	1	1	1	1	1	1	1	0
1	1	1	1	1	1	1	1	1	1	1

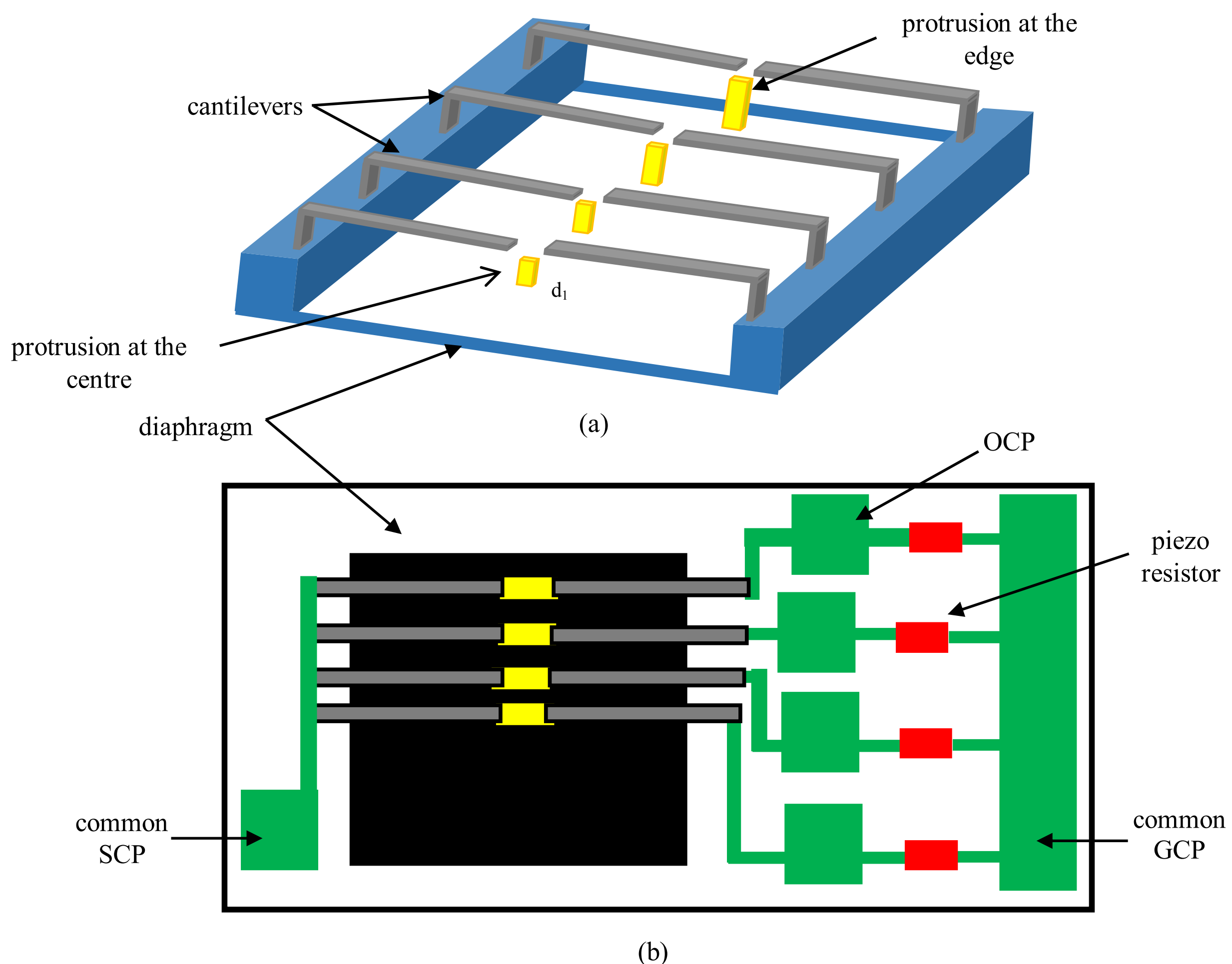

(b)

Fig. 6.4 Design I of the sensor (a) 3D view (b) top view

The pressure deflection characteristics of a diaphragm are nonlinear [93] and can be made linear by assuming that the maximum deflection is very small as compared to the thickness of the diaphragm. If this assumption cannot be made, the pressure deflection characteristics of a diaphragm will be nonlinear. In order to reduce the nonlinearity in the diaphragm deflection, a boss structure has been introduced in the diaphragm [91, 92]. A further modified design (design II) was proposed which consists of a circular diaphragm with a central circular boss structure with an array of metallic protrusions of different heights

positioned on the boss structure of the diaphragm with a fixed predefined gap d_2 (gap between the free end of the cantilevers and the circular boss structure of the diaphragm) in a circular fashion as shown in Fig. 6.6(a). Each metallic protrusion along with the pair of metallic cantilevers arranged side by side forms a switch with multiple output contact pads as shown in Fig. 6.6(b).

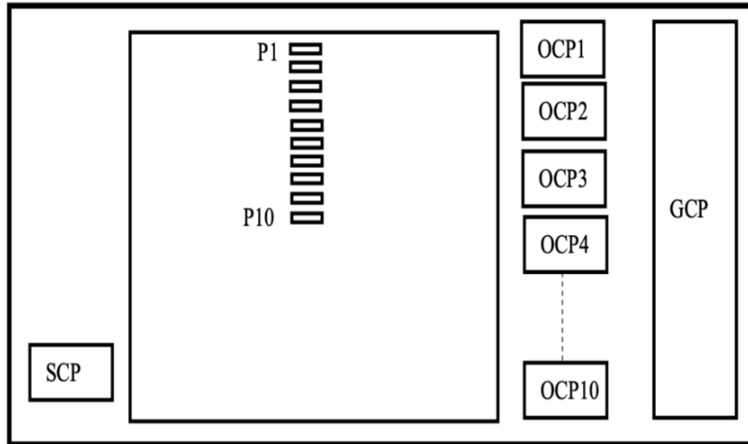

Fig. 6.5 Top view showing the diaphragm with protrusions and contact pads

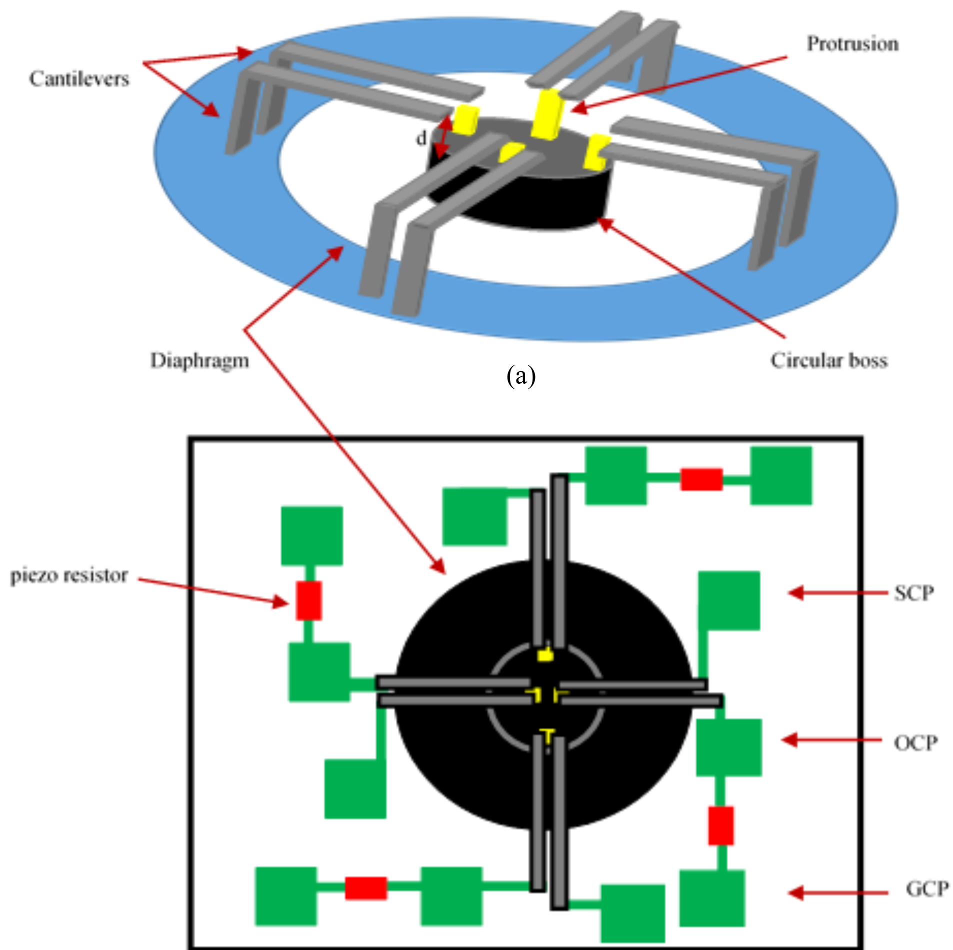

Fig. 6.6 Design II of the sensor (a) 3D view (b) top view

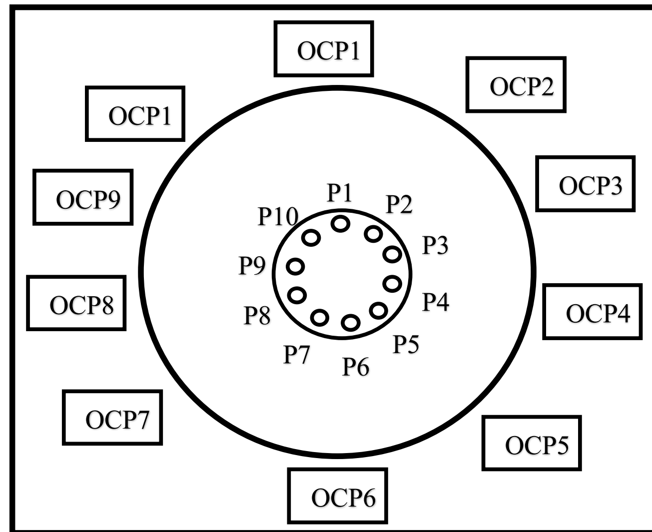

Fig. 6.7 Top view showing the boss diaphragm with protrusions and contact pads

For the same pressure range, the design II requires only one diaphragm on a single substrate with ten protrusions P1–P10 and ten output contact pads (OCP1 to OCP10) as shown in Fig. 6.7. The principle of operation will be the same as the previous design except the protrusions are deflected by the central deflection of rigid boss of the diaphragm with the applied pressure. The equivalent circuit representation of a single switch in the proposed sensor designs along with its ON and OFF states is shown in Fig. 6.8.

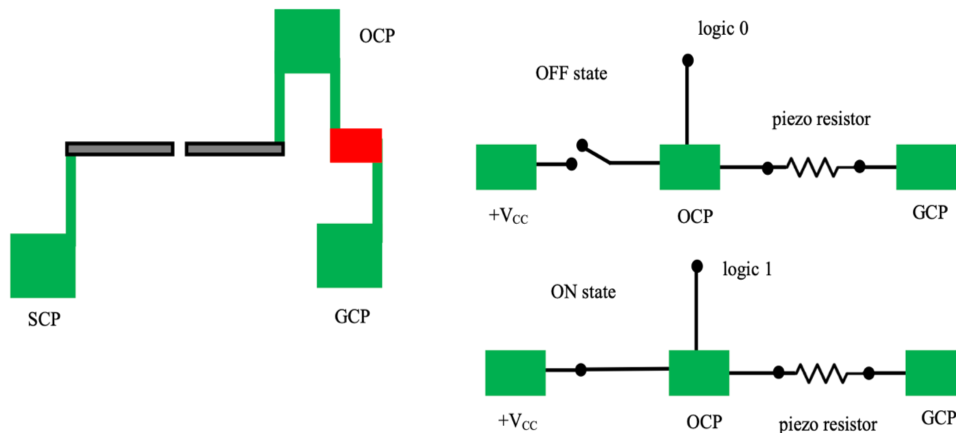

Fig. 6.8 Equivalent circuit of a switch during ON and OFF state

6.3 Analytical Modelling

Analytical expressions were obtained for a square diaphragm and circular diaphragm with a boss structure to estimate the pressure deflection characteristics by using MATLAB as a mathematical tool in the operating pressure range of 0-1 bar. The sensor

design shown in Fig. 6.1 (initial design), the diaphragm design is the most crucial step among the various stages of pressure sensor realization. For a square diaphragm of thickness h and side length $2a$, subjected to a uniform pressure P, with all its edges fixed in all directions, the central deflection w_0 is given by Eq. (6.1) [93].

$$w_0 = 0.22\frac{Pa^4}{Eh^3} \tag{6.1}$$

The side length of the diaphragm for a given pressure is given by Eq. 6.2

$$a = \left(\frac{w_0 Eh^3}{0.22P}\right)^{0.25} = \left(\frac{dEh^3}{0.22P}\right)^{0.25} \tag{6.2}$$

where E is the young's modulus of silicon diaphragm. For a fixed diaphragm thickness h of 5 µm, and fixed gap d of 0.5 µm, the side length $2a$ for ten square diaphragms in the pressure range of 0-1 bar is estimated from Eq. (6.2) and tabulated in the first column of Table 6.2. The diaphragm with the largest side length will be D1, and the smallest will be D10 as shown in Fig. 6.3.

In the design I shown in Fig. 6.4, the protrusions height is estimated for a fixed gap d_1, if the diaphragm deflections at each protrusion (P1–P10) which are placed along the central axis of the diaphragm are known for an applied pressure as shown in Fig. 6.5. For a square diaphragm of thickness h, side length a, subjected to a uniform pressure P, and all its edges being fixed in all directions, the deflection w (x, y) is expressed by Eq. (6.3). [94].

$$w(x,y) = \frac{W_{11}}{4}\left[1+\cos\left(\frac{\pi x}{a}\right)\right]\left[1+\cos\left(\frac{\pi y}{a}\right)\right] \tag{6.3}$$

For a fixed diaphragm thickness h of 5 µm, side length a of 500 µm and fixed air gap d_1 of 5 µm, the square diaphragm deflections at C1 to C10 (positions of the protrusions shown in Fig. 6.9) are estimated as w1 to w10 from Eq. (6.3) in the pressure range of 0-1 bar. The height h of each protrusion (P1–P10) is estimated by taking the difference between fixed gap and the estimated diaphragm deflections as $h = d - w$. The various protrusion heights thus estimated are listed in the second column of Table 6.2 respectively. In the design II shown in Fig. 6.6, the protrusions height is estimated for a fixed gap d_2, if the boss

structured circular diaphragm central deflection is known for an applied pressure. For a circular diaphragm of thickness h, radius a, circular boss structure with radius b, subjected to a uniform pressure P, and its circumference being fixed in all directions, the central deflection w_d was given by Eq. (6.4) [94]. For a diaphragm thickness h of 5 μm, radius a of 500 μm, boss radius b of 100 μm and fixed air gap d_2 of 40 μm, the diaphragm central deflections shown in Fig. 6.10 are estimated from Eq. (6.4) in the pressure range of 0-1 bar. From the estimated deflections, the protrusion heights are tabulated in the third column of Table 6.2 respectively.

$$w_d = \frac{P}{16D}\left[\frac{a^4}{4} - \frac{b^4}{4} + a^2 b^2 \ln\left(\frac{b}{a}\right)\right] \tag{6.4}$$

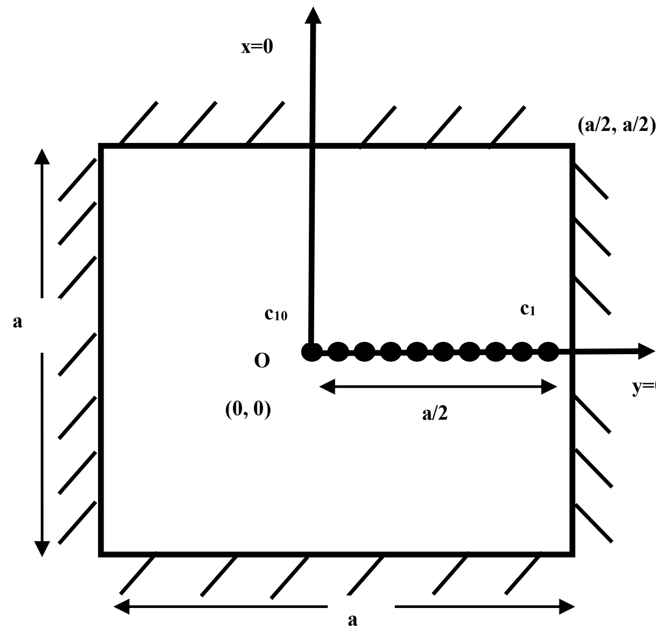

Fig. 6.9 The top view of the square diaphragm

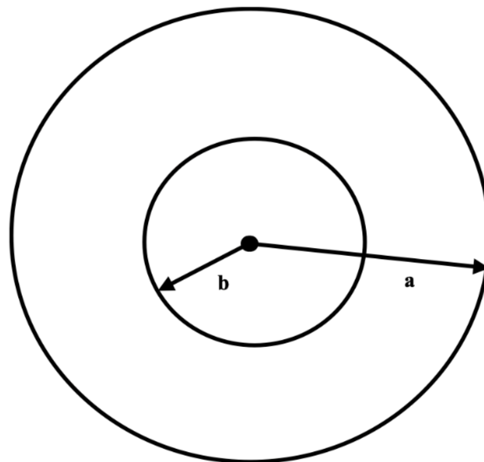

Fig. 6.10 The top view of the circular boss diaphragm

Table 6.2 The side lengths and protrusion heights for all the sensor designs

Pressure (bar)	Diaphragm side length (μm) for initial design	Protrusion height (μm) for design I	Protrusion height (μm) for design II
0.1	527	4.98	36
0.2	443	4.92	32
0.3	400	4.74	28
0.4	372	4.43	25
0.5	352	3.97	21
0.6	336	3.38	17
0.7	324	2.7	13
0.8	313	2	10
0.9	304	1.37	6
1.0	296	0.87	2

6.4 Numerical Simulation

All the designs shown in Fig. 6.1, Fig. 6.4 and Fig. 6.6 are modelled and simulated in COMSOL Multiphysics FEM software using MEMS module to evaluate their performance in the operating pressure range 0-1 bar. The dimension of all the sensor designs are taken from the analytical model results, and the 3D models of the sensor designs were built in the software with appropriate materials for the diaphragm, protrusion and cantilever. Tetrahedron parabolic meshing is applied to all the designs, and the meshed models are shown in Fig. 6.11. As the working principle of all the sensor designs depends on the deflection generated in the diaphragm, FEM analysis is carried out for all the designs to obtain the maximum displacement and stress for an applied pressure in the range of 0-1 bar. The simulation results in Fig. 6.12 show the deflection of the diaphragms with the protrusion touching the metallic cantilevers for an applied pressure of 0.1 bar for all sensor designs.

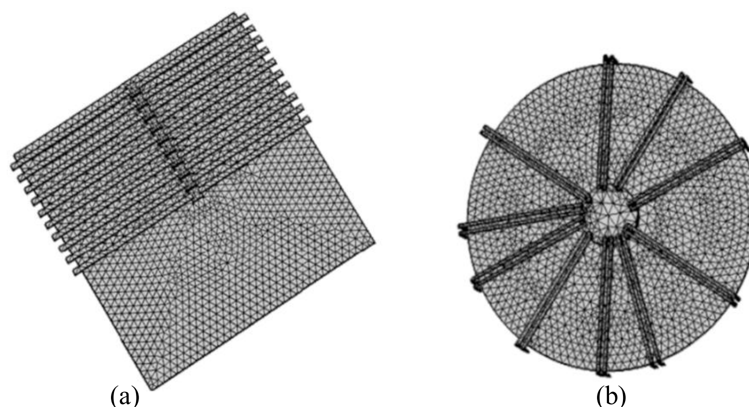

Fig. 6.11 The meshed model of the sensor in COMSOL (a) design I and (b) design II

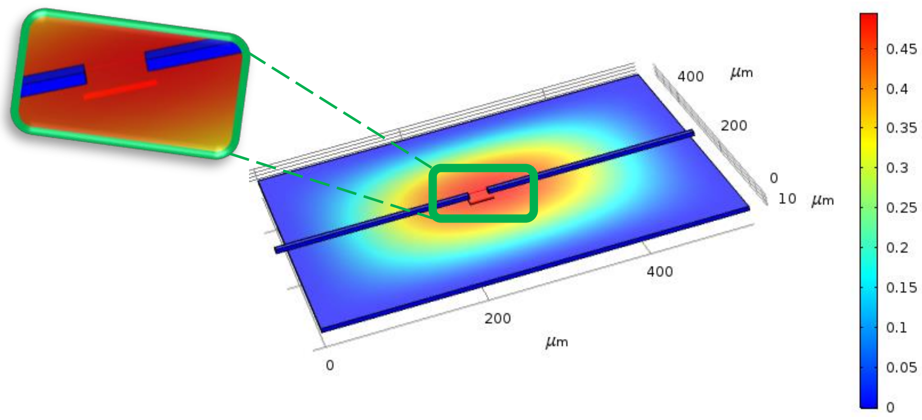

(a)

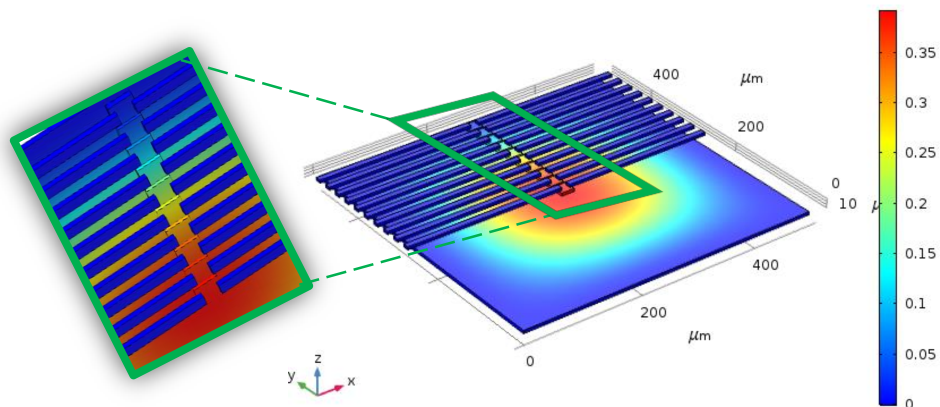

(b)

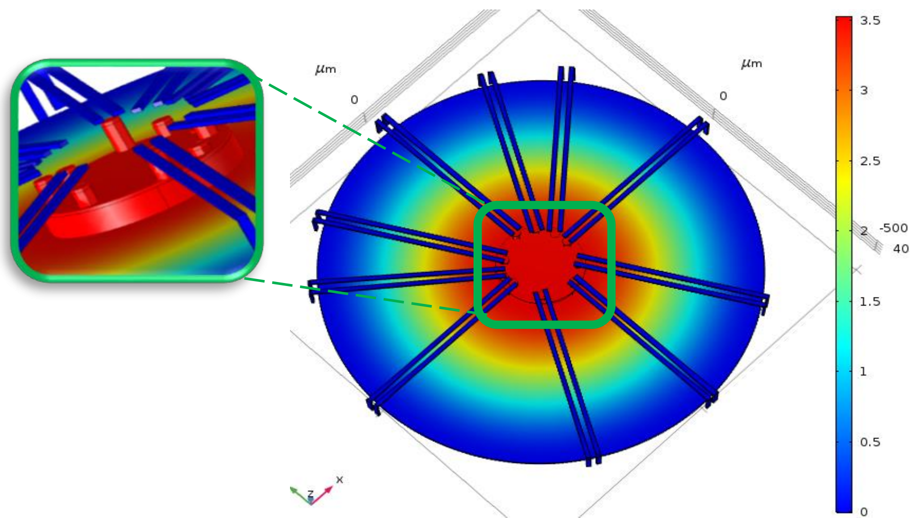

(c)

Fig. 6.12 The simulation results for (a) initial design (b) design I (c) design II

6.5 Proposed Fabrication Steps

The fabrication process for the initial design (single diaphragm) of the pressure sensor is as follows: Initially, a 4-inch 400 μm thick prime quality silicon wafer is taken and cleaned using piranha solution. The process starts with the deposition of 0.1 μm thin layer of gold on the front side of the wafer to create a metal protrusion with the help of physical vapor deposition. Patterning and wet etching of gold is done with a mixture of HCl and HNO_3 solution. A 0.5 μm thick layer of silicon dioxide is deposited on the wafer using PECVD and patterned. The etching of silicon dioxide layer is done by plasma assisted etching technique to form two anchors for the cantilevers. Once again, a 0.1 μm layer of gold is deposited, patterned and etched to obtain the designed width and length of the cantilevers. A thin layer of silicon nitride of 0.1 μm layer is proposed to be deposited using LPCVD method on the patterned cantilever metal layer and the bottom silicon wafer. The bottom side silicon nitride is patterned and reactive ion etching (RIE) process is carried out to remove silicon nitride. This RIE process is followed by a DRIE process of the silicon to realize the diaphragm of 5 μm thickness. After the DRIE of silicon, the silicon nitride layer is stripped off from both sides of the wafer using wet etching with the help of concentrated orthophosphoric acid (H_3PO_4). Finally, sacrificial etching of silicon oxide will be carried out to realise the cantilever structures by dipping the wafer in a 1:3 buffered HF solution followed by DI water rinse and nitrogen drying. The complete fabrication process steps are shown in Fig. 6.13.

6.6 Results and Discussion

The diaphragm deflection for all the designs of the proposed sensor in the pressure range of 0-1 bar is estimated from Eq. (6.2), Eq. (6.3) and Eq. (6.4) derived in Section 6.3 using MATLAB as a mathematical tool and the numerical model using COMSOL developed in Section 6.4. The diaphragm deflection from analytical analysis and simulation has been compared for the initial design of the sensor with two different side lengths 296 μm and 527 μm as shown in Fig. 6.14. Similarly, for design I the diaphragm deflection values at the positions of the protrusions (C1 to C10) from the analytical modelling results are shown in Fig. 6.15(a) and the comparison between the analytical and simulation values at C10 (deflection at P10) is shown in Fig. 6.15(b). In design II, the central deflection values for the circular diaphragm with the boss structure are compared as shown in Fig. 6.16. The results show that the analytical values are in close agreement with the simulation values.

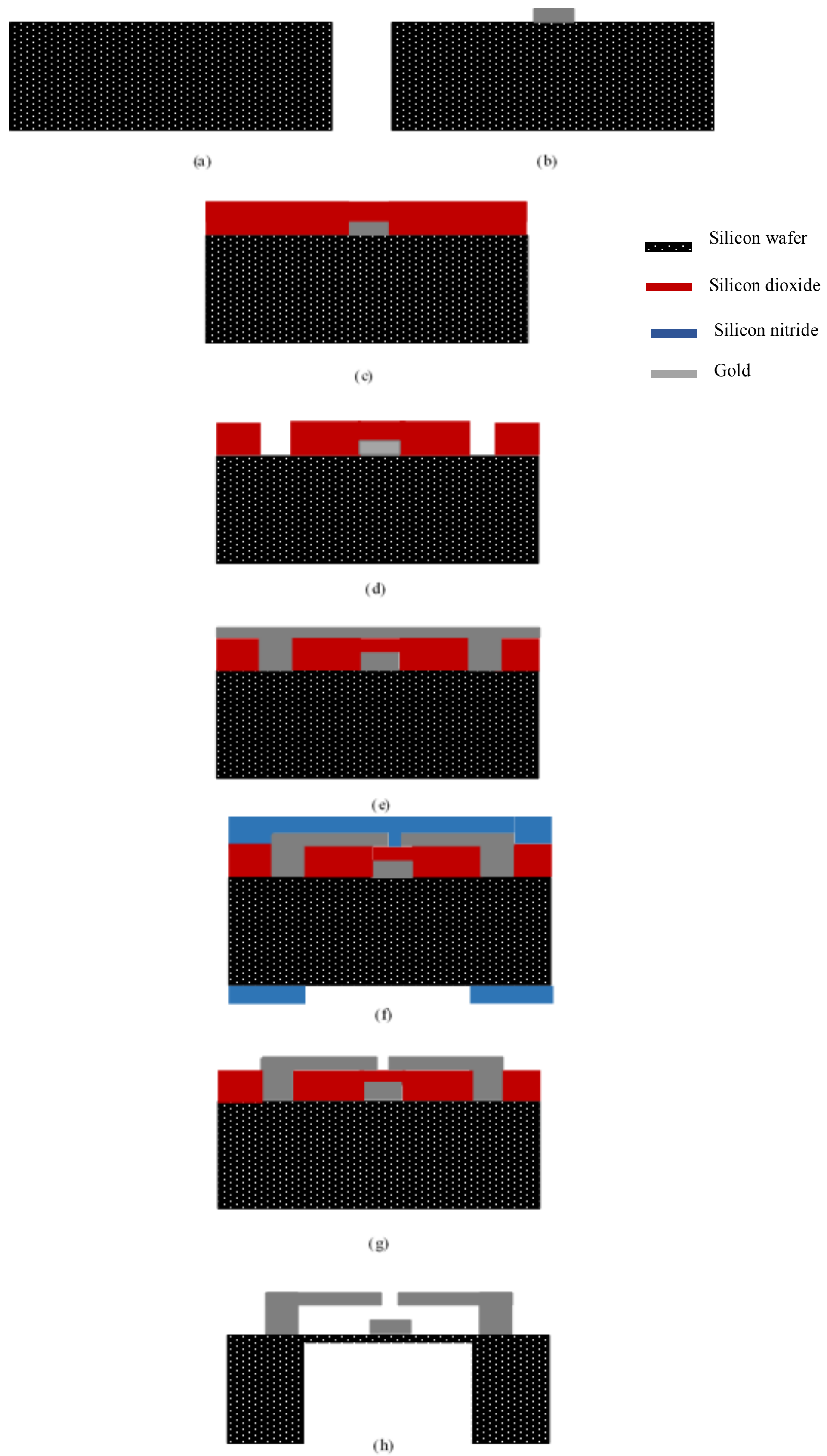

Fig. 6.13 Proposed fabrication steps for initial design of the pressure sensor

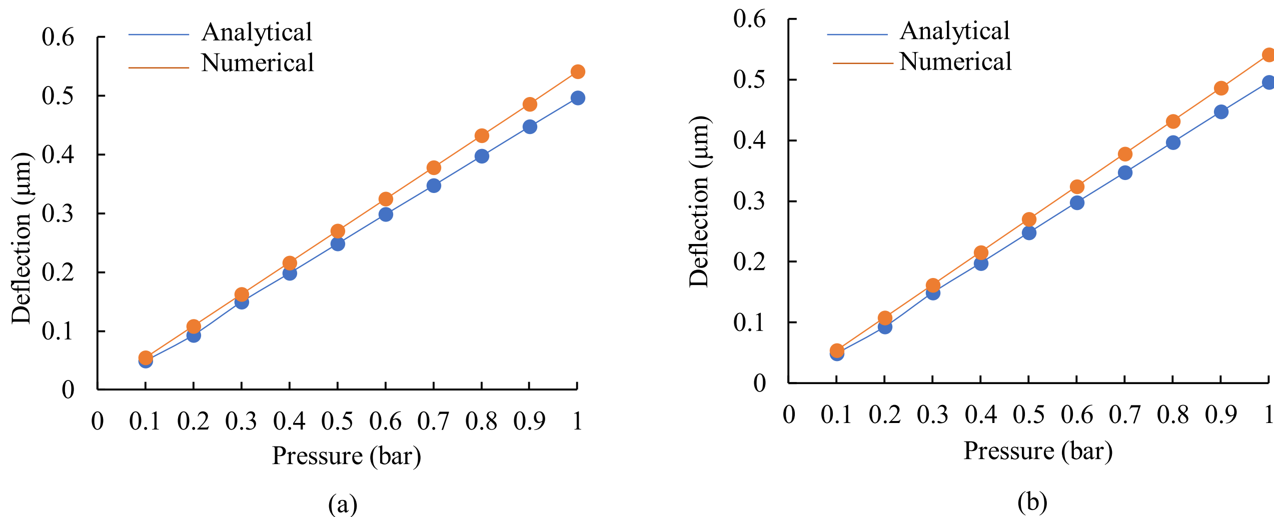

Fig. 6.14 Diaphragm deflection for two side lengths (a) 527 µm and (b) 296 µm

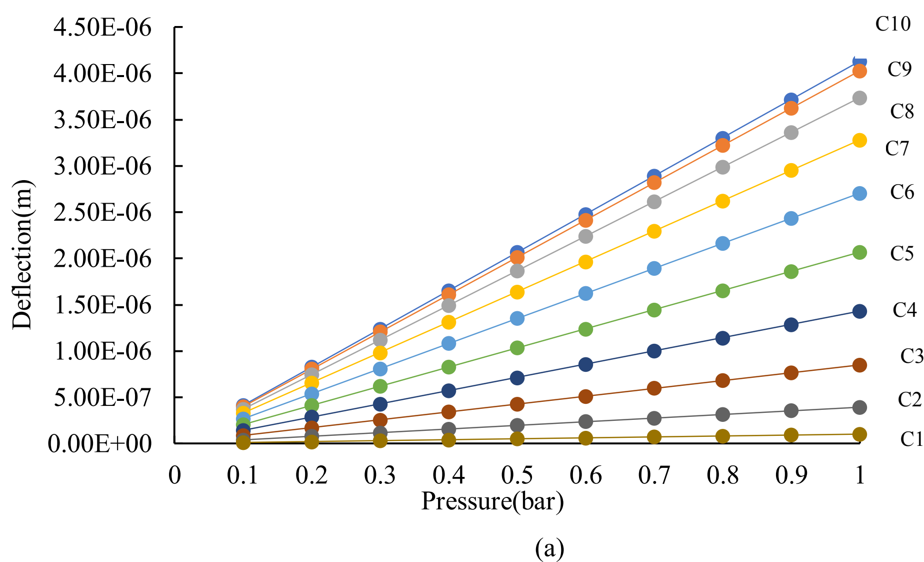

(a)

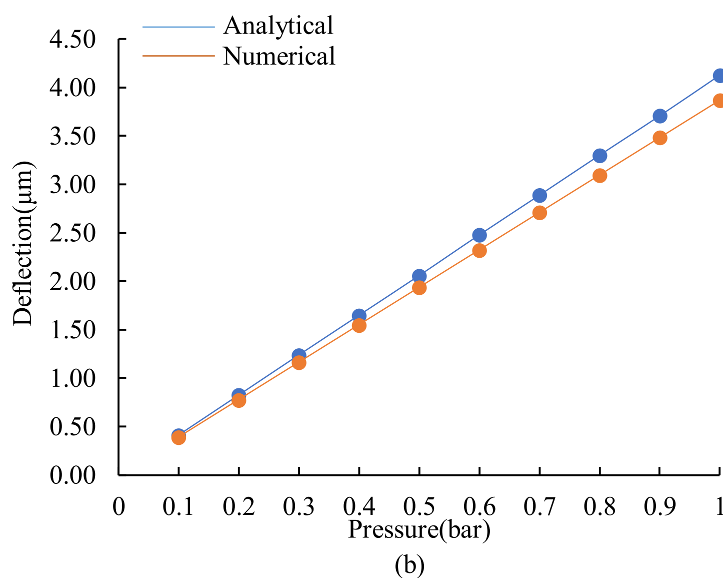

(b)

Fig. 6.15 (a) Analytical results of the diaphragm deflection from C1 to C10 (b) Comparison of simulation and analytical results at C10

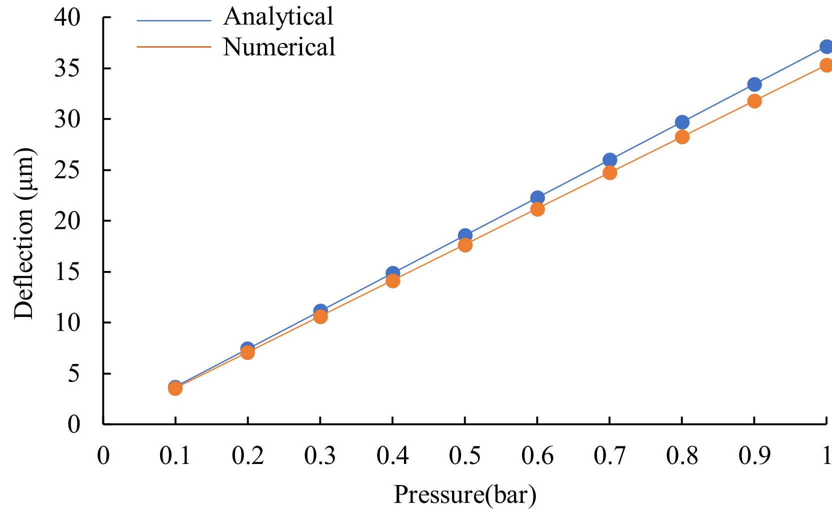

Fig. 6.16 Comparison of diaphragm deflection for design II

6.7 Conclusion

In this work, a MEMS based pressure has been designed and modeled which measures pressure in the range of 0-1 bar and provides output in digital form. Three designs of the pressure sensor have been proposed, and for all three designs, both analytical analysis and numerical simulations have been carried out using COMSOL Multiphysics software. Design I has only one diaphragm instead of ten diaphragms in the initial design and a boss structure is included in design II to reduce the nonlinearity in diaphragm deflection. In the proposed pressure sensor designs, only the deflection of the diaphragm is considered and no pressure is directly applied to the piezo resistor hence, the sensor is free from temperature variations in the case of piezoresistive pressure sensors. The resolution of the sensor can be increased further by increasing the number of protrusions on a single diaphragm. The protrusion heights are estimated from the analytical expressions and are supported by the numerical simulation results. The other advantage of the sensor is that the output is in digital form which is free from hysteresis as compared to the other analog output pressure sensors available in the literature.

Chapter 7

Conclusions and Scope for Future Work

7.1 Conclusions

The objective of the thesis was to design, fabricate and test pressure sensors in meso scale. In the meso scale, a differential Hall effect-based pressure sensor was designed, fabricated and tested along with a modified design. In micro scale, a digital output MEMS pressure sensor with three different designs is designed and simulated.

A pressure sensor with Hall effect sensing was designed and simulated to measure pressure in the range of 0–20 bar. A differential arrangement was proposed in the sensor design and rigorous analytical studies were carried out to optimize the dimensions of the sensor to obtain maximum central diaphragm deflection. The analytical results were also supported by numerical simulation results in the same pressure range obtained from the COMSOL simulation tool. Both the analytical modelling and the numerical simulation results were found to be in good agreement. The design was proposed to be fabricated using stainless steel and a CAD model with detailed dimensions were provided prior to fabrication

Two different designs of pressure sensors were fabricated and tested providing effective pressure measurement in the range of 0-1 bar. One design consists of a differential design which consists of two pairs of Hall sensors and magnets and a single Hall sensor and magnet pair in the other design. Characterization of the Hall sensor was carried out to determine the initial gap between the Hall sensor and magnets. The calibration of both sensor designs were carried out for 25 cycles of ascending and descending pressure. The designed sensors are highly repeatable with a maximum non-linearity of 0.2% for design I and 3.75% for design II. The maximum hysteresis for design I was 0.21% and 0.37% for design II and both the sensors were found to be accurate with a maximum +1.21% error in design I and -4.08% error in design II. The maximum repeatability for design I is 0.0008% and for design II is 0.51%. The resolution of both sensor designs was found to be 0.02 bar Moreover, design I has shown better performance as compared to design II from the analysis of experimental data.

A wired and wireless transmitter has been designed and hardware implemented on the fabricated sensors. The wired transmitter consists of signal conditioning circuitry as the first stage and a V-I converter in the second stage. Two designs of pressure sensors are

used in the development of wired and wireless transmitters. The first stage of the transmitter is the signal conditioning circuitry which amplifies and converts the sensor output in the 1-5 V range. The second stage of the transmitter converts the signal conditioning circuit output to a 4-20 mA current signal for lossless wired transmission over long distances. The V-I converter current output showed good linearity and accuracy for both sensor designs. A wireless transmitter is also designed which employs the NodeMCU enabled with a Wi-Fi module for data transmission and the Blynk IoT console cloud server for data storage and data access. The first stage for the wireless transmitter is similar to the wired transmitter. The output of the first stage is supplied directly to NodeMCU through a potential divider for transmission instead of the second stage. The received data observed in the Blynk IoT console is in close agreement with the Wi-Fi module transmitted data.

A MEMS-based pressure has been designed and modelled which measures pressure in the range of 0–1 bar and provides output in digital form. Three designs of the pressure sensor have been proposed, the first design consists of square diaphragms of different side lengths, the second design consists of a single square diaphragm with different protrusion heights and the third design consists of a circular diaphragm with a boss structure. For all three designs, both analytical analysis and numerical simulations have been carried out using COMSOL Multiphysics software. The results from analytical and simulation analysis are in close agreement with each other. In the proposed pressure sensor designs, only the deflection of the diaphragm is considered and no pressure is directly applied to the piezo resistor hence, the sensor is free from temperature variations in the case of piezo resistor pressure sensors. The proposed sensor can operate on 5V which suits well with conventional CMOS logic. The other advantage of the sensor is that the output is in digital form which has less hysteresis as compared to the other analog output pressure sensors available in the literature.

7.2 Scope for Future Work

In the sensor designs, stainless steel diaphragm can be replaced by silicon elastomer to increase the lifespan and pressure range of the sensor. A suitable mechanism can also be designed, which will help to adjust the zero error of the sensor in case of any external disturbance which alters the initial gap d. The presence of the external stray magnetic fields can also affect the performance of the sensor. To provide proper shielding from external magnetic fields, the entire structure of the sensor to be housed in an enclosure. The effect of external ambient vibrations on the sensor performance can be studied further, and also a method for vibration compensation can be developed. In the case of wireless transmitter, a slight error between the transmitted data and received data is observed. This error may be due to transmission delay and quantization errors. The above errors can be reduced by using a more precise real-time system and reducing the quantization error. This can be achieved by increasing the counter time base rate which can be implemented by suitable microcontrollers. For the digital output pressure sensor, that has been designed and simulated can be fabricated by utilising the proposed fabrication steps.

References

[1] K. Dyndal, Z. Sobkow, J. Sanetra and K. W. Marszalek, "Hall effect test bench for temperature dependence of carrier concentration", *Przeglad Electrotechniczny*, vol. 98 no. 9, pp: 231-234, 2022.

[2] G. Kovatch and W. E. Meserve, "The Hall-effect analog multiplier", *IRE Transactions on Electronic Computers*, vol. EC-10, no. 3, pp. 512-515, 1961. doi: 10.1109/TEC.1961.5219240.

[3] R. Aisuwarya, M. A. Riyan and R. E. Putri, "Design of bicycle's speed measurement System using Hall effect sensor", *Journal of Physics Conference Series*, Ser:1339, 2019.

[4] Z. M. Zhang, X. Cheng, X. Gui, X. Chen and S. Liu, "A steel pressure sensor based on micro fused glass frit technology", *Proceedings 13th international conference on electronic packaging technology and high density packaginig*, pp: 1582-1585, 2012.

[5] A. R. Tripathy, A. Choudhury, A. Dash, P. Panigrahi, S. S. Kumar, P. Pancham, S. K.Sahu and S. Mallik, "Polymer matrix composite engineering for PDMS based capacitive sensors to achieve high-performance and broad-range pressure sensing", *Applied Surface Science Advances*, vol. *3*, 2021. https://doi.org/10.1016/j.apsadv.2021.100062

[6] D. Rodrigues, A.I. Barbosa, R. Rebelo, I.K. Kwon, R.L. Reis and V.M. Correlo, "Skin-integrated wearable systems and implantable biosensors: A comprehensive review", *Biosensors*, vol. 10, no. 79, 2020. https://doi.org/10.3390/bios10070079

[7] S.S. Kumar, A.K. Ojha and B.D. Pant, "Experimental evaluation of sensitivity and non-linearity in polysilicon piezoresistive pressure sensors with different diaphragm sizes", *Microsystem Technologies,* vol.22, pp: 83–91, 2016. https://doi.org/10.1007/s00542-014-2369-3

[8] S.Chang, J. Lee and M. G.Allen, "Robust capacitive pressure sensor array", *Sensors and Actuators A: Physical*, vol.101, no.1, pp: 231-238, 2002. https://doi.org/10.1016/S0924-4247(02)00193-0

[9] Q. Meng, Y. Lu, J. Wang, D. Chen and J. Chen, "A piezoresistive pressure sensor with optimized positions and thickness of piezoresistors", *Micromachines*, vol.12, 1095, 2021. https://doi.org/10.3390/mi12091095

[10] H. Sandmaier and K. Kuhl, "A square-diaphragm piezoresistive pressure sensor with a rectangular central boss for low-pressure ranges", *IEEE Transactions on Electron Devices*, vol. 40, no. 10, pp: 1754-1759, 1993. doi: 10.1109/16.277331.

[11] R. Singh, L. L. Ngo, H. S. Seng and F. N. C. Mok, "A silicon piezoresistive pressure sensor", *Proceedings First IEEE International Workshop on Electronic Design, Test and Applications*, pp: 181-184, 2002. doi: 10.1109/DELTA.2002.994611.

[12] A. Nallathambi, T. Shanmuganantham and D. Sindhanaiselvi, "Design and analysis of MEMS based piezoresistive pressure sensor for sensitivity enhancement", *Materials Today: Proceedings*, vol. 5 no.1, pp: 1897-1903, 2018. https://doi.org/10.1016/j.matpr.2017.11.291

[13] M. Aryafar, M. Hamedi and M. Ganjeh, "A novel temperature compensated piezoresistive pressure sensor", *Measurement*, vol. 63, pp: 25-29, 2015. https://doi.org/10.1016/j.measurement.2014.11.03

[14] A. V. Tran, X. Zhang and B. Zhu, "The development of a new piezoresistive pressure sensor for low pressures", *IEEE Transactions on Industrial Electronics*, vol. 65, no. 8, pp: 6487-6496, 2018. doi: 10.1109/TIE.2017.2784341.

[15] M. Basov and D. M. Prigodskiy, "Investigation of high-sensitivity piezoresistive pressure sensors at ultra-low differential pressures", *IEEE Sensors Journal*, vol. 20, no. 14, pp: 7646-7652, 2020. doi: 10.1109/JSEN.2020.2980326.

[16] A. A. L'vov, P. A. L'vov and R. S. Konovalov, "Improvement of piezoresistive pressure sensor accuracy by means of current loop circuit using optimal digital signal processing", *IEEE NW Russia Young Researchers in Electrical and Electronic Engineering Conference (EIConRusNW)*, pp: 262-265, 2016. doi: 10.1109/EIConRusNW.2016.7448170.

[17] D. Šaponjić and A. Žigic, “Correction of a piezoresistive pressure sensor using a microcontroller”, *Instruments and Experimental Techniques,* vol. 44, pp: 38–44 2001. https://doi.org/10.1023/A:1004168614028

[18] G. Gilanizadehdizaj, K. C. Aw, J. Stringer and D. Bhattacharyya, “Facile fabrication of flexible piezo-resistive pressure sensor array using reduced graphene oxide foam and silicone elastomer”, *Sensors and Actuators A: Physical*, vol. 340, 2022. https://doi.org/10.1016/j.sna.2022.113549

[19] D. Du, X. Ma, W.An and S. Yu, “Flexible piezoresistive pressure sensor based on wrinkled layers with fast response for wearable applications”, *Measurement*, vol. 201, 2022. https://doi.org/10.1016/j.measurement.2022.111645

[20] H. Li, K. Wu, Z. Xu, Z. Wang, Y. Meng, and L. Li, “Ultrahigh-sensitivity piezoresistive pressure sensors for detection of tiny pressure”, *ACS Applied Materials & Interfaces,* vol. 10, no. 24, pp: 20826-20834, 2018. DOI: 10.1021/acsami.8b03639

[21] T. Zhao, T. Li, L. Chen, L. Yuan, X. Li and J. Zhang, “Highly sensitive flexible piezoresistive pressure sensor developed using biomimetically textured porous materials”, *ACS Applied Materials & Interfaces,* vol. 11, no. 32, pp: 29466-29473, 2019. DOI: 10.1021/acsami.9b09265

[22] T. T. Nguyen, L. A. L. Fernandes and P. Häfliger, “An energy-efficient implantable transponder for biomedical piezo-resistance pressure sensors”, *IEEE Sensors Journal*, vol. 14, no. 6, pp: 1836-1843, 2014. doi: 10.1109/JSEN.2014.2304566.

[23] L. Kaabi, J. Sakly and M. Saafi, “A low pressure meter based on a capacitive micro sensor”, *Physics Procedia*, vol. 2, no.3, pp: 1495-1503, 2009. https://doi.org/10.1016/j.phpro.2009.11.122

[24] M. Molla-Alipour and B. A. Ganji, “Analytical analysis of mems capacitive pressure sensor with circular diaphragm under dynamic load using differential transformation method (DTM)”, *Acta Mechanica Solida Sinica*, vol.28, no.4, pp: 400-408, 2015. https://doi.org/10.1016/S0894-9166(15)30025-2

[25] K. S. Rao, B. M. Reddy, V. B. Teja, *et al.* "Design and simulation of MEMS based capacitive pressure sensor for harsh environment", *Microsystem Technologies,* vol.26, pp:1875–1880, 2020. https://doi.org/10.1007/s00542-019-04735-2

[26] M. Jang and K.S. Yun, "MEMS capacitive pressure sensor monolithically integrated with CMOS readout circuit by using post CMOS processes", *Micro and Nano System Lett*ers, vol.5, no.4, 2017. https://doi.org/10.1186/s40486-016-0037-3

[27] X. Chen, D. Brox, B. Assadsangabi, M. S. Mohamed Ali and K. Takahata, "A stainless-steel-based capacitive pressure sensor chip and its microwelding integration", *Transducers – 2015 18th International Conference on Solid-State Sensors, Actuators and Microsystems (TRANSDUCERS)*, pp: 1081-1084, 2015. doi: 10.1109/TRANSDUCERS.2015.7181114.

[28] F. Liu, S. Dai, J. Cao, Z. Zhang, G. Cheng and J. Ding, "CNTs based capacitive stretchable pressure sensor with stable performance", *Sensors and Actuators A: Physical*, vol. 343, 2022. https://doi.org/10.1016/j.sna.2022.113672

[29] M. Chattopadhyay and D. Chowdhury, "Design and performance analysis of MEMS capacitive pressure sensor array for measurement of heart rate", *Microsystem Technolo*gies, vol.23, pp: 4203–4209, 2017. https://doi.org/10.1007/s00542-016-2842-2

[30] K.S. Rao, W. Samyuktha, D.V. Vardhan, *et al.* "Design and sensitivity analysis of capacitive MEMS pressure sensor for blood pressure measurement", *Microsystem Technologies,* vol.26, pp: 2371–2379, 2020. https://doi.org/10.1007/s00542-020-04777-x

[31] M. N. Jelodar and B. A. Ganji, "Design and analysis of a novel MEMS capacitive tire pressure sensor with high sensitivity and linearity", *Majlesi Journal of Telecommunication Devices*, vol.5, no. 2, pp: 69-75, 2016.

[32] M. C. Scardelletti and C. A. Zorman, "Packaged capacitive pressure sensor system for aircraft engine health monitoring", *IEEE Sensors Journal*, pp: 1-3, 2016 doi: 10.1109/ICSENS.2016.7808607.

[33] Y. Sujan, G. Uma and M. Umapathy, "Design and testing of piezoelectric resonant pressure sensor", *Sensors and Actuators A: Physical*, vol. 250, pp: 177-186, 2016. https://doi.org/10.1016/j.sna.2016.09.031

[34] N. Alcheikh, A. Hajjaj and M. Younis, "Highly sensitive and wide-range resonant pressure sensor based on the veering phenomenon", *Sensors and Actuators A: Physical*, vol. 300, 2019. https://doi.org/10.1016/j.sna.2019.111652

[35] T. T. Pham, H. Zhang, S. Yenuganti, S. Kaluvan and J. A. Kosinski, "Design, modeling, and experiment of a piezoelectric pressure sensor based on a thickness-shear-mode crystal resonator," *IEEE Transactions on Industrial Electronics*, vol. 64, no. 11, pp: 8484-8491, 2017. doi: 10.1109/TIE.2017.2733498.

[36] S. Yenuganti, H. Zhang and C. Zhang, "Langasite crystal based pressure sensor with temperature compensation", *Sensors and Actuators A: Physical*, vol. 281, pp: 108-116, 2018. https://doi.org/10.1016/j.sna.2018.07.012

[37] M. S. Patel and B. K. Sinha, "A dual-mode thickness-shear quartz pressure sensor for high pressure applications", *IEEE Sensors Journal*, vol. 18, no. 12, pp: 4893-4901, 2018. doi: 10.1109/JSEN.2018.2822282.

[38] Y. Sujan, G. Uma and M. Umapathy, "Design and modelling of a micro resonant pressure sensor", *Microsystem Technologies,* vol.23, pp: 1285–1293, 2017. https://doi.org/10.1007/s00542-016-2824-4

[39] Y. Li, Y. Lu, B. Xie, J. Chen, J. Wang and D. Chen, "A micromachined resonant differential pressure sensor", *IEEE Transactions on Electron Devices*, vol. 67, no. 2, pp: 640-645, 2020. doi: 10.1109/TED.2019.2957880.

[40] Y. Sujan, G. Uma and M. Umapathy, "Micro pressure sensor with three degrees of freedom resonator", *Microsystem Technologies,* vol. 23, pp: 3201–3214, 2017. https://doi.org/10.1007/s00542-016-3108-8

[41] X. Han, L. Zhao, J. Wang, L. Wang, M. Huang, C. Chen, P. Yang, Z. Li, N. Zhu, S. Wang, X. Yan, Y. Wang, H. Wang, Y. Wu, Y. Chen and Z. Jiang, “High-accuracy differential resonant pressure sensor with linear fitting method**”,** *Journal of Micromechanics and Microengineering,* vol. 31, no. 4, pp: 045006, 2021.

[42] X. Du, L. Wang, A. Li, L. Wang and D. Sun, “High accuracy resonant pressure sensor with balanced-mass DETF resonator and twinborn diaphragms”, *Journal of Microelectromechanical Systems*, vol. 26, no. 1, pp: 235-245, 2017. doi: 10.1109/JMEMS.2016.2632108.

[43] C. F. Chiang *et al.*, “Resonant pressure sensor with on-chip temperature and strain sensors for error correction”, *IEEE 26th International Conference on Micro Electro Mechanical Systems (MEMS)*, pp: 45-48, 2013. doi: 10.1109/MEMSYS.2013.6474172.

[44] X.Han, Q. Mao, L. Zhao, *et al.* “Novel resonant pressure sensor based on piezoresistive detection and symmetrical in-plane mode vibration”, *Microsystems & Nanoengineering,* vol. 6, no. 95, 2020. https://doi.org/10.1038/s41378-020-00207-0

[45] P. Maurya and N. Mandal, “Design analysis of wireless pressure measurement by integrating surface acoustic wave sensor with bourdon tube”, *IEEE Sensors Journal*, vol. 18, no. 21, pp: 8996-9004, 2018, doi: 10.1109/JSEN.2018.2867567.

[46] Y. Seo, D. Kim and N. A. Hall, “Piezoelectric pressure sensors for hypersonic flow measurements”, *Journal of Microelectromechanical Systems*, vol. 28, no. 2, pp: 271-278, 2019. doi: 10.1109/JMEMS.2019.2899266.

[47] H. Han and J. Kim, “Active muscle stiffness sensor based on piezoelectric resonance for muscle contraction estimation”, *Sensors and Actuators A: Physical*, vol.194, pp: 212-219, 2013. https://doi.org/10.1016/j.sna.2013.01.054

[48] G. J. Radosavljevic, L. D. Zivanov, W. Smetana, A. M. Maric, M. Unger and L. F. Nad, “A wireless embedded resonant pressure sensor fabricated in the standard LTCC technology”, *IEEE Sensors Journal*, vol. 9, no. 12, pp: 1956-1962, 2009, doi: 10.1109/JSEN.2009.2030974.

[49] W. J. Bock, M. Beaulieu and A. W. Domanski, “GaAs-based fiber-optic pressure sensor”, *IEEE Transactions on Instrumentation and Measurement*, vol. 41, no. 1, pp: 68-71, 1992. doi: 10.1109/19.126634.

[50] P. Maurya and N. Mandal, “Design and analysis of an electro-optic type pressure transmitter using bellows as primary sensor”, *IEEE Sensors Journal*, vol. 18, no. 18, pp: 7730-7740, 2018. doi: 10.1109/JSEN.2018.2862921.

[51] J. Feng, Y. Zhao, S. S. Li, X. W. Lin, F. Xu and Y. Q. Lu, “Fiber-Optic pressure sensor based on tunable liquid crystal technology”, *IEEE Photonics Journal*, vol. 2, no. 3, pp: 292-298, 2010. doi: 10.1109/JPHOT.2010.2045365.

[52] N. Paliwal and J. John, “Design and modeling of highly sensitive lossy mode resonance-based fiber-optic pressure sensor”, *IEEE Sensors Journal*, vol. 18, no. 1, pp: 209-215, 2018. doi: 10.1109/JSEN.2017.2771313.

[53] A. Phan, P. Truong, J. Trumpp and F. E. Talke, “Design of an optical pressure measurement system for intraocular pressure monitoring”, *IEEE Sensors Journal*, vol. 18, no. 1, pp: 61-68, 2018. doi: 10.1109/JSEN.2017.2767539.

[54] V. Neeharika and P. K. Pattnaik, “Optical MEMS pressure sensors incorporating dual waveguide Bragg gratings on diaphragms”, *IEEE Sensors Journal*, vol. 16, no. 3, pp: 681-687, 2016. doi: 10.1109/JSEN.2015.2482944.

[55] T. H. da Costa and J. Choi, “An all-elastomer pressure sensor utilizing printed carbon nanotube patterns with high sensitivity”. *Micro and Nano Engineering*, vol. 14, 2022. https://doi.org/10.1016/j.mne.2022.100113

[56] V. N. Kumar and K. V. L. Narayana, “Development of an ANN-based pressure transducer” *IEEE Sensors Journal*, vol. 16, no. 1, pp: 53-60, 2016. doi: 10.1109/JSEN.2015.2477458.

[57] Y. Zhang, Q. Hao and G. Xiao, “Low-Frequency noise of magnetic sensors based on the anomalous Hall effect in Fe–Pt alloys”, *Sensors*, vol. 19, 2019. https://doi.org/10.3390/s19163537

[58] A. Girgin, M. Bilmez, H. Y. Amin and T. C. Karalar, “A silicon Hall sensor SoC for current sensors”, *Microelectronics Journal*, vol. 90, pp: 12-18, 2019. https://doi.org/10.1016/j.mejo.2019.04.020

[59] S. Du, J. Hu, Y. Zhu and M. Zhang, "A Hall sensor-based position measurement with on-line model parameters computation for permanent magnet synchronous linear motor", *IEEE Sensors Journal*, vol. 18, no. 13, pp: 5245-5255, 2018. doi: 10.1109/JSEN.2018.2836218.

[60] S. M. Yang and C. L. Huang, "A Hall sensor-based three-dimensional displacement measurement system for miniature magnetically levitated rotor", *IEEE Sensors Journal*, vol. 9, no. 12, pp: 1872-1878, 2009. doi: 10.1109/JSEN.2009.2029042.

[61] S. Zahran, A. M. Moussa, A. B. Sesay and N. El-Sheimy, "A new velocity meter based on Hall effect sensors for UAV indoor navigation", *IEEE Sensors Journal*, vol. 19, no. 8, pp: 3067-3076, 2019. doi: 10.1109/JSEN.2018.2890094.

[62] J. C. S. Borges, D. B. B. de Deus, A. C. Lima Filho and F. A. Belo, "New contactless torque sensor based on the Hall effect", *IEEE Sensors Journal*, vol. 17, no. 16, pp: 5060-5067, 2017. doi: 10.1109/JSEN.2017.2723041.

[63] G. Rajita, D. Banerjee, N. Mandal and S. C. Bera, "Design and analysis of Hall effect probe-based pressure transmitter using bellows as sensor", *IEEE Transactions on Instrumentation and Measurement*, vol. 64, no. 9, pp: 2548-2556, 2015. doi: 10.1109/TIM.2015.2403152.

[64] S. Saha, S. K. Bera, H. Mandal, P. K. Sadhu and S. C. Bera, "A temperature compensated non-contact pressure transducer using Hall sensor and bourdon tube", *IEEE Sensors Journal*, vol. 19, no. 14, pp: 5429-5438, 2019. doi: 10.1109/JSEN.2019.2904767.

[65] J. Seo and C. Yoo, "Omnidirectional fingertip pressure sensor using Hall effect", *Sensors* vol.21, no.21, 2021. https://doi.org/10.3390/s21217072

[66] N. A. B. Zulkifli *et al.*, "Highly reliable magnetic-based pressure sensor utilizing simple microstructured PDMS: mechanical and design analysis via finite element analysis", *IEEE Sensors Journal*, vol. 21, no. 15, pp; 16560-16567, 2021. doi: 10.1109/JSEN.2021.3077630.

[67] H. Y. Yu, M. Qin, M. Nie and Q. A. Huang, "A MEMS pressure sensor based on Hall effect", *IEEE Sensors Journal*, pp: 218-221, 2011. doi: 10.1109/ICSENS.2011.6127076.

[68] U. P. Borole, S. Subramaniam, I. R.Kulkarni, P. Saravanan, H. C. Barshilia and P. Chowdhury, "Highly sensitive giant magnetoresistance (GMR) based ultralow differential

pressure sensor", *Sensors and Actuators A: Physical*, vol. 280, pp: 125-131, 2018. https://doi.org/10.1016/j.sna.2018.07.022

[69] S. F. Ali and N. Mandal, "Design and development of an electronic level transmitter based on hydrostatic principle", *Measurement*, vol. 132, pp: 125-134, 2019. https://doi.org/10.1016/j.measurement.2018.09.055

[70] S. F. Ali and N. Mandal, "Design and development of an electronic level transmitter using inter digital capacitor", *IEEE Sensors Journal*, vol. 19, no. 13, pp: 5179-5185, 2019. doi: 10.1109/JSEN.2019.2903296.

[71] E. Sisinni, A. Depari and A. Flammini, "Design and implementation of a wireless sensor network for temperature sensing in hostile environments", *Sensors and Actuators A: Physical*, vol. 237, pp: 47-55, 2016. https://doi.org/10.1016/j.sna.2015.11.012

[72] B. Mondal, S. F. Ali and N. Mandal, "An approach to design a wireless air flow transmitter using flex sensor", *IEEE Sensors Journal*, vol. 21, no. 9, pp: 10498-10505, 2021. doi: 10.1109/JSEN.2021.3060814.

[73] R. Firdaus, M. A. Murti and I. Alinursafa, "Air quality monitoring system based internet of things (IoT) using LPWAN LoRa", *IEEE International Conference on Internet of Things and Intelligence System (IoTaIS)*, pp: 195-200, 2019. doi: 10.1109/IoTaIS47347.2019.8980437.

[74] N. Ahmad, A. Hussain, I. Ullah and B. H. Zaidi, "IOT based wireless sensor network for precision agriculture", *7th International Electrical Engineering Congress (iEECON)*, pp: 1-4, 2019. doi: 10.1109/iEECON45304.2019.8938854.

[75] A. Ismail *et al*., "A high performance MEMS based digital-output gyroscope", *Transducers & Eurosensors XXVII: The 17th International Conference on Solid-State Sensors, Actuators and Microsystems (TRANSDUCERS & EUROSENSORS XXVII)*, pp: 2523-2526, 2013. doi: 10.1109/Transducers.2013.6627319.

[76] M. L. Ya *et al*., "Design and analysis of a first-order sigma-delta analog-to-digital converter for MEMS resistive sensor", *IEEE International Conference on Semiconductor Electronics (ICSE2010)*, pp: 297-300, 2010. doi: 10.1109/SMELEC.2010.5549366.

[77] V. Kumar, X. Guo, R. Jafari and S. Pourkamali, “Ultra-low power self-computing binary output digital MEMS accelerometer”, *IEEE 29th International Conference on Micro Electro Mechanical Systems (MEMS)*, pp: 251-254, 2016. doi: 10.1109/MEMSYS.2016.7421607.

[78] J. J. Yang, G. Tsai and T. H. Tsai, “A 53.36pF/MPA CMOS-MEMS pressure sensor with compact size and integrated digital readout”, *IEEE 33rd International Conference on Micro Electro Mechanical Systems (MEMS)*, pp: 661-664, 2020. doi: 10.1109/MEMS46641.2020.9056292.

[79] J. A. Montiel-Nelson, J. Sosa, R. Pulido, A. Beriain, H. Solar and R. Berenguer, “Digital output MEMS pressure sensor using capacitance-to-time converter”, *Design of Circuits and Integrated Systems*, pp. 1-4, 2014. doi: 10.1109/DCIS.2014.7035565.

[80] K. Sivasundari, R.J. Daniel and K. Sumangala, “Evolution, modelling and simulation of MEMS PWM pressure sensor employing cantilever switch and SOI diaphragm”, *Microsystem Technologies,* vol. 23, pp: 3559–3574, 2017. https://doi.org/10.1007/s00542-016-3169-8

[81] T. Nguyen Thanh and P. Häfliger, “A 9.4-bit, 28.8-mV range inverter based readout circuit for implantable pressure bridge piezo-resistive sensor”, *IEEE International Symposium on Circuits and Systems (ISCAS)*, pp: 2377-2380, 2014.doi: 10.1109/ISCAS.2014.6865650.

[82] J. Long, “A novel PWM based readout circuit for pressure sensors”, *3rd International Conference on Information Science and Control Engineering (ICISCE)*, pp: 779-783, 2016. doi: 10.1109/ICISCE.2016.171.

[83] J. Y. Yang, Zhiping Yu and Litian Liu, “PMOS ring oscillating digital pressure sensor manufactured by MEMS process”, *9th International Conference on Solid-State and Integrated-Circuit Technology*, pp: 2436-2439, 2008. doi: 10.1109/ICSICT.2008.4735064.

[84] J. Y. Yang *et al*., “Digital pressure sensor with filtered frequency output using ring oscillator and mixer”, *1st Asia Symposium on Quality Electronic Design*, pp: 363-365, 2009. doi: 10.1109/ASQED.2009.5206239.

[85] K. Sivasundari, D.M. Sugantharathnam and R.J. Daniel, “Fabrication of surface micromachined molybdenum cantilever beams for PWM MEMS pressure sensor and issues that

affect yield", *Microsystem Technologies,* vol. 25, pp: 2535–2545, 2019. https://doi.org/10.1007/s00542-019-04388-1

[86] R. Proie, J. S. Pulskamp, R. G. Polcawich, T. Ivanov and M. Zaghloul, "Low-power 3-bit piezoelectric MEMS analog to digital converter", *IEEE 24th International Conference on Micro Electro Mechanical Systems*, pp: 1241-1244, 2011. doi: 10.1109/MEMSYS.2011.5734657.

[87] K. R. Sandra, B. George and V. J. Kumar, "Combined variable reluctance Hall effect displacement sensor", *IEEE Transactions on Instrumentation and Measurement*, vol. 67, no. 5, pp: 1169-1177, 2018. doi: 10.1109/TIM.2017.2761958.

[88] Le Khac Quynh *et al* "Simple planar Hall effect based sensors for low-magnetic field detection" *Advances in Natural Sciences: Nanoscience and Nanotechnology,* vol.10, 2019.

[89] K. Bhaskar, T.K. Varadan, "Plates: theories and applications", Ane Books Pvt Ltd, New Delhi 2013.

[90] B. S. Kumar, K.Suresh, U.V. Kumar, G. Uma and M. Umapathy, "Resonance based DC current sensor", *Measurement*, vol.45 no.3, pp: 369-374, 2012. https://doi.org/10.1016/j.measurement.2011.11.008.

[91] M.S. Manjunath, N. Nagarjuna, G. Uma, *et al.* "Design, fabrication and testing of reduced graphene oxide strain gauge based pressure sensor with increased sensitivity", *Microsystem Technologies,* vol. 24, pp: 2969–2981, 2018. https://doi.org/10.1007/s00542-018-3782-9

[92] A.V. Tran, X. Zhang and B. Zhu, "Mechanical structural design of a piezoresistive pressure sensor for low-pressure measurement: A computational analysis by increases in the sensor sensitivity", *Sensors*, vol. 18, 2018. https://doi.org/10.3390/s18072023

[93] K.N. Bhat and M.M. Nayak, "MEMS pressure sensors–an overview of challenges in technology and packaging", *Journal of Institute of smart structures and systems (ISSS)*, vol.1 No. 1, pp: 1–10, 2013.

[94] R. Szilard, "Theories and applications of plate analysis", Wiley, New Jersey, 2004.

List of Publications

Peer Reviewed Journals:

1. S. Paliwal and S. Yenuganti, “A differential Hall effect based pressure sensor”, *Journal of Electrical Engineering and Technology,* vol. 16, pp: 1119–1129, 2021. (SCI indexed)
2. S. Paliwal, S. Yenuganti and M. Manuvinakurake, “Fabrication and testing of a Hall effect based pressure sensor", *Sensor Review*, vol. 42, no. 3, pp: 354-364, 2022. (SCI indexed)
3. S. Paliwal and S. Yenuganti, “Design and simulation of digital output MEMS pressure sensor”, *Arabian Journal of Science and Engineering,* vol. 45, pp: 6661–6673, 2020. (SCI indexed)

Conferences:

1. S. Paliwal and S. Yenuganti, "Implementation of Wired and IoT Based Wireless Transmitters for a Pressure Sensor," OPJU International Technology Conference on Emerging Technologies for Sustainable Development (OTCON), Raigarh, Chhattisgarh, India, 2023, pp. 1-6, doi: 10.1109/OTCON56053.2023.10113907

Brief Biography of the Candidate

Mr. Sankalp Paliwal was born in Kanpur, Uttar Pradesh on 29th October 1990. He received his Bachelor's degree in Electronics and Instrumentation from Sri Ramswaroop Memorial College of Engineering and Management, AKT University, Lucknow in 2013 and received his ME degree in Electronics Instrumentation and Control from Thapar University, Patiala, Punjab in 2016. From August 2016 to January 2019 he worked as an assistant professor in BBD University, Lucknow. He joined his Doctoral program at BITS Pilani, Pilani campus in January 2019. His research areas include sensor fabrication and instrumentation.

Brief Biography of the Supervisor

Dr. Sujan Yenuganti received his Bachelor's Degree in Electronics and Instrumentation Engineering from JNT University, Hyderabad, India, in 2007; his Master's Degree (MS by Research) and Ph.D. Degree in Instrumentation and Control Engineering from the National Institute of Technology Tiruchirappalli, Trichy, India, in 2012 and 2017. His Ph.D. work is in the area of design and development of resonant-based micro and meso scale pressure sensors. He also worked as a post-doctoral research associate in the smart materials lab, at the University of North Texas, Texas, USA for one year after his Ph.D. Currently, he is working as Assistant Professor in the EEE department at Birla Institute of Technology and Science, Pilani, India. His research interests include the design and simulation of MEMS-based sensors, Energy harvesting, the development of sensors using smart materials, and QCM-based sensors.